Dynamique et contrôle de l'interaction onde de choc / couche limite

Bur Reynald

Centre Val de Loire UNIVERSITÉ
Spirit of the Loire Valley

UNIVERSITÉ D'ORLÉANS

UNIVERSITE D'ORLEANS

PRISME

Laboratoire de rattachement : ONERA / Département Aérodynamique, Aéroélasticité, Acoustique

HDR présentée par :

Reynald BUR

soutenue le : 8 septembre 2017

Discipline : Energétique

Dynamique et contrôle de l'interaction onde de choc / couche limite

RAPPORTEURS :

Jean-Paul BONNET	Directeur de Recherche, Institut PPRIME
Georges GEROLYMOS	Professeur, Sorbonne Universités / UPMC
Jean-Christophe ROBINET	Professeur, DynFluid / ENSAM

JURY :

Alain MERLEN	Professeur, Université de Lille 1, Président du jury
Holger BABINSKY	Professor, University of Cambridge
Jean-Paul BONNET	Directeur de Recherche, Institut PPRIME
Georges GEROLYMOS	Professeur, Sorbonne Universités / UPMC
Azeddine KOURTA	Professeur, PRISME / Université d'Orléans
Jean-Christophe ROBINET	Professeur, DynFluid / ENSAM
Denis SIPP	Directeur de Recherche, ONERA

Dynamique et contrôle de l'interaction onde de choc / couche limite

Reynald BUR

ONERA
Département Aérodynamique, Aéroélasticité, Acoustique

TABLE DES MATIERES

1. INTRODUCTION

Ce mémoire résume une partie majeure de mes travaux réalisés en tant qu'ingénieur de recherche à l'ONERA dans le département d'aérodynamique fondamentale et expérimentale. Ces travaux se placent dans le contexte d'un organisme dont l'objet est d'apporter des solutions aux problèmes de l'industrie aéronautique et spatiale. Dans le domaine du transport aérien civil, la commission européenne via les directives de son programme *Flightpath 2050*, entend imposer une réduction drastique des émissions de polluants et des nuisances sonores. Dans le domaine militaire, il s'agit plutôt de satisfaire des spécifications exigeantes de furtivité en gardant des performances aérodynamiques convenables. Quant au domaine spatial, l'optimisation des trajectoires de lanceurs pour assurer de manière fiable la mise en orbite de satellites ainsi que celles des corps et engins en phase de rentrée atmosphérique est un enjeu crucial pour les industriels du secteur.

Dans ce contexte, la compréhension des phénomènes physiques pour les domaines de vol énoncés nécessite de résoudre des problèmes liés à l'aérodynamique compressible, et plus particulièrement au phénomène d'interaction onde de choc / couche limite lorsque l'écoulement devient uniformément ou localement supersonique. Ces interactions faibles ou fortes, selon l'intensité du choc et la nature (laminaire, transitionnelle ou turbulente) de la couche limite, provoquent une amplification des effets dissipatifs et des pertes de pression d'arrêt (et production d'entropie) dans l'écoulement et, fréquemment, l'apparition d'un décollement qui a des conséquences néfastes : production de traînée (d'onde et de frottement), perte d'efficacité et amplification des instabilités dans la couche de cisaillement. Ceci se traduit par une chute des performances pour une voilure supercritique d'avion de transport, et une baisse de rendement pour la prise d'air et la tuyère d'avion de combat ou de missile. Le domaine de vol est également affecté par une apparition précoce du tremblement sur la voilure et du pompage de la prise d'air (oscillations auto-entretenues à basse fréquence de l'onde de choc dans les deux cas).

La partie du mémoire présentant les résultats de mes travaux se décompose en trois parties. Un premier chapitre présente la soufflerie de recherche supersonique dans laquelle les écoulements sont étudiés, ainsi que les moyens de visualisation et de mesure utilisés. Les écoulements de référence sont d'une part, une interaction onde de choc / couche limite avec décollement et, d'autre part, une oscillation forcée d'une onde de choc. Dans ces deux configurations, la couche limite déstabilisée par le choc est turbulente, sachant que des interactions laminaire et transitionnelle ont été étudiées par ailleurs (voir la liste de publications). Le chapitre suivant montre les résultats de l'effet de dispositifs de contrôle (passif et actif) sur ces écoulements. Le dernier chapitre s'intéresse à la dynamique et aux instationnarités de l'interaction avec décollement, à la fois par une approche expérimentale et une analyse numérique.

Ce document est organisé de la façon suivante. Il comporte en plus du mémoire d'habilitation *stricto sensu*, mon curriculum vitae, ma liste de publications, mes activités d'encadrement ainsi que les principaux programmes de recherche auxquels j'ai participé. Enfin, les quatre publications dont les résultats ont majoritairement servi à l'élaboration de ce mémoire sont compilées en annexe par ordre chronologique.

2. ECOULEMENTS DE REFERENCE

L'ensemble de mes travaux expérimentaux présentés dans ce mémoire a été obtenu dans la soufflerie de recherche S8Ch du Laboratoire de Mécanique des Fluides (LMF) basé sur le centre de Meudon de l'ONERA. Cette soufflerie a permis depuis de nombreuses années de développer et de valider des moyens de mesures optiques (LDV, PIV, PSP) et de tester des dispositifs de contrôle des écoulements compressibles avec présence d'une onde de choc (normale ou oblique selon la valeur du nombre de Mach nominal).

2.1. Soufflerie de recherche S8Ch

La soufflerie S8Ch est une soufflerie continue alimentée par un air asséché prélevé à la pression atmosphérique. Un dessiccateur est placé en amont du circuit afin de contrôler son taux d'humidité : durant l'essai, l'élévation de la température réservoir de l'écoulement reste inférieure à 2°C et le point de rosée est stabilisé autour de –50°C. Le canal transsonique est rectangulaire dans sa section d'entrée, de hauteur 100mm et de largeur (d'envergure) 120mm (voir Fig. 1). La veine d'essais est constituée d'une paroi supérieure rectiligne et d'une paroi inférieure équipée d'un contour profilé (ou d'une bosse). La forme de la bosse a été définie de manière à produire une interaction forte entre la couche limite et le choc lorsque celui-ci est placé sur la partie aval de la bosse, ce qui correspond à un nombre de Mach de l'écoulement de l'ordre de 1,45 pour lequel l'écoulement est massivement décollé. D'autre part, un hublot est intégré au plafond de la veine d'essais afin de réaliser des mesures optiques (principalement de la PIV, voir Fig. 3) : le faisceau laser illumine la région d'interaction par le haut et la caméra est placée en regard d'un hublot latéral de la veine.

Un second col de section variable est localisé dans le plan de sortie de la veine d'essais. Lorsqu'il est amorcé, une onde de choc est générée dans l'écoulement dont la position quasi-stationnaire peut être ajustée précisément et de manière reproductible au cours des essais. Des perturbations quasi-sinusoïdales de pression peuvent être introduites dans l'écoulement par l'intermédiaire d'une came elliptique positionnée au niveau du second col, en milieu de veine. La mise en rotation de cette came induit une variation périodique de la section du second col, ce qui provoque une oscillation forcée du choc dont l'amplitude dépend de la vitesse de rotation de la came. Pour ces essais, la fréquence d'oscillation du choc est égale à 30Hz et l'amplitude de l'oscillation induite est d'environ 30mm, ce qui rend le phénomène aisément observable (voir les études similaires de Sajben *et al.* et de Ott *et al.*, annexe A).

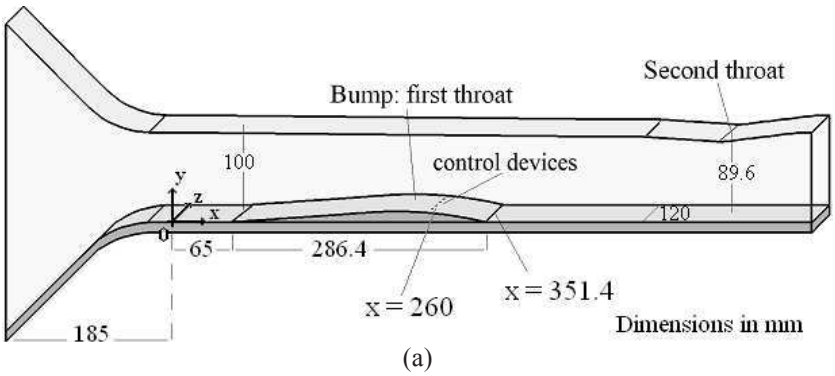

(a)

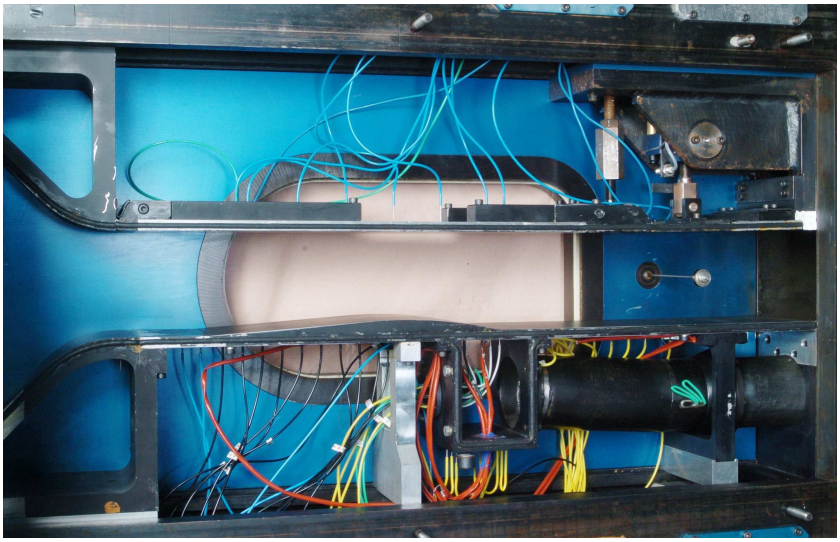

(b)

Figure 1 - Schéma (a) et photographie (b) de la veine d'essais de la soufflerie S8Ch

Les conditions réservoir, à savoir la température et la pression d'arrêt de l'écoulement amont, sont proches de l'ambiante, soient : p_{st}=0,96×10^5 ± 300 Pa and T_{st}=300 ± 10 K. De plus, des mesures du champ de vitesse ont été effectuées par vélocimétrie laser (LDV) au niveau de la partie amont de la bosse, où l'écoulement est encore subsonique. A l'abscisse X = 135mm (voir Fig. 1a pour la position de l'origine du système de coordonnées), la couche limite est pleinement turbulente avec les propriétés suivantes : épaisseur physique de 4mm, épaisseur de déplacement de 0,46mm, épaisseur de quantité de mouvement de 0,25mm et facteur de forme incompressible H_i égal à 1,6. Le nombre de Reynolds unitaire vaut environ 14×10^6 m^{-1} et le nombre de Reynolds basé sur l'épaisseur de quantité de mouvement de la couche limite subsonique amont est égal à 3500.

2.2. Moyens d'investigation

Un banc strioscopique est utilisé de manière systématique au cours des essais pour à la fois visualiser l'écoulement et contrôler les positions de l'onde de choc dans la veine. Le principe de la strioscopie repose sur l'effet de déviation des rayons lumineux dont les variations d'indice de réfraction dépendent du gradient de masse volumique de l'écoulement (loi de Gladstone-Dale). Le banc est monté classiquement en « Z », c'est-à-dire que le trajet optique et, donc, les miroirs sphériques côtés émission et réception sont disposés en symétrie ponctuelle par rapport au centre de la veine d'essais. Ce montage permet d'éliminer l'aberration chromatique des objectifs et d'obtenir un réglage en teinte sensible uniforme dans la totalité du champ de visualisation. Une lampe HBO de lumière blanche est utilisée comme source lumineuse, de préférence étendue, ce qui permet d'obtenir un échelonnement des nuances de gris en fonction de l'amplitude de la déviation, donc une image plus riche en information. Les modifications d'éclairement dans l'image sont produites par l'utilisation de diaphragmes strioscopiques (ici des couteaux d'occultation) destinées à mettre en évidence les rayons déviés à partir de la veine d'essais. La sensibilité de la strioscopie à couteaux est directionnelle : elle est en effet maximale pour une déviation orthogonale à l'arête du couteau et c'est donc la composante du gradient perpendiculaire au couteau qui est mise en évidence. Ainsi, pour faire ressortir une couche limite se développant sur une paroi horizontale, les couteaux sont positionnés à l'horizontal, alors que pour observer une onde de choc droite, les couteaux sont verticaux. L'acquisition des images est réalisée par une caméra à haute cadence

(Vision Research Phantom V710), avec un débit de 7 millions de pixels par seconde et un temps d'exposition de 300ns, et 60 000 images (464 x 360 pixels) sont acquises à une fréquence de 35kHz. Le grandissement étant d'environ 3 pixels par millimètre, la taille des images est de 140mm, ce qui permet de visualiser l'écoulement sur toute la hauteur du canal.

La paroi inférieure de la veine d'essais est équipée de 39 prises de pression statique situées sur une ligne décalée de 10mm de l'axe médian, et de 12 capteurs de pression instationnaire dont 6 placés sur l'axe médian et les 6 autres selon l'envergure (uniquement pour l'étude du cas de référence). Le schéma de la Figure 2 montre la répartition de ces capteurs sur la paroi de la veine ; les capteurs avec le symbole P sont situés sur la paroi pleine et ceux avec le symbole G sont sur la grille perforée lorsque le contrôle est étudié (voir Fig. 15). Les prises de pression statique ont un diamètre de 0,4mm et sont connectées à des capteurs Statham^{TM} par des tubes en vinyle. Les capteurs de pression instationnaire sont des Kulite^{TM} XCS093 de 15psi absolu ou différentiel, et ont un diamètre de 0,8mm. Les incertitudes de mesure (de pression) sont de ± 800Pa pour les Statham^{TM} et de ± 105Pa pour les Kulite^{TM}, respectivement. La définition du système de coordonnées est donnée sur la Figure 2 : l'origine O est sur la paroi inférieure et dans le plan d'entrée de la veine ; l'axe des X est la direction longitudinale, l'axe des Y la direction verticale et l'axe des Z le long de l'envergure, avec Z=0 dans le plan médian de la veine. L'origine de la bosse est à X=65mm ; sa longueur est de 286,4mm et son sommet égal à 12mm. Les dispositifs de contrôle mécaniques (VGs) sont positionnés en X=261,4mm, soit 10mm en aval du sommet de la bosse.

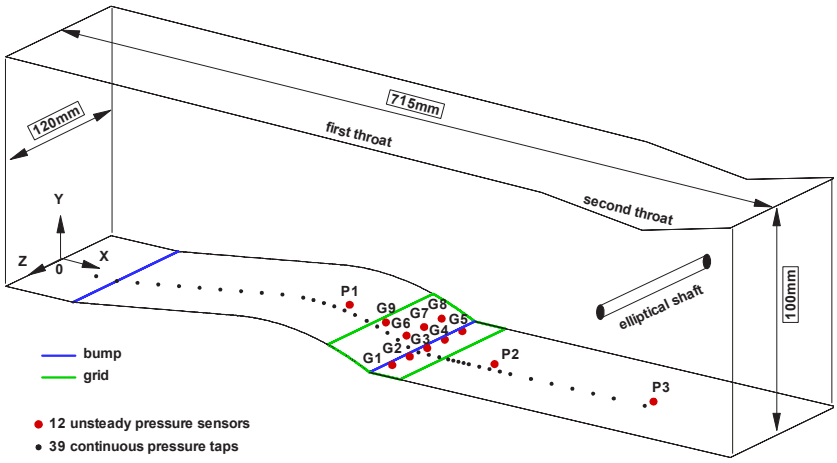

Figure 2 - Schéma de la localisation des prises de pressions statique et instationnaire dans la veine d'essais

Les mesures de champ dans la région d'interaction sont obtenues principalement par des techniques optiques (PIV, LDV). La PIV (Particle Image Velocimetry) s'est fortement développée ces dernières années en soufflerie car c'est un outil de mesures non intrusif de l'écoulement. Ce dernier est ensemencé de particules de très faible dimension, appelées traceurs. Ces traceurs sont illuminés deux fois par une nappe laser avec un intervalle de temps très court pour ce type d'écoulement transsonique. Le traitement des images prises à ces deux instants connus permet de déterminer le déplacement des particules durant l'intervalle et ainsi de remonter au champ de vitesse. Les résultats présentés dans ce mémoire proviennent de mesures PIV 2C, c'est-à-dire pour deux composantes du vecteur vitesse pour lesquelles une seule caméra est utilisée. L'objectif est orienté perpendiculairement à la nappe laser et l'écoulement est analysé seulement lorsque le laser flashe (voir Fig. 3). Les mesures de l'écoulement sont faites dans un plan situé sur l'axe médian de la veine d'essais, où les effets

tridimensionnels dus aux couches limites des parois latérales sont négligeables. Cette hypothèse est en partie vérifiée car l'envergure du canal de la soufflerie est suffisamment grande pour que les écoulements de coin restent confinés près des parois.

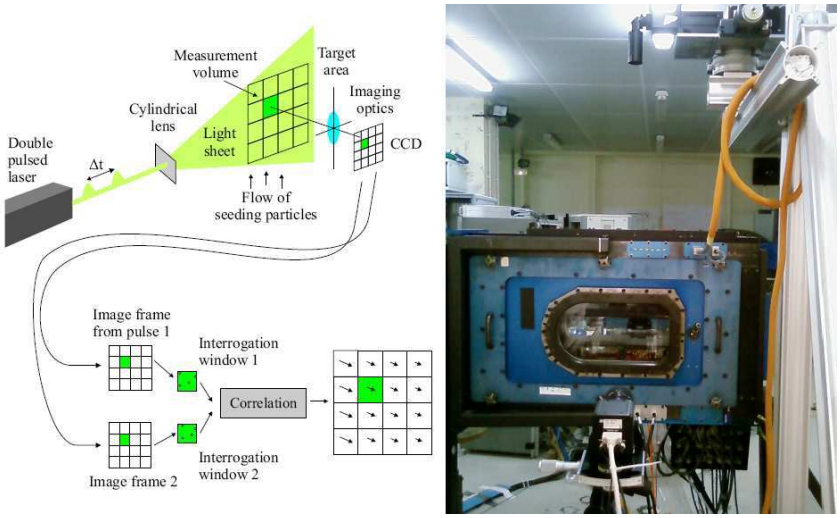

Figure 3 - Principe de fonctionnement de la PIV et photographie de l'équipement autour de la soufflerie S8Ch

Les nappes laser sont générées par un laser ND:YAG à double impulsion, qui délivre 150mJ par impulsion. L'intervalle de temps entre les deux impulsions est égal à 2,5µs pour le champ intégrant toute la région d'interaction et à 1,5µs pour le champ zoomé sur la couche limite. La caméra est équipée d'une lentille de focale 105mm pour le champ global et d'une télécentrique pour la couche limite, et comme le capteur CCD a une résolution de 2048 × 2048 pixels, le grandissement est d'environ 20 pixels/mm et 37 pixels/mm pour les deux champs étudiés. Un paramètre important qui peut affecter la qualité des résultats est la taille de la fenêtre d'interrogation : elle doit être assez grande pour contenir suffisamment de particules pour la corrélation, mais pas trop pour obtenir un champ de vecteurs relativement dense. Les résultats présentés sont des champs globaux d'au moins 100 × 100 vecteurs, avec un vecteur pour 20 pixels, soit tous les millimètres. Pour la couche limite, la fenêtre d'interrogation est de 10 pixels, ce qui donne un champ de 200 × 200 vecteurs avec un vecteur tous les 300µm. Pour chaque essai, mille paires d'images (échantillons) sont acquises à 5,6Hz et environ quatre minutes sont nécessaires pour l'enregistrement des données. Un test de convergence statistique de ces données est effectué sur les champs de vitesses moyenne et fluctuante pour le nombre d'échantillons retenus.

Le post-traitement des images est réalisé avec le logiciel FOLKI-PIV développé à l'ONERA et basé sur une méthode itérative de corrélation directe utilisant une descente de gradient (Champagnat *et al.*, voir annexe C). Le logiciel utilise des processeurs graphiques (GPU) permettant d'accélérer les calculs d'un facteur 50 par rapport aux logiciels classiques reposant sur des algorithmes FFT. De plus, il peut détecter avec précision le déplacement d'une particule pour une taille de fenêtre d'interrogation variable (de quelques pixels à des centaines de pixels), ce qui permet de calculer une plage de vitesses très étendue (du subsonique au supersonique). Ainsi, à un déplacement de 30 pixels pour chaque couple d'images dans la région supersonique correspond un déplacement d'au moins 2 pixels par image dans le décollement, où la vitesse de recirculation est d'environ ±30m/s. En supposant une résolution de 0,1 pixel (conventionnelle en PIV), on obtient une très bonne précision de calcul de la vitesse, de l'ordre de 1m/s. Enfin, comme la réflexion du laser à la paroi engendre des erreurs de calcul de la couche limite, un masque est utilisé pour imposer une vitesse nulle

à la paroi. Afin de déterminer avec précision la position de la paroi, avant chaque acquisition, une mire d'étalonnage est placée dans la veine d'essais au niveau de la nappe laser et une image est enregistrée pour pouvoir calibrer correctement le masque.

La LDV (Laser Doppler Velocimetry) est une autre technique de mesures non intrusive de l'écoulement. Les résultats présentés dans ce mémoire sont issus uniquement de la configuration d'oscillation forcée du choc, à la fréquence de 30Hz. Les mesures des deux composantes du vecteur vitesse sont synchronisées à un signal dépendant de la position de la came elliptique en rotation. Contrairement à la PIV, la LDV est une technique de mesure ponctuelle : le volume de mesure de quelques dizaines de micron est issu de la focalisation des faisceaux laser. Le maillage comprend 5000 points de mesure, avec un raffinement dans les couches limites, et il couvre entièrement la région d'oscillation du choc dans la veine.

Une technique de moyennage de phase, proposée par Hussain and Reynolds (voir annexe A), est utilisée pour post-traiter les signaux LDV conditionnés et calculer le champ de vitesse. Cette technique permet de découpler la composante « cohérente » du signal, relative à l'excitation périodique de l'écoulement, et la composante aléatoire relative aux fluctuations. La vitesse instantanée *U(X,t)* se décompose alors en trois termes :

$$U(X,t) = \overline{U}(X) + \widetilde{U}(X,t) + U'(X,t)$$

où $\overline{U}(X)$ est la composante de moyenne d'ensemble, $\widetilde{U}(X,t)$ la composante cyclique et *U'(X,t)* la composante fluctuante. La composante de moyenne de phase est définie comme :

$$< U(X,t) > = \overline{U}(X) + \widetilde{U}(X,t)$$

La composante fluctuante restante peut être interprétée comme un résidu d'évènements dans l'écoulement qui ne sont pas en phase avec le mouvement d'ensemble. Dans l'écoulement étudié, la vitesse moyenne de phase est déterminée à l'aide d'un signal temporel, et une période d'oscillation du choc est décomposée en 60 classes prises tous les 6°. Le début de la période est repéré par un marqueur localisé sur la came elliptique. L'utilisation d'un appareil RMR (Rotating Machinery Resolver de TSI) permet de classer au cours du temps chaque échantillon dans la période.

L'ensemencement de l'écoulement est un point critique pour assurer une bonne qualité de mesure par des techniques optiques, en particulier lorsque les écoulements étudiés sont compressibles avec présence d'ondes de choc, qui engendrent des problèmes de traînage des particules. D'autre part, la présence de régions décollées avec des écoulements de retour pose des problèmes à la fois de déficit de particules et de pollution des hublots de la veine d'essais, qui dégradent de manière significative les mesures. Le traceur le plus performant pour cette classe d'écoulements est du Di-Ethyl-Hexyl-Sebacate (DEHS) dont les particules submicroniques liquides (de l'ordre de 0,5µm) sont générées par un atomiseur (Topas ATM 210) placé dans la chambre de tranquillisation de la soufflerie, afin d'obtenir une concentration de particules la plus homogène possible dans la veine d'essais. Le nombre de Stokes du DEHS vaut environ 0,07 et garantit bien que ce traceur est un scalaire passif pour l'écoulement.

2.3. Interaction onde de choc / couche limite turbulente avec décollement

Plusieurs études menées dans le canal transsonique ont montré qu'il existe une position optimale de l'onde de choc pour laquelle l'extension spatiale de la zone décollée est maximale (voir annexe A). Cette configuration est obtenue quand l'ouverture du second col est égale à 89,6mm (voir Fig. 1a), ce qui correspond à une position du choc normal dans la veine à 12,6mm en aval de la fin de la bosse. Le nombre de Mach juste en amont du choc normal vaut environ 1,45 et juste en aval du choc, le nombre de Mach est de l'ordre de 0,75.

Dans ce cas, l'interaction est forte puisqu'elle provoque le décollement de la couche limite et elle se caractérise par la formation d'une structure de choc en lambda, comme le montre la visualisation strioscopique de la Figure 4. Cette structure de choc s'explique par le fait que la branche amont du choc (nommée 1 sur la Fig. 4) est un choc oblique faible dont l'intensité est fonction de la valeur du nombre de Mach amont. Lorsqu'il rencontre le choc fort quasi-normal (nommé 2 sur la Fig. 4), l'écoulement en aval de ces chocs n'a pas les mêmes états de pression et de vitesse (en module et en direction). Afin d'assurer la compatibilité de propriétés entre ces deux écoulements adjacents, un choc fort se crée pour former la structure de choc en lambda (branche aval du choc, nommée 3 sur la Fig. 4). Les chocs se rejoignent en un point appelé le point triple (point c sur la Fig. 4) d'où part une ligne de glissement à travers laquelle la pression statique se conserve. Bien que l'écoulement redevienne en principe subsonique en aval du système de choc, il peut subsister une « poche » d'écoulement faiblement supersonique localisée juste en aval de la branche aval du choc. L'existence de cette « poche » dépend notamment de la déviation de l'écoulement corrélée à la forme de la paroi (ici la bosse) ainsi que de l'extension de la zone décollée. Le décollement peut être matérialisé sur l'image strioscopique de la Figure 4 : près de la paroi, entre les points notés a et b, il existe une zone dans laquelle les structures turbulentes, générées au niveau du pied du choc de tête pour former la couche de cisaillement, ne sont pas visibles.

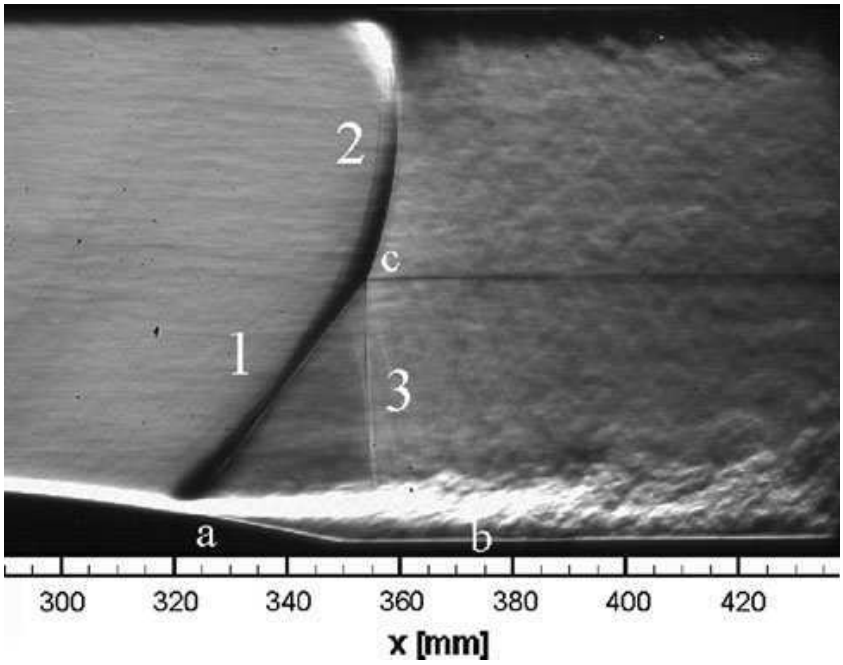

Figure 4 - Visualisation strioscopique de la région d'interaction

La Figure 5 montre la structure du choc en lambda obtenue à partir de mesures PIV de la composante de vitesse longitudinale. La « poche » d'écoulement supersonique est mise en

évidence par le tracé de la ligne sonique (en noir). La bulle de recirculation au niveau de décollement est matérialisée par des valeurs négatives de la vitesse allant jusqu'à –40m/s (en bleu), soit environ un ordre de grandeur inférieur à l'écoulement en amont de l'onde de choc. Un zoom au niveau de la bulle de recirculation est tracé sur la Figure 6, où sont superposés les vecteurs vitesse (en fait, un vecteur sur cinq pour la clarté du tracé). Le décollement s'étend du pied de choc, à $X \approx 336$mm, jusqu'à l'abscisse $X \approx 378$mm. Le logiciel FOLKI-PIV permet d'obtenir ce résultat à partir d'une seule paire d'images, sans acquisition supplémentaire d'images zoomées sur le décollement. En revanche, la couche limite turbulente en amont de l'interaction n'est pas correctement résolue à partir de sa zone logarithmique, puisqu'au mieux on dispose d'un vecteur tous les 300µm (avec une fenêtre d'interrogation de 10 pixels).

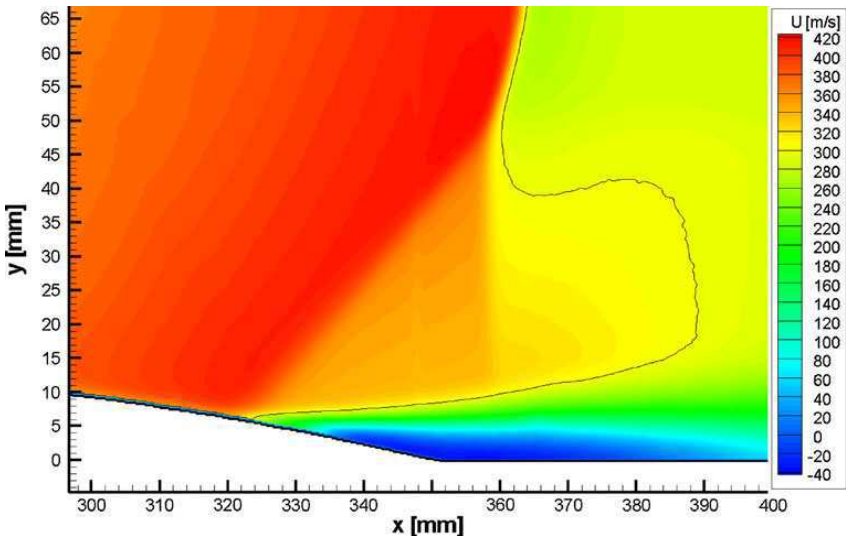

Figure 5 - Iso-contours de la composante de vitesse longitudinale dans la région d'interaction et ligne Mach = 1 en noir

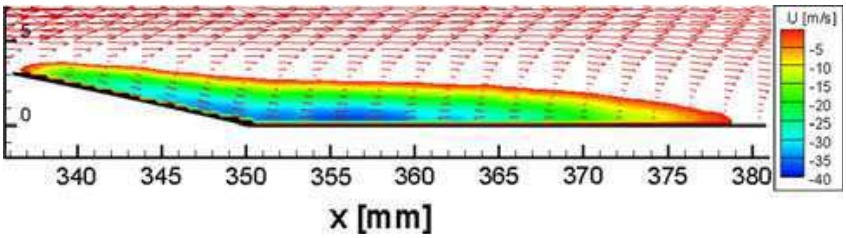

Figure 6 - Zoom au niveau de la bulle de recirculation
Iso-contours de la composante de vitesse longitudinale et tracés des vecteurs vitesse (uniquement 1 vecteur sur 5 pour la clarté de la figure)

Le post-traitement des résultats PIV permet de calculer les valeurs RMS des composantes fluctuantes des vitesses longitudinale et verticale. On en déduit le champ turbulent associé par l'intermédiaire de la pseudo (uniquement à deux composantes) énergie cinétique turbulente k et la tension de cisaillement $-\overline{u'v'}$. L'évolution de l'énergie cinétique turbulente k, normalisée par la vitesse $U = 300$m/s correspondant à une valeur moyenne de la vitesse dans la couche de cisaillement, est présentée sur la Figure 7. La couche de cisaillement prend naissance dès que la couche limite décolle et le niveau maximum de turbulence est atteint dans celle-ci au niveau de la bulle de recirculation, puis se relaxe lentement lorsque l'écoulement est recollé à la paroi. Ces fluctuations correspondent aux structures turbulentes d'échelle moyenne visibles sur la strioscopie de la Figure 4. Sous la couche de cisaillement,

de X = 340mm à X = 360mm, le faible niveau de k signifie que la recirculation de l'écoulement dans le décollement s'effectue de manière quasi-stationnaire.

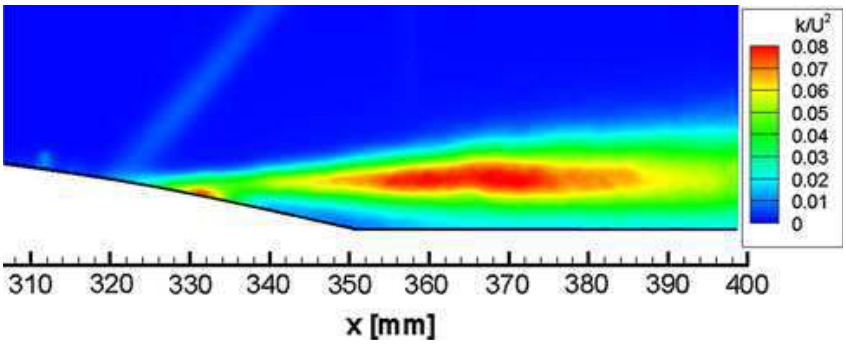

Figure 7 - Iso-contours de la pseudo (2D) énergie cinétique turbulente k normalisée

L'évolution de la tension de cisaillement normalisée $-\overline{u'v'}$ est présentée sur la Figure 8. En écoulement transsonique, on suppose que le gradient de masse volumique est faible à travers la couche limite ; ainsi, la mesure de $-\overline{u'v'}$ constitue une bonne approximation de la valeur exacte de la tension de cisaillement issue du tenseur de Reynolds. Le maximum (adimensionné) de $-\overline{u'v'}$ vaut 0,023 et est en accord avec la valeur de 0,026 obtenue par des mesures LDV sur une configuration similaire pour laquelle le choc était positionné légèrement plus en amont dans la veine (Délery et Bur, voir annexe C). Ce maximum est localisé au voisinage du point de recollement (voir Fig. 6) et de grosses structures tourbillonnaires se forment dans la couche de cisaillement (visibles sur la Fig. 4). De ce fait, le niveau de tension de cisaillement croît plus lentement dans l'écoulement comparé à celui de l'énergie cinétique turbulente. La branche amont du choc en lambda apparaît sur le champ turbulent : une ligne oblique juste en amont du décollement (voir Fig. 7) indique une croissance de fluctuations au passage de la discontinuité et souligne le caractère instationnaire de ce choc de tête. La mesure de ces fluctuations est délicate à cause de problèmes d'aberration optique dus aux indices de réfraction très inhomogènes à travers le choc (Humble *et al.* ; Mitchell *et al.*, voir annexe C).

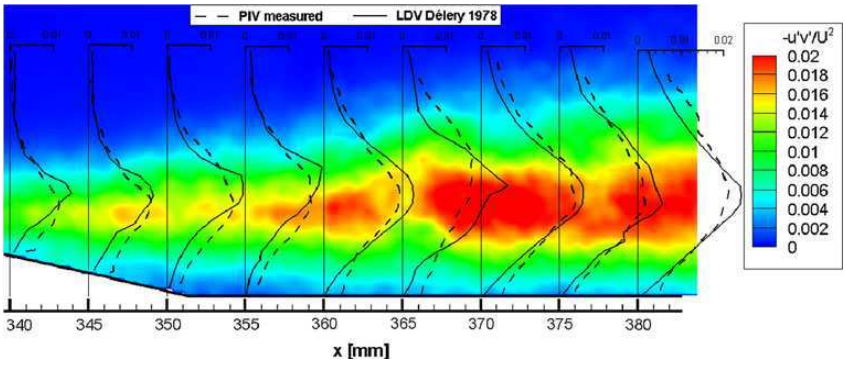

Figure 8 - Iso-contours de la tension de cisaillement $-\overline{u'v'}$ normalisée
Champ et lignes pointillées : mesures PIV et lignes pleines : mesures LDV

En conclusion, le champ moyen de l'écoulement est résolu par PIV avec une précision de 1m/s et une résolution spatiale de 1mm ; en zoomant la fenêtre d'interrogation dans la région de proche paroi, la couche limite en amont de l'interaction est mesurée jusqu'à 300µm de la paroi, ce qui reste perfectible notamment vis-à-vis de mesures LDV obtenues avec une

focale courte pour lesquelles le volume de mesure est réduit à 50µm. La région d'interaction est correctement prédite, avec la structure de choc en lambda, la bulle de recirculation (et l'écoulement de retour à vitesse négative) et la couche de cisaillement qui se développe à partir du pied de choc. Les mesures des fluctuations de vitesse permettent de mettre en évidence une production importante de turbulence se développant dans la couche de cisaillement, avec la présence de grosses structures tourbillonnaires, puis une lente relaxation vers un état de couche limite à l'équilibre en aval de l'interaction.

2.4. Oscillation forcée de l'onde de choc

L'oscillation de l'onde de choc est forcée par une évolution périodique de la section d'un col aval, au moyen d'une came elliptique en rotation placée au voisinage de ce col, au milieu du canal (voir Fig. 1). La came en rotation génère des ondes de pression qui vont remonter l'écoulement. La fréquence de rotation de la came est variable, entre 0 et 180Hz (expériences similaires de Sajben *et al.* et de Ott *et al.*, voir annexe A). La fréquence d'étude retenue est de 15Hz, ce qui correspond à une fréquence d'oscillation du choc de 30Hz due à la forme elliptique de la came. L'amplitude d'oscillation correspondante du choc à cette fréquence d'excitation est d'environ 30mm. Ainsi, durant le cycle d'oscillation de l'onde de choc, la couche limite est à la fois attachée et décollée, selon l'intensité du choc et le gradient de pression adverse produit par la courbure de la paroi (bosse).

La Figure 9 montre les visualisations strioscopiques de l'écoulement pour les deux positions les plus extrêmes de l'onde de choc dans le canal, à la fréquence d'oscillation de 30Hz. Même si on retrouve une structure de choc en lambda pour les deux positions, la taille de ce lambda diffère selon l'état de la couche limite. En position aval, la couche limite reste attachée alors qu'en position amont, elle est décollée et une couche de cisaillement se développe avec la formation de grosses structures cohérentes.

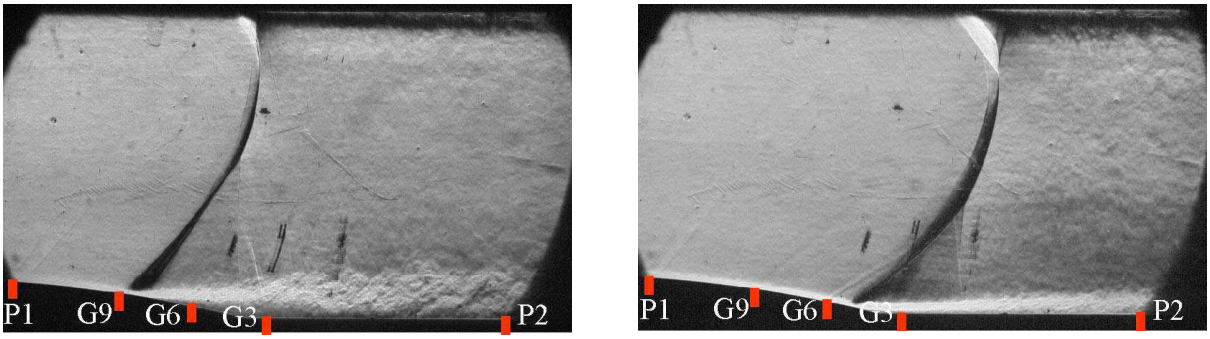

(a) position amont (b) position aval

Figure 9 - Positions de l'onde de choc dans le canal pour la fréquence d'oscillation de 30Hz (et localisations des capteurs Kulite dans le plan médian)

La Figure 10 présente l'évolution longitudinale des spectres de fluctuations de pression pour la fréquence d'oscillation de 30Hz obtenus à partir des signaux mesurés par les capteurs Kulite situés sur l'axe médian de la veine d'essais (voir Figs. 2 et 9). Les spectres sont calculés en SPL (Sound Pressure Level, en dB) par la formule suivante :

$$SPL(dB) = 20 \times log_{10}\left(\frac{\sqrt{S_{p'p'}}}{p_{ref}}\right)$$

où $S_{p'p'}$ est le module du spectre (en Pa^2) et p_{ref} la pression de référence égale à 2×10^{-5} Pa.

La fréquence d'échantillonnage est de 6000Hz pour chaque capteur et les spectres sont calculés à partir de 50 blocs de 8192 échantillons. Le spectre du capteur P1 (à X=281,4mm) est plat car il est localisé dans la région supersonique de l'écoulement, non affecté par les perturbations aval. Le spectre de G9 (à X=316,4mm) a un pic d'énergie à la fréquence fondamentale 30Hz de l'oscillation du choc, et quelques harmoniques. Ces pics sont de faible intensité car le capteur est situé à la limite amont de l'oscillation du choc. Le spectre de G6 (à X=336,4mm) possède la fondamentale et de nombreuses harmoniques très énergétiques car le capteur est situé dans la région d'oscillation. Le spectre de G3 (à X=356,4mm, juste en aval de la bosse) ne contient plus que la fondamentale et une seule harmonique de faible énergie La fondamentale en G3 est plus faible que celle en G6, à savoir 160dB contre 170dB. Ceci est dû à la position du capteur G3 toujours en aval du choc de tête (voir Fig. 9), ce choc engendrant le plus de fluctuations dans l'interaction. Les capteurs P2 (à X=421,4mm) et P3 (à X=575mm, au niveau de la came) donnent la même forme de spectre car ils sont situés dans la région subsonique en aval de l'interaction et ils restituent principalement les perturbations de pression aval.

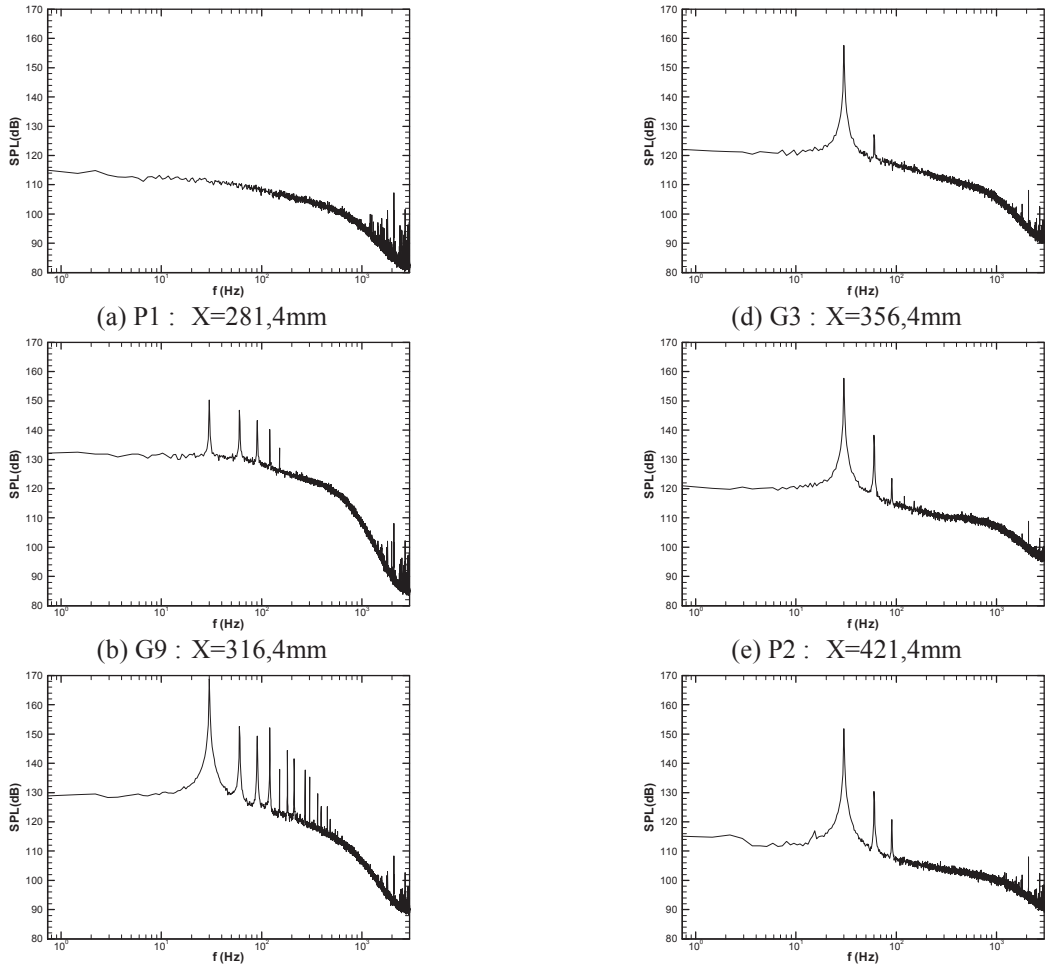

(a) P1 : X=281,4mm (d) G3 : X=356,4mm

(b) G9 : X=316,4mm (e) P2 : X=421,4mm

(c) G6 : X=336,4mm (f) P3 : X=575mm

Figure 10 - Evolution longitudinale des spectres de fluctuations de pression pour la fréquence d'oscillation de 30Hz

La Figure 11 donne l'évolution du nombre de Mach obtenue par mesures LDV conditionnelles durant une période T d'oscillation du choc à la fréquence de 30Hz.

L'amplitude d'oscillation du choc est égale à 30mm et on retrouve bien la structure de choc en lambda dont la taille évolue selon la position du choc, comme déjà analysé sur les visualisations strioscopiques (voir Fig. 9). Lorsque le choc est en position amont (à t=0), le nombre de Mach devant le système de choc vaut environ 1,3. L'extension longitudinale du bulbe de décollement est égale à 62mm, de X=328mm to X=390mm, avec une vitesse de retour maximale de –77m/s. Quand le choc est en position aval (à t=T/2), le nombre de Mach devant le choc est égal à 1,5 et la couche limite reste attachée.

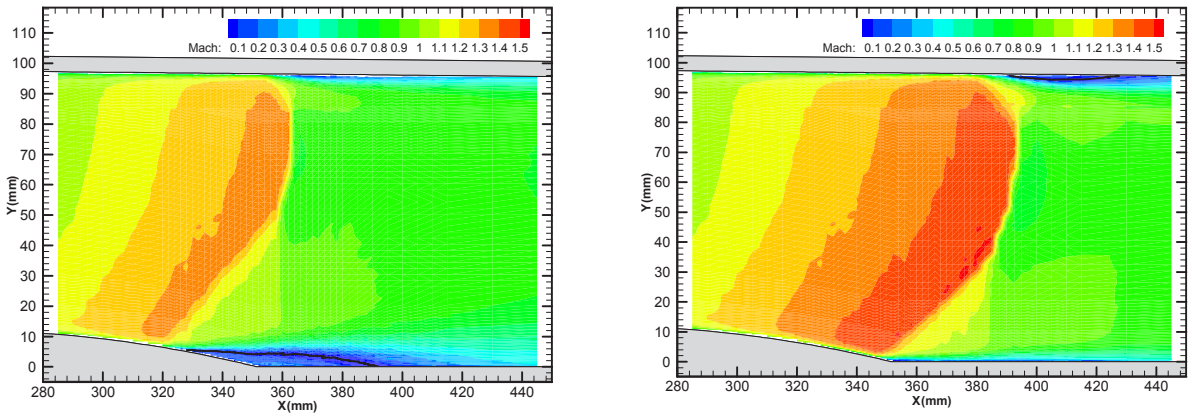

(a) position amont (t=0) (b) position aval (t=T/2)

Figure 11 - Iso-contours du nombre de Mach obtenus par mesures LDV conditionnelles durant une période T d'oscillation du choc à la fréquence 30Hz

En conclusion, l'analyse spectrale des signaux de pression a montré que la réponse des capteurs est pilotée par l'oscillation de la branche amont du choc en lambda. Le traitement des mesures LDV par analyse conditionnelle, grâce à la synchronisation des acquisitions à un top par tour au niveau de la came tournante, a permis de quantifier avec précision l'évolution du bulbe de décollement et de la couche de cisaillement pendant le cycle d'oscillation du choc.

3. CONTROLE DES ECOULEMENTS

3.1. Etude de dispositifs de contrôle

Le contrôle des écoulements de référence, et plus particulièrement de la région du décollement, peut se faire par deux types de dispositifs distincts, classés en contrôle passif et contrôle actif. Les actionneurs dits passifs se définissent par le fait qu'ils n'utilisent aucune énergie auxiliaire pour agir sur l'écoulement.

Les générateurs de tourbillons mécaniques (en anglais, « vane-type vortex generators » ou VGs) sont des actionneurs passifs utilisés pour augmenter la quantité de mouvement du fluide près de la paroi par un transfert d'énergie, créé par vorticité, de l'écoulement externe vers la couche limite (voir annexe B). Les VGs sont des éléments simples ou profilés, disposés en rangée avec un angle de dérapage ou d'incidence afin de produire des tourbillons dans le sens longitudinal de l'écoulement. Leur dimension doit être optimisée pour ne pas produire des discontinuités trop fortes dans l'écoulement, type ondes de compression qui pourraient interférer avec le système de choc, ou engendrer de la traînée de frottement. Les VGs sont souvent testés pour agir sur le décollement de couche limite, et ainsi augmenter la portance ou repousser la limite d'apparition du tremblement d'un profil d'aile.

Les actionneurs passifs testés sur les deux écoulements de référence (interaction choc / couche limite avec décollement et oscillation forcée de l'onde de choc) sont des VGs mécaniques localisés en amont de la région d'interaction. Ce sont des éléments triangulaires calés avec un angle de dérapage de 18° par rapport à la direction principale de l'écoulement. Ils sont positionnés par paires selon l'envergure de la veine d'essais, soit en position « co-rotative » pour générer les tourbillons de même signe, soit en position « contra-rotative » pour créer des tourbillons de signe opposé. Plusieurs paramètres géométriques sont testés (voir Fig. 12 et Pauley *et al.* ; Pearcey et Lin, voir annexe B). Le paramètre dimensionnant est la hauteur h des VGs en regard de l'épaisseur physique δ de la couche limite turbulente en amont de l'interaction, mesurée par LDV à 4mm. Deux hauteurs de VGs sont retenues : des VGs « conventionnels » (h/δ=1, notés CoC et C) sont comparés à des « sub-VGs » (h/δ=0.5, notés CoS et S). Pour les VGs « contra-rotatifs », l'espacement λ entre chaque paire de VGs est étudié (λ/h=10 et 5, respectivement pour les VGs C1, S1 et C2, S2).

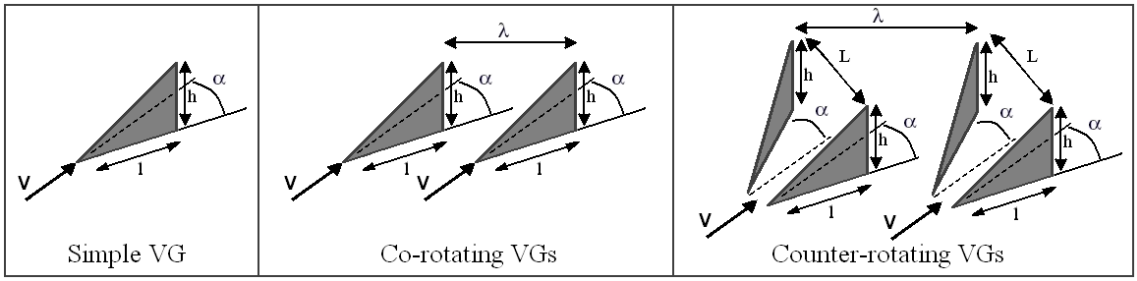

Figure 12 - Configurations et dimensionnements des VGs mécaniques

De plus, le nombre de VGs a été adapté pour chaque configuration afin de couvrir entièrement l'envergure de la veine d'essais. Pour le choix de la position des VGs vis-à-vis de l'interaction, on introduit le paramètre $\Delta X_{VG} / h$, dans lequel ΔX_{VG} est la distance entre les VGs et la ligne de décollement au niveau du pied de choc. La position retenue pour la ligne de VGs est en X=260mm, soit 10mm en aval du sommet de la bosse (voir Fig. 1). Elle résulte d'une étude paramétrique à partir de simulations numériques RANS 3D dont l'objectif était de supprimer le décollement de la couche limite. La distance normalisée $\Delta X_{VG} / h$ est alors égale à 16 pour les VGs « conventionnels » et à 32 pour les « sub-VGs », ce qui est dans la plage de valeurs citées dans la littérature (positions optimales pour : $10 < \Delta X_{VG} / h < 50$, voir annexe B). Au final, six configurations de VGs sont testées sur les écoulements (voir Tableau 1 et Fig. 13). La Figure 14 montre les VGs « contra-rotatifs » C2 en place sur la paroi inférieure de la veine d'essais, à 10mm en aval du sommet de la bosse.

	VGs « co-rotatifs »		VGs « contra-rotatifs »			
	CoC1	CoS1	C1	C2	S1	S2
h/δ	1	0.5	1	1	0.5	0.5
l/h	2.5	2.5	2.5	1.25	2.5	1.25
L/h	-	-	3	1.5	3	1.5
λ/h	6	6	10	5	10	5
Nombre de VG	5	9	3	5	5	11

Tableau 1 - Paramètres géométriques des VGs mécaniques

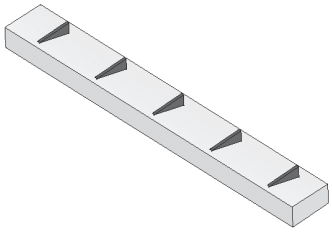

CoC1 : VGs « co-rotatifs » conventionnels

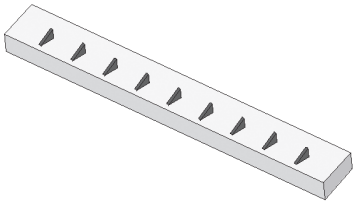

CoS1 : Sub-VGs « co-rotatifs »

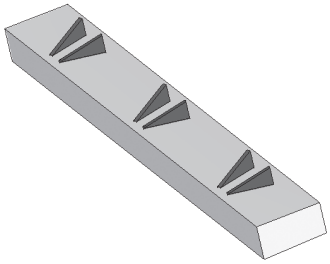

C1 : VGs « contra-rotatifs » conventionnels

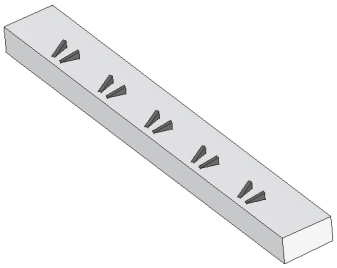

S1 : Sub-VGs « contra-rotatifs »

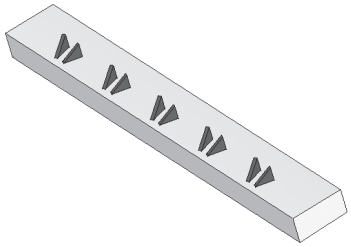

C2 : VGs « contra-rotatifs » conventionnels

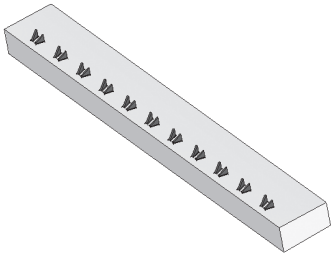

S2 : Sub-VGs « contra-rotatifs »

Figure 13 - Configurations testées de VGs mécaniques

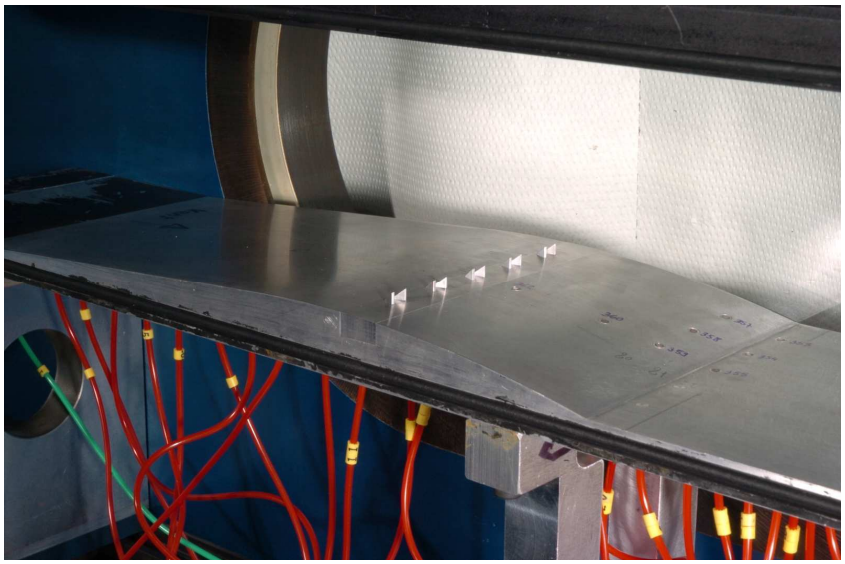

Figure 14 - Photographie des VGs « contra-rotatifs » C2 sur la paroi inférieure de la veine d'essais

Le second type de contrôle, par des actionneurs dits actifs, nécessite un apport d'énergie auxiliaire pour agir sur l'écoulement. En particulier, cette source d'énergie peut être une quantité de fluide ajoutée (soufflage) ou prélevée (aspiration) dans la région à contrôler. Dans les deux cas, le débit fluidique est un paramètre crucial qui va permettre d'optimiser le dispositif de contrôle en regard de la configuration aérodynamique à étudier. Pour le soufflage, l'objectif est d'injecter du fluide dans la couche limite pour augmenter la quantité de mouvement et la rendre plus résistante au décollement. L'inconvénient de cette technique de soufflage est qu'elle engendre une augmentation de la traînée. L'objectif du contrôle par aspiration est de supprimer le décollement en prélevant du fluide soit de manière locale, par une fente, soit de manière répartie à travers une grille perforée. Ce dernier est testé sur la configuration d'oscillation forcée de l'onde de choc (voir Fig. 15). L'aspiration de fluide est réalisée à travers une grille perforée dont les caractéristiques sont : une porosité de 5,67% et des trous de diamètre 0,3mm, inclinés à 45° vers l'aval par rapport à la paroi sur la première moitié de la grille, et à 90° sur sa deuxième moitié. La cavité est placée dans la région d'interaction, à cheval sur la bosse et le plancher rectiligne, avec une longueur de 70mm et une profondeur de 110mm. Elle est reliée à une pompe auxiliaire par une canalisation circulaire qui est équipée de col sonique de différents diamètres permettant de figer les valeurs du débit d'aspiration. Si aucun débit n'est prélevé, alors le dispositif de contrôle devient passif. Dans ce cas, une recirculation naturelle de fluide s'opère à travers la grille perforée, due à la différence de pression de part et d'autre de l'onde de choc : le fluide est aspiré en aval du choc à travers la grille et est réinjecté en amont du choc dans la couche limite.

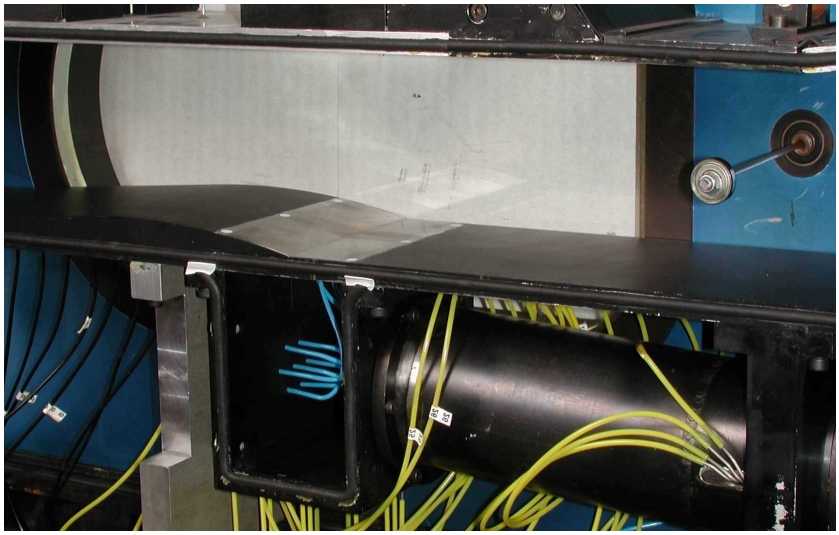

Figure 15 - Photographie du dispositif de contrôle actif dans la région d'interaction

3.2. Résultats sur les écoulements

Une comparaison des visualisations strioscopiques de la configuration d'interaction onde de choc / couche limite est montrée sur la Figure 16 entre l'écoulement de référence et l'écoulement contrôlé par les VGs « contra-rotatifs » C2 (voir Fig. 14). On retrouve la structure de choc en lambda, le décollement et la couche de cisaillement dans le cas sans contrôle (voir Fig. 16a). L'onde visible en amont de l'interaction, due à la jonction entre la bosse et l'élément fabriqué à l'emplacement des VGs, est de faible intensité et ne perturbe pas l'écoulement. Dans le cas avec contrôle (voir Fig. 16b), la taille du choc en lambda est réduite, le point triple se situant plus près de la paroi. Ceci est lié à la diminution de la région de décollement sous l'action des VGs et à l'accroissement de la couche de cisaillement (avec

la présence de grosses structures cohérentes). D'autre part, la forme des VGs engendre la formation d'un faisceau de détentes suivi d'ondes de compression dans l'écoulement, mais leurs propagations font qu'elles ne viennent pas perturber la région d'interaction. On peut aussi observer les trajectoires des tourbillons créés par les VGs en amont de l'interaction.

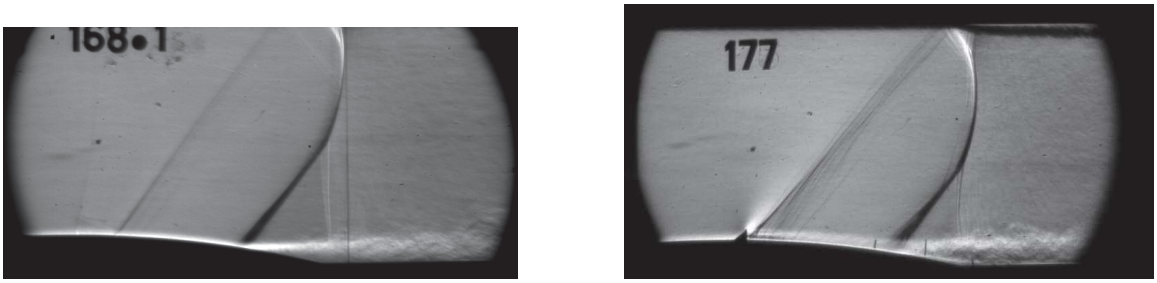

(a) écoulement de référence (b) écoulement contrôlé

Figure 16 - Visualisations strioscopiques de l'interaction onde de choc / couche limite sans contrôle (a) et avec contrôle par les VGs « contra-rotatifs » C2 (b)

Les répartitions de pression statique (sur l'axe médian de la veine d'essais) pour la configuration d'interaction onde de choc / couche limite sont tracées sur la Figure 17 pour le cas de référence et les six cas avec contrôle par les VGs mécaniques (voir Fig. 13). La région de décollement importante dans l'écoulement de référence correspond à la présence d'un quasi-plateau de pression suite à la recompression intense de l'écoulement à travers la branche amont du choc en lambda. Ce plateau de pression est fortement atténué sous l'action des VGs, dont l'efficacité semble accrue lorsque leur espacement diminue (S2 comparé à S1, C2 à C1). Ainsi, les onze paires de sub-VGs « contra-rotatifs » S2 ont la meilleure efficacité pour supprimer le décollement. Les perturbations dues à la présence des VGs (détentes et compressions observées sur la Fig. 16b) sont de faible intensité et n'ont qu'un effet très local sur le champ de pression pariétal. D'autre part, il est possible de diminuer l'impact des VGs, notamment sur la traînée, en imposant leur hauteur h à une valeur inférieure à celle de la ligne sonique de la couche limite en amont de l'interaction, mesurée à : h^*=0,5mm (voir annexe B). Or, vu les difficultés de fabrication pour reproduire des éléments de très faible dimension, tous les VGs testés ont des hauteurs plus importantes, à savoir : h/h^*=4 et 8 pour les « sub-VGs » et les VGs « conventionnels », respectivement.

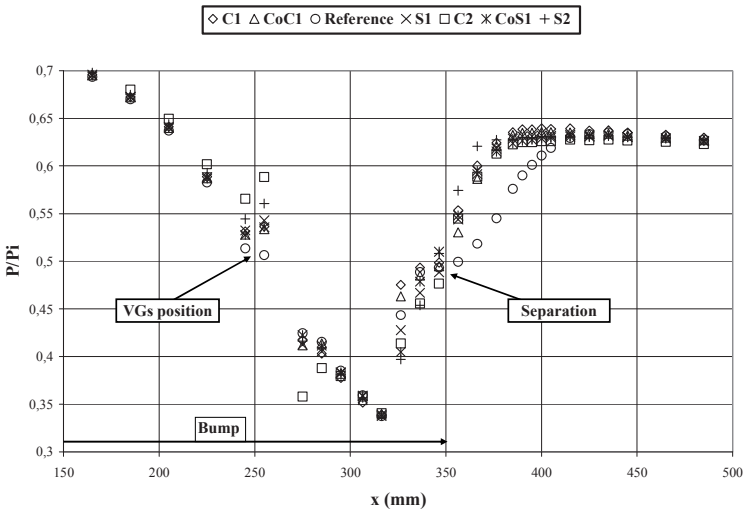

Figure 17 - Répartitions de pression statique pour la configuration d'interaction onde de choc / couche limite sans contrôle et avec contrôle par les VGs mécaniques

Une comparaison des visualisations pariétales par enduit visqueux coloré de la configuration d'interaction onde de choc / couche limite est montrée sur la Figure 18 entre l'écoulement de référence et l'écoulement contrôlé par les VGs C2. Dans le cas de référence, l'écoulement est à peu près invariant le long de l'envergure et la position longitudinale du décollement est quasi-constante, aux effets de bord près (matérialisée par la ligne en pointillé, qui est reportée à la même position dans le cas contrôlé, voir Fig. 18a et b). Une modification importante de la topologie du décollement apparaît dans le cas contrôlé par les VGs. Les lignes de frottement mettent en évidence la formation et la trajectoire des tourbillons issus des VGs, en amont de l'interaction. Le suivi des trajectoires montre la propagation de paires de tourbillons jusqu'à la région (ligne pointillée) correspondant au décollement de l'écoulement de référence. En aval de cette ligne, on observe une organisation tridimensionnelle des lignes de frottement, pseudo-périodique selon l'envergure avant contamination par la présence des parois latérales. Le recollement de la couche limite est donc partiel selon l'envergure : il est présent dans le sillage d'une paire de VGs mais des zones décollées (en forme de cellules) subsistent entre chaque paire de VGs. De plus, l'extension de ces cellules semble plus faible que celle du décollement de référence ; le recollement est plutôt localisé au voisinage de la fin de la bosse, en amont du point de recollement de référence.

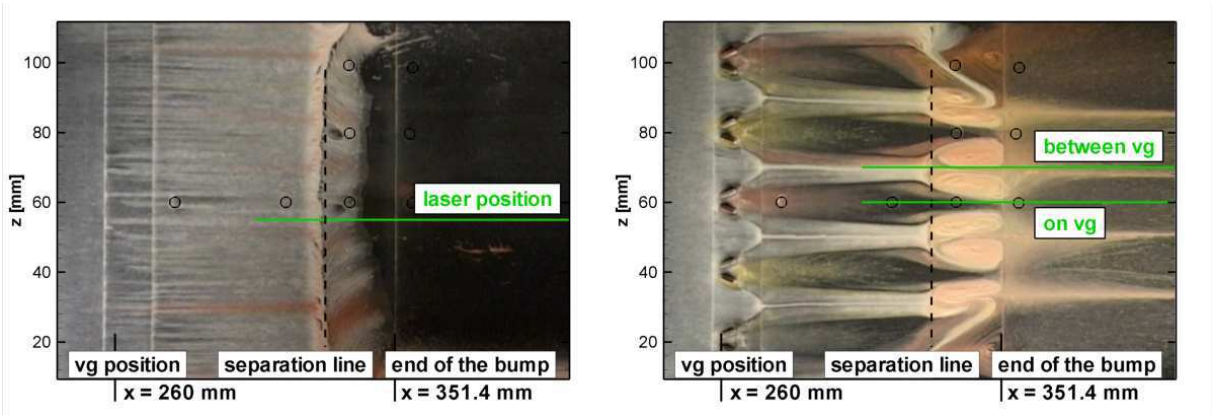

(a) écoulement de référence (b) écoulement contrôlé

Figure 18 - Visualisations par enduit visqueux de l'interaction onde de choc / couche limite sans contrôle (a) et avec contrôle par les VGs « contra-rotatifs » C2 (b)
La ligne verticale en pointillé indique la position du décollement du cas de référence (sur les deux figures)
Les cercles noirs pointent les lieux d'imprécisions de mesure dues à la présence des capteurs Kulite

Ces observations sont confirmées par des mesures PIV de la composante de vitesse longitudinale dans la région d'interaction, entre l'écoulement de référence et l'écoulement contrôlé par les VGs C2 (voir la Figure 19). Les mesures en présence des VGs sont réalisées selon deux plans longitudinaux : un plan au milieu de la paire centrale de VGs, qui coïncide avec l'axe médian de la veine d'essais, et un autre localisé entre deux paires de VGs. Ces plans sont notés « on VG » et « between VG », respectivement, sur les Figures 18 à 20. Le premier plan permet de décrire le sillage turbulent créé par les VGs, tandis que le second permet de quantifier la croissance des tourbillons. Le bulbe de recirculation a complètement disparu dans le plan « on VG » du sillage de la paire de VGs, tandis qu'il subsiste en partie dans le plan « between VG » entre deux paires de VGs. L'extension de la bulle est réduite par rapport au cas de référence, le point le recollement étant situé juste après la fin de la bosse (voir la ligne de vitesse nulle en noir sur la Fig. 19). De plus, la couche de cisaillement est générée avec un angle d'inclinaison plus verticale sous l'action de la vorticité des tourbillons, tendance déjà observée sur le cliché strioscopique (voir Fig. 16b).

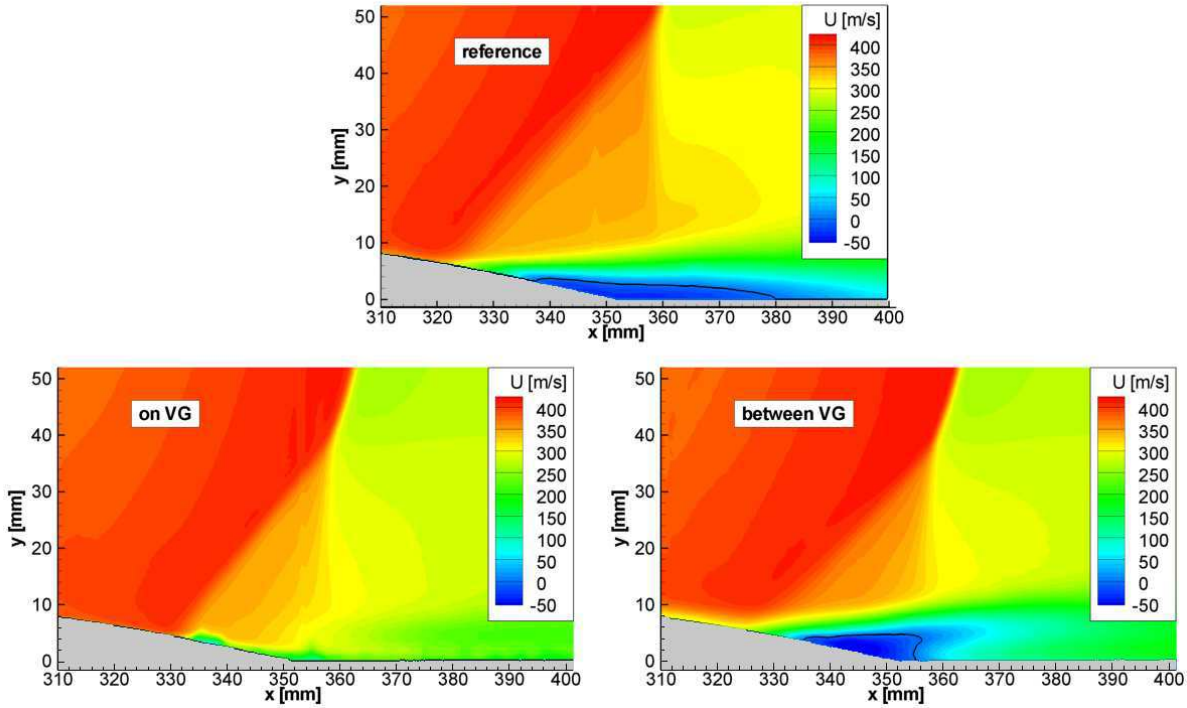

Figure 19 - Iso-contours de la composante de vitesse longitudinale de l'interaction onde de choc / couche limite sans contrôle (haut) et avec contrôle par les VGs « contra-rotatifs » C2 (bas), et ligne U = 0 en noir

Les évolutions de la tension de cisaillement $-\overline{u'v'}$ normalisée dans la région d'interaction sont comparées sur la Figure 20 entre l'écoulement de référence et l'écoulement contrôlé par les VGs C2. Comme signalé sur la Fig. 18, les mesures dans le plan « on VG » entre X = 330mm et 335mm sont perturbées par la présence de capteurs Kulite. La taille du choc en lambda est modifiée sous l'action des VGs. Si la position du choc quasi-normal reste stable, à X = 360mm pour Y = 50mm, celle de la branche amont du lambda se décale de 10mm vers l'aval, X = 320mm à 330mm. Le niveau de fluctuations est fortement diminué dans le plan « on VG » du sillage de la paire de VGs, dû à la suppression de la zone décollée. Dans le plan « between VG » entre deux paires de VGs, le maximum de $-\overline{u'v'}$ est similaire à celui de l'écoulement de référence, mais est localisé légèrement plus en amont dans la couche de cisaillement. De plus, en aval du recollement, on note la présence d'un « patch » de valeurs de $-\overline{u'v'}$ de signe opposé, dénotant l'existence d'un sillage induit par l'orientation plus verticale de la couche de cisaillement.

En conclusion, les VGs mécaniques ont un effet bénéfique sur l'écoulement de référence en agissant sur le décollement massif de la couche limite. Les VGs « contra-rotatifs » permettent de le supprimer partiellement car des cellules de fluide décollé de petites dimensions subsistent dans l'interaction. Les actionneurs doivent être localisés suffisamment en amont de l'interaction afin que les tourbillons aient pu transférer de la quantité de mouvement dans la couche limite avant le pied de choc. D'autre part, les perturbations induites par leur présence à la paroi (ondes de détente et de compression) dans l'écoulement restent modérées, et peuvent être minimisées en les dimensionnant à la hauteur de la ligne sonique de la couche limite en amont de l'interaction.

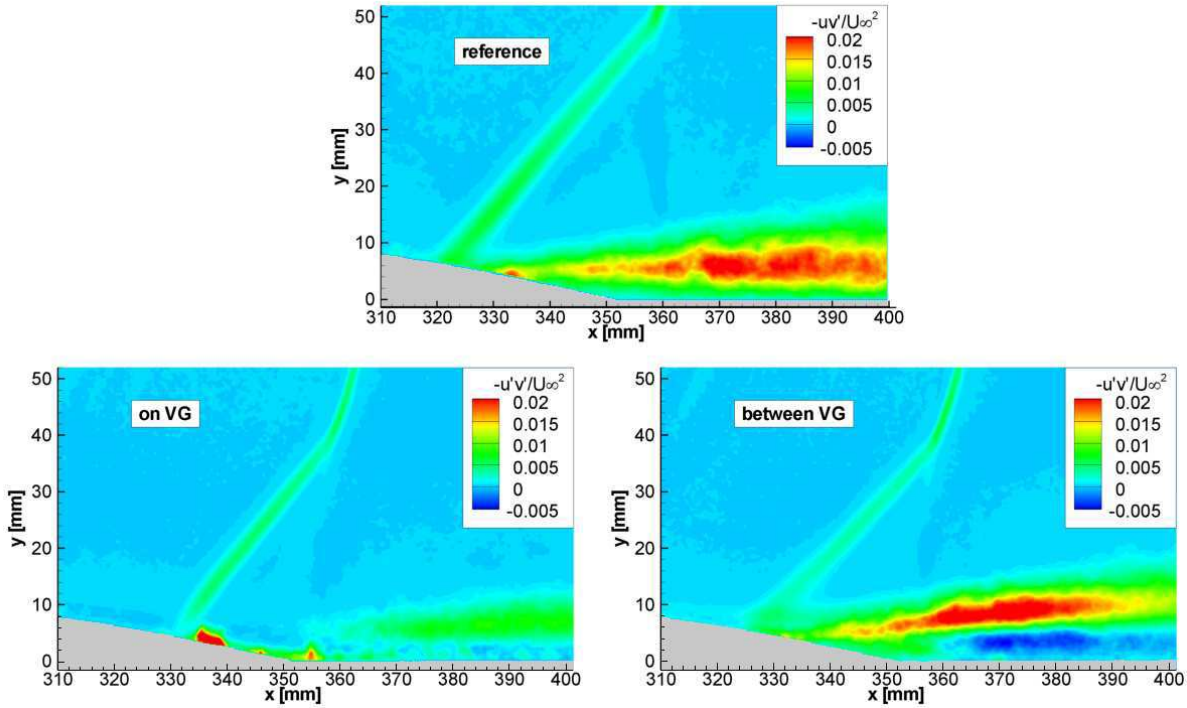

Figure 20 - Iso-contours de la tension de cisaillement $-\overline{u'v'}$ normalisée de l'interaction onde de choc / couche limite sans contrôle (haut) et avec contrôle par les VGs « contra-rotatifs » C2 (bas)

En ce qui concerne maintenant l'étude de la configuration d'oscillation forcée du choc à 30Hz, une comparaison est réalisée sur l'évolution des fluctuations de pression de l'écoulement sans et avec contrôle. Les valeurs RMS de pression sont tracées sur la Figure 21 pour le cas de référence et les six cas avec contrôle par les VGs mécaniques (voir Fig. 13), ainsi que les spectres associés sur la Figure 22, uniquement ceux des trois capteurs localisés dans la région d'oscillation du choc et pour l'écoulement contrôlé par les VGs « contra-rotatifs » C2. Au niveau du capteur G9, le contrôle par VGs permet de maintenir une valeur RMS de la pression du même ordre que celle dans la région supersonique en amont de l'interaction, mesurée environ à 500Pa par le capteur P1, alors qu'elle est fortement amplifiée dans l'écoulement de référence. Ceci signifie que la position la plus amont du choc de tête lors du cycle d'oscillation se décale vers l'aval, et ainsi, que l'amplitude de l'oscillation du choc est réduite sous l'action des VGs. Le spectre correspondant au cas des VGs C2 (voir Fig. 22a) a un niveau large bande plus bas (–25dB) comparé à celui de l'écoulement de référence, et similaire à celui de la région supersonique amont (voir Fig. 10a). La présence de raies de faible énergie dans le spectre signifie que le capteur G9 se situe à la limite de la position amont du choc oscillant. Les niveaux RMS de pression très élevés obtenus par le capteur G6 sans et avec contrôle, de l'ordre de 9000Pa, sont dus à la présence de la bulle de recirculation au niveau de la partie finale de la bosse. Ainsi, les deux spectres sont similaires, avec un pic de fréquence fondamentale à 30Hz et de nombreuses harmoniques avec des niveaux d'énergie comparables (voir Fig. 22b). Pour le capteur G3, des écarts de valeurs RMS sont à noter entre les différents VGs mécaniques car le capteur est situé plus ou moins au point de recollement selon les configurations testées. Néanmoins, ce capteur étant toujours situé en aval du choc de tête, les spectres de l'écoulement de référence et du cas contrôlé par les VGs C2 sont pratiquement équivalents (voir Fig. 22c). Le niveau RMS résiduel mesuré par le capteur P2, de l'ordre de 2500Pa (à comparer au niveau de 500Pa en amont de l'interaction), signifie que la couche limite, même rattachée, n'a pas encore atteint un nouvel état d'équilibre.

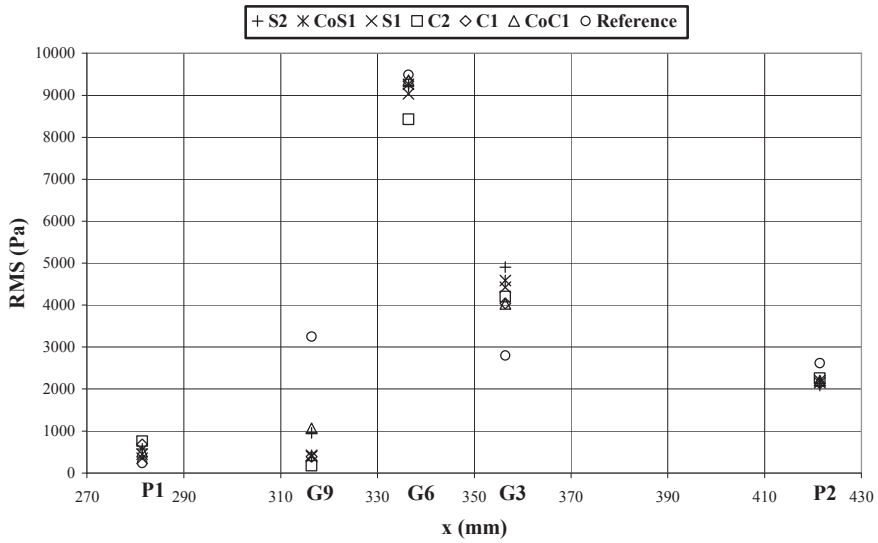

Figure 21 - Valeurs RMS des pressions pour la configuration d'oscillation forcée du choc à 30Hz sans contrôle et avec contrôle par les VGs mécaniques

(a) G9 : X=316,4mm

(b) G6 : X=336,4mm

(c) G3 : X=356,4mm

Figure 22 - Evolution longitudinale des spectres de fluctuations de pression pour la configuration d'oscillation forcée du choc à 30Hz sans contrôle (gauche) et avec contrôle par les VGs « contra-rotatifs » C2 (droite)

La Figure 23 montre les deux positions les plus extrêmes de l'onde de choc dans le canal, à la fréquence d'oscillation de 30Hz, lorsque le contrôle actif est appliqué (voir Fig. 15). Le débit d'aspiration à travers la grille perforée est mesuré à l'aide d'un col sonique placé dans la canalisation reliée à la cavité, dont plusieurs diamètres ont été testés, à savoir : 10, 15, 20 et 30mm. Les visualisations strioscopiques de la Figure 23 sont obtenues pour le col sonique de diamètre 20mm, ce qui correspond à un débit d'aspiration normalisé de Q/Q_0=1% (voir le Tableau 2). La structure de choc est modifiée par le contrôle actif, notamment dans la position la plus amont où le choc en lambda ainsi que le décollement de la couche limite ont pratiquement disparus. En conséquence, l'amplitude d'oscillation du choc est réduite de manière significative en comparaison de l'écoulement de référence (voir Fig. 9). On observe la présence d'ondes obliques de faible intensité en amont du choc, qui prennent naissance à la fois au raccord entre la paroi et la grille perforée et au niveau des trous de la grille.

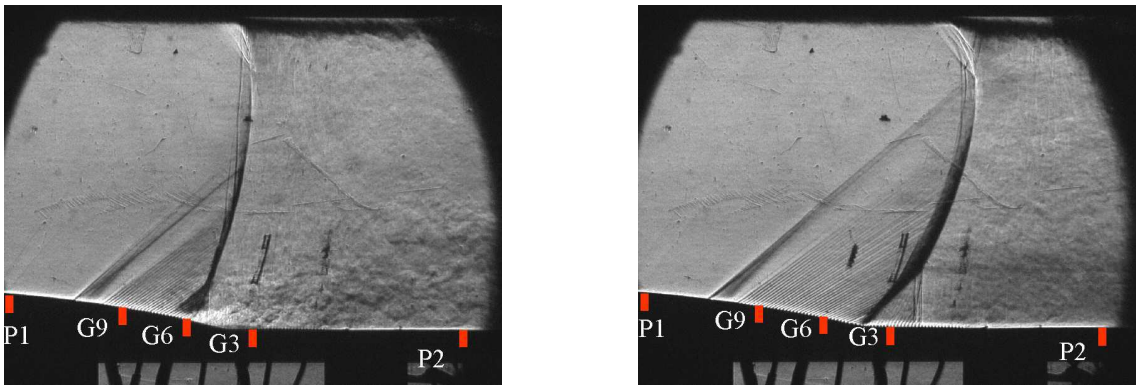

(a) position amont (b) position aval

Figure 23 - Positions de l'onde de choc dans le canal pour la fréquence d'oscillation de 30Hz en présence de contrôle actif : Q/Q_0=1%

La Figure 24 montre l'effet du contrôle actif (dans le cas où Q/Q_0=1%) sur l'évolution longitudinale des spectres de fluctuations de pression des trois capteurs localisés sur la grille perforée, pour la fréquence d'oscillation du choc de 30Hz. Le spectre du capteur G9 a un faible niveau large bande comparé à celui de l'écoulement de référence, avec seulement deux pics, car le capteur est situé dans la région supersonique lorsque l'aspiration agit. Les spectres des capteurs G6 et G3 ont la fondamentale à 30Hz ainsi que de nombreuses harmoniques car les deux capteurs voient passer l'onde de choc durant le cycle d'oscillation. Alors que les spectres de référence et du cas contrôlé en G6 sont similaires, les spectres en G3 diffèrent car le contrôle par aspiration réduit significativement l'amplitude d'oscillation du choc.

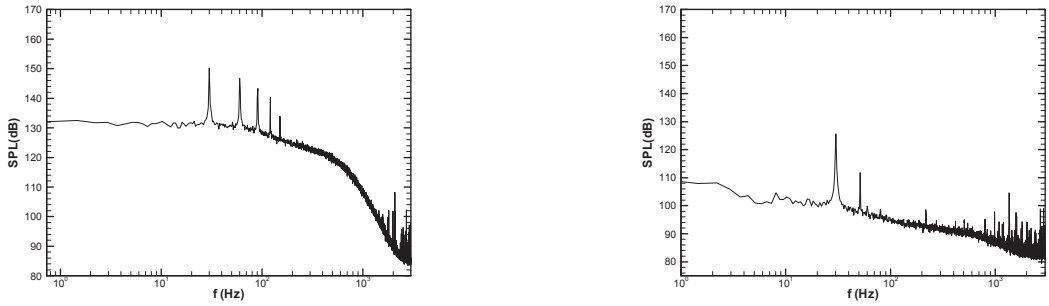

(a) G9 : X=316,4mm

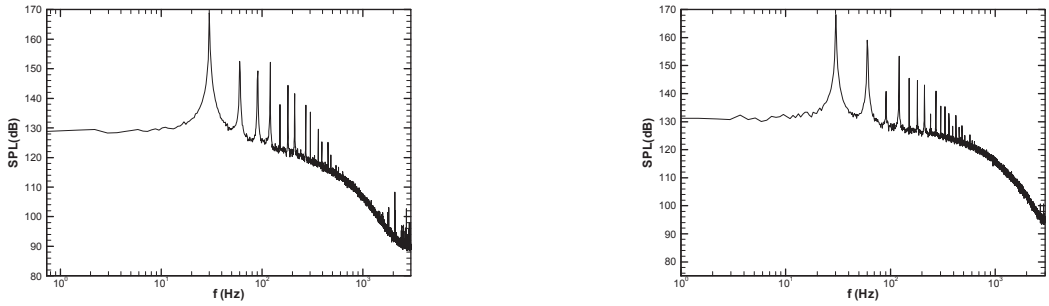

(b) G6 : X=336,4mm

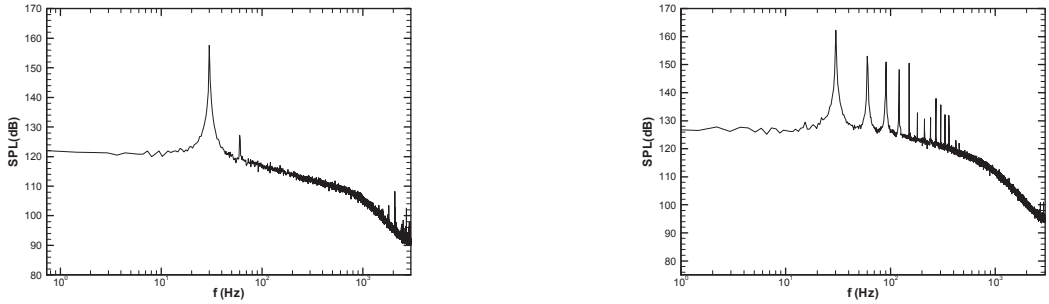

(c) G3 : X=356,4mm

Figure 24 - Evolution longitudinale des spectres de fluctuations de pression pour la configuration d'oscillation forcée du choc à 30Hz sans contrôle (gauche) et avec contrôle actif : Q/Q_0=1% (droite)

Le Tableau 2 donne une comparaison des valeurs d'amplitude de l'oscillation du choc entre l'écoulement de référence et les cas de contrôle actif et passif, c'est-à-dire lorsque le débit d'aspiration à travers la grille perforée est nul. Alors que le contrôle passif par recirculation naturelle de fluide n'a aucun effet sur le battement du choc, le contrôle actif par aspiration réduit l'oscillation du choc. Ainsi, pour une valeur modérée du débit d'aspiration égale à 20,3g/s, ce qui correspond à 1% du débit total du canal transsonique (Q_0=2,3×10^{3}g/s), la diminution de l'amplitude d'oscillation du choc est d'environ 20% (de 30mm à 23,6mm).

Diamètre du col sonique $\varnothing$ (mm)		Débit d'aspiration		Amplitude de l'oscillation ΔX (mm)
		Q (g/s)	Q/Q_0 (%)	
Ecoulement de référence				30
Contrôle passif				30
Contrôle actif par aspiration	10	7,8	0,4	27
	15	14,3	0,6	25
	20	20,3	1	23,6
	30	non amorcé		23,6

Tableau 2 - Evolution de l'amplitude d'oscillation du choc en présence de contrôle par cavité

En conclusion, le contrôle passif par des VGs mécaniques réduit faiblement l'amplitude de l'oscillation forcée du choc en contrariant le déplacement vers l'amont de la branche de tête du choc en lambda. En revanche, le contrôle actif par aspiration de fluide à travers une grille perforée, localisée dans la région d'interaction et avec des débits d'aspiration modérés, est efficace pour réduire l'amplitude de battement du choc.

4. DYNAMIQUE DE L'INTERACTION

4.1. Approche expérimentale

La dynamique de l'interaction onde de choc / couche limite turbulente avec décollement est étudiée par l'analyse à la fois de signaux de pression temporels et de traitement d'images obtenues à haute cadence.

Des capteurs de pression sont placés à la paroi dans la région d'interaction, plus précisément au pied de la branche amont du choc en lambda et dans la zone décollée (capteurs Kulite G9 et G6, voir Fig. 2), mais également au point de recollement de l'écoulement (3 capteurs en X = 390mm, 395mm et 400mm, voir Fig. 25). Les signaux de pression sont amplifiés et échantillonnés à la fréquence de 100kHz, et l'analyse de Fourier utilise la fonction type « fenêtre de Hanning » avec un recouvrement de 50%, donnant des spectres à partir de 500 blocs de 32 768 échantillons chacun. Cela conduit pour chaque spectre à une fréquence de résolution de 3Hz. Comme les instationnarités de l'écoulement ont de faible niveau d'énergie, le choix élevé de 500 blocs est nécessaire pour assurer une bonne convergence et résolution des spectres.

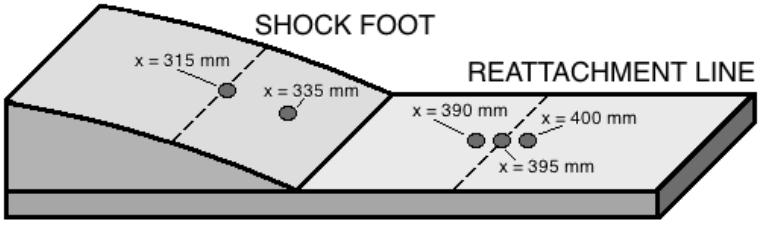

Figure 25 - Schéma d'implantation des capteurs Kulite dans la région d'interaction

La Figure 26 montre les spectres obtenus à partir des mesures de pression instationnaires. Ces spectres étant large bande et ne comportant aucun pic, il est intéressant de les représenter comme le produit de la densité spectrale de puissance par la fréquence (en fonction log) : les spectres sont dits prémultipliés. Le principal résultat est que les mouvements du choc sont caractérisés par des oscillations à basse fréquence, de l'ordre de 300Hz (capteur G9, courbe bleue), tandis que les oscillations à moyenne fréquence, de l'ordre de 4kHz, sont typiques de la région de recollement et de la zone de cisaillement (courbes rouge, rose et noir). Les valeurs du nombre de Strouhal, calculées avec une échelle de longueur caractéristique de la région décollée de l'écoulement, sont égales à 0,04 et 0,5, respectivement. De plus, la densité spectrale de puissance au niveau du décollement (capteur G9, courbe bleue) indique que le choc bat à basse fréquence uniquement, et ainsi se comporte comme un filtre passe-bas avec une fréquence de coupure voisine de 300Hz. Le choc amortit toutes les fluctuations de pression à plus hautes fréquences provenant de la région décollée.

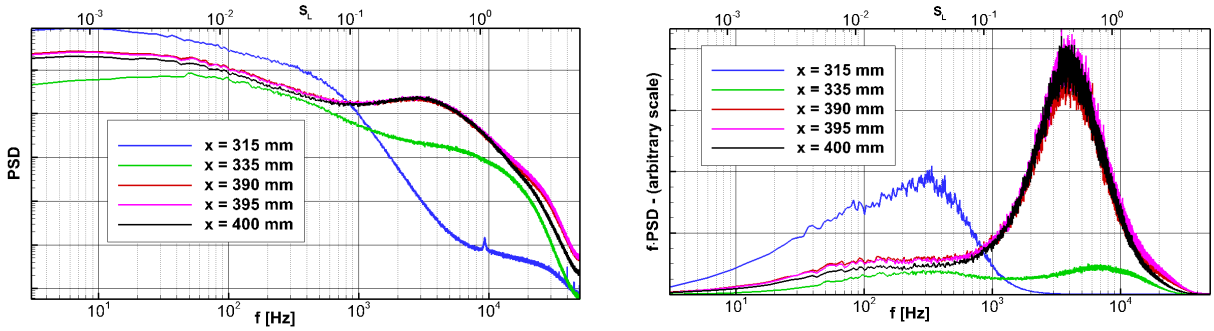

(a) densité spectrale de puissance (b) spectre prémultiplié

Figure 26 - Spectres de pression à la paroi dans la région d'interaction

Afin d'accéder à une information plus globale de la distribution spatiale des instationnarités dans l'interaction, l'écoulement a été analysé à l'aide d'images de strioscopie acquises avec une caméra haute cadence. Cette technique de mesure donne accès aux gradients de densité (horizontaux ou verticaux selon l'orientation du couteau) lesquels permettent de caractériser l'onde de choc et les structures tourbillonnaires présentes dans la couche de mélange. A partir des échantillons (60 000 images acquises à une cadence de 35kHz), un traitement des images par une décomposition en modes de Fourier met en exergue la forme spatiale des modes qui représentent des instationnarités typiques à certaines fréquences.

La Figure 27 montre les modes de Fourier obtenus à partir des gradients verticaux de densité pour des fréquences caractéristiques du battement de choc (f = 300Hz) et des instationnarités de la couche de mélange (f = 4000Hz). Les oscillations à basse fréquence sont typiques de l'intégralité de l'onde de choc ainsi que de la partie centrale de la couche de mélange, qui suit les mouvements du choc. Sur un mode de Fourier à plus haute fréquence, la plupart de l'énergie est concentrée dans la zone de cisaillement et le mode n'est plus présent sur le choc.

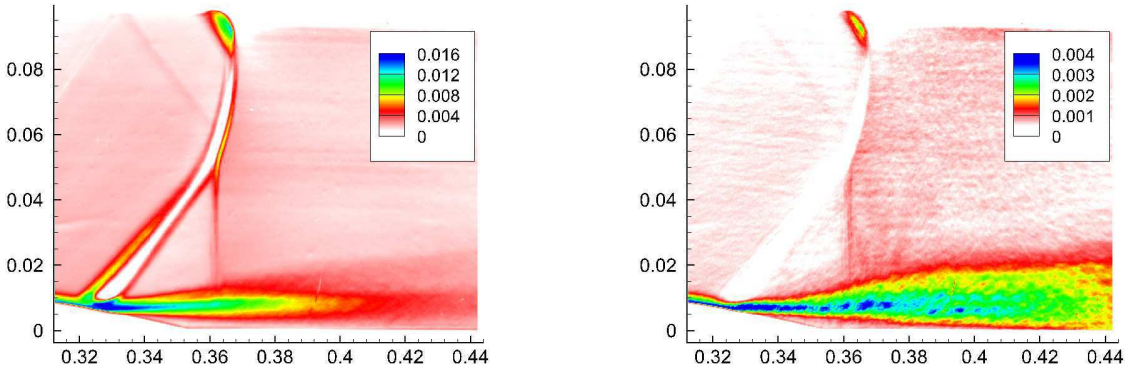

(a) mode à 300Hz (b) mode à 4000Hz

Figure 27 - Modes de Fourier pour le gradient vertical de densité

4.2. Approche numérique

L'analyse de stabilité linéaire est utilisée pour avoir des informations sur le comportement des instationnarités dans un écoulement. Elles peuvent être classifiées en deux catégories : l'écoulement peut se comporter comme un oscillateur, et imposer sa propre dynamique, ou il peut avoir un comportement de type amplificateur de bruit. Dans le premier

cas, une décomposition en modes globaux peut décrire la dynamique de l'écoulement qui est piloté par un mode global instable. Dans le second cas, le système filtre et amplifie certains bruits de fond du système à cause des instabilités convectives, et une décomposition en valeurs propres de l'opérateur de Navier-Stokes linearisé ne peut pas décrire la dynamique du système. Dans cette étude, la dynamique de l'interaction est analysée à travers une décomposition en valeurs singulières du Résolvant Global, en étudiant la réponse de l'écoulement à des forçages externes. Cette approche a été appliquée avec succès pour décrire les modes les plus amplifiés dans des écoulements incompressibles.

L'hypothèse sur laquelle l'étude numérique s'appuie est que les deux phénomènes instationnaires observés expérimentalement sont caractérisés par des fréquences inférieures aux fréquences typiques des structures qui caractérisent les effets de la turbulence. Cette hypothèse de séparation d'échelle de fréquence permet de modéliser l'impact des petites structures sur les plus larges à travers une viscosité turbulente μ_t. Des calculs de type RANS avec un modèle de Spalart-Allmaras ont permis de simuler l'écoulement dans un domaine qui reproduit l'intégralité de la veine d'essais utilisée pour l'étude expérimentale. Le résultat, présenté en Figure 28, est en accord avec les mesures PIV (voir Fig. 5) mais indique que l'écoulement est stationnaire. L'intégration en temps des équations n'est pas capable de reproduire les mouvements à basse fréquence de battement du choc ainsi que les fluctuations observées expérimentalement dans la zone cisaillée.

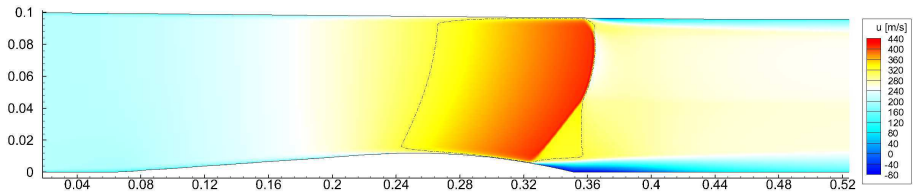

Figure 28 - Calcul RANS de la composante longitudinale de la vitesse. Ligne sonique en pointillée

Le résultat de la simulation RANS est ensuite considéré comme champ de base pour une analyse de stabilité : grâce à une linéarisation des équations, on obtient la matrice Jacobienne et un problème aux valeurs propres associé. Si au moins une des valeurs propres présente un taux d'amplification positif, alors l'écoulement est instable. Or les spectres obtenus montrent que les valeurs propres sont complètement stables, donc que les instationnarités de l'écoulement ne peuvent pas être liées à un mode global instable (voir Annexe D).

Vu l'absence de modes globaux instables, la dynamique de l'interaction est de type amplificateur de bruit. Pour décrire le mécanisme de sélection de fréquences, on introduit le Résolvant Global défini par :

$$\mathfrak{R} = (i\omega \mathrm{I} - \mathrm{J})^{-1}$$

où J est la matrice Jacobienne et I est la matrice identité.

Le Résolvant Global existe pour chaque fréquence ω car toutes les valeurs propres de J sont à partie réelle négative, et il met en relation la réponse de l'écoulement $\hat{w}$ quand il est soumis à un forçage externe $\hat{f}$ à travers : $\hat{w} = \mathfrak{R}\ \hat{f}$. Grâce à une décomposition en valeurs singulières de la matrice $\mathfrak{R}$, on peut calculer le forçage (dit optimal), à une certaine fréquence, qui produit la réponse la plus énergétique de l'écoulement. En faisant cette opération pour

toutes les fréquences ω, on obtient la courbe de gain $G(\omega)$ qui représente le ratio entre l'énergie de la réponse obtenue par un forçage optimal et le forçage lui-même.

L'évolution en fréquence de la courbe de gain, donnée par la valeur propre la plus énergétique λ_1 du Résolvant Global, est portée sur la Figure 29. Cette courbe indique que l'interaction est très sensible aux basses fréquences, caractéristiques du battement du choc, et aux moyennes fréquences, caractéristiques des fluctuations de la couche de mélange.

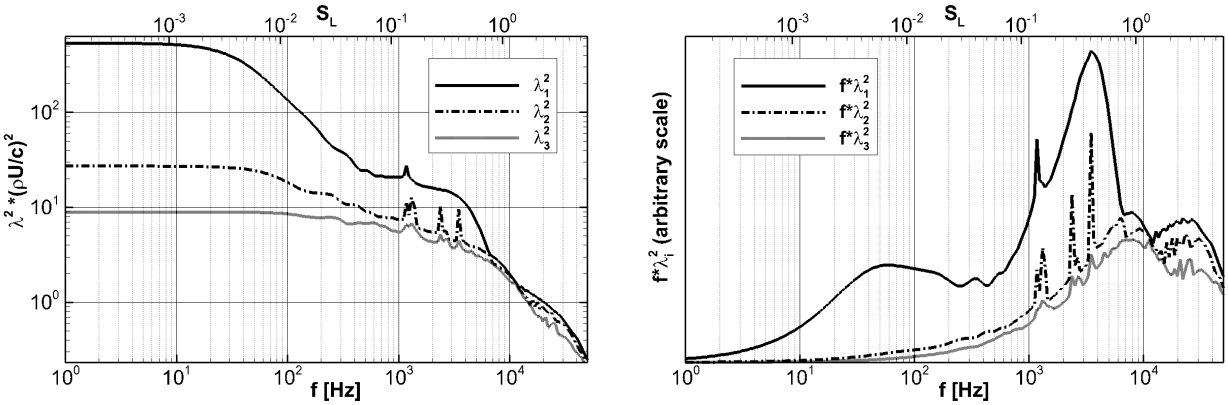

(a) fonction de gain (échelle logarithmique) (b) gain prémultiplié

Figure 29 - Valeurs propres du Résolvant Global. Chaque λ_i représente le gain quand l'écoulement est forcé, à la fréquence f, avec un forçage optimal

En gain prémultiplié, on peut observer que les réponses les plus énergétiques pour un forçage optimal à basse et moyenne fréquences sont obtenues pour f = 50Hz et 4000Hz, respectivement. Ces réponses optimales sont représentées sur la Figure 30 pour la partie réelle de la densité de l'écoulement. A la fréquence f = 50Hz, la réponse est concentrée uniquement sur le choc, et indique qu'un forçage à basse fréquence est capable d'activer une réponse de l'écoulement qui est sur le choc. A la fréquence f = 4000Hz, la réponse n'est pas dans le choc comme dans le cas à basse fréquence, mais plutôt concentrée dans la zone cisaillée, avec des structures circulaires périodiques qui commencent à partir du point de décollement. Ces mouvements à moyennes fréquences de l'interaction sont dus à des instabilités de type Kelvin-Helmholtz dans la couche de cisaillement. D'autre part, on peut observer des similarités entre ces réponses optimales et les modes de Fourier obtenus expérimentalement à partir des images de strioscopie, représentés en Figure 27.

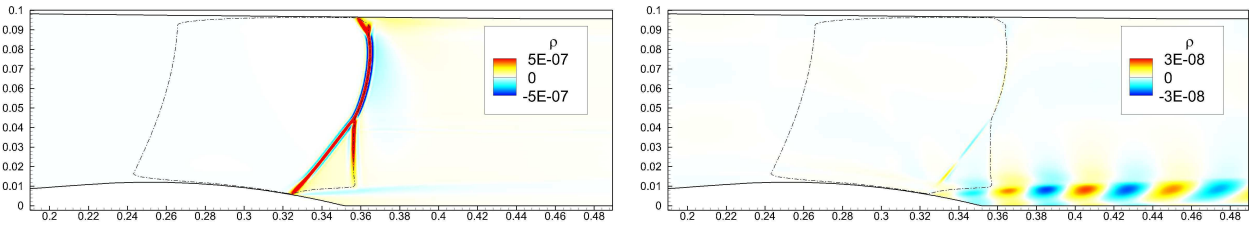

(a) fréquence à 50Hz (b) fréquence à 4000Hz

Figure 30 - Réponses optimales pour la partie réelle de la densité

En conclusion, des mesures ont permis de montrer que l'interaction est caractérisée par la coexistence de deux fréquences caractéristiques distinctes : le battement de l'onde de choc impliquant généralement une oscillation à basse fréquence (dont l'origine est controversée) et la couche de mélange se développant après le décollement et battant à des fréquences qui sont plus élevées que celle du mouvement de choc et associées à des

instabilités de type Kelvin-Helmholtz. Une étude de stabilité globale par décomposition en valeurs propres de l'opérateur de Navier-Stokes linéarisé autour d'un champ de base RANS indique que l'interaction est un phénomène stable, et la dynamique de l'écoulement ne peut pas être décrite par un mode global instable. Une approche linéarisée est proposée dans laquelle la réceptivité de l'écoulement à un forçage externe est analysée à travers une décomposition en valeurs singulières du Résolvant Global. Cette approche permet d'expliquer la sélection de fréquence dans cet écoulement, et montre que l'interaction filtre et amplifie le bruit résiduel existant : certaines perturbations sont plus amplifiées dans la couche de mélange, tandis que le choc semble se comporter comme un filtre passe-bas.

5. PERSPECTIVES

Les activités liées à la thématique *Contrôle des écoulements* offrent des perspectives de recherche intéressantes, si l'on en juge par le nombre et la qualité des publications de la communauté scientifique sur le sujet. De plus, les objectifs portés par cet axe de recherche visent notamment à un transfert de technologie vers les industries aéronautique et automobile, permettant un gain de rendement et des améliorations de performance à la fois pour les aéronefs et les véhicules terrestres.

Dans ce contexte, mes perspectives de recherche vont continuer à porter sur *le contrôle et la dynamique des interactions onde de choc / couche limite*. Les écoulements étudiés couvrent plus spécifiquement les régimes transsoniques et supersoniques que l'on rencontre sur les avions civils, les avions militaires et les missiles. Les applications liées à ces études touchent aussi bien l'aérodynamique externe (optimisation des performances d'une voilure) que l'aérodynamique interne (efficacité d'une entrée d'air). Ainsi, un contrôle efficace des interactions onde de choc / couche limite passe par une compréhension fine des phénomènes physiques présents dans la région d'interaction, à savoir : l'amplification du niveau turbulent au passage du choc, les propriétés de la région de décollement (échelles spatio-temporelles, caractère tridimensionnel), la réponse de l'onde de choc aux perturbations provenant du décollement et des ondes acoustiques, la formation de grosses structures tourbillonnaires dans la couche de cisaillement et le retour à une couche limite à l'équilibre en aval du recollement.

Les dispositifs de contrôle à mettre en œuvre doivent permettre d'augmenter l'efficacité aérodynamique d'un système, par exemple en réduisant la traînée d'une voilure d'avion ou en augmentant le rendement d'une prise d'air d'un avion de combat ou d'un missile. Ainsi, le contrôle de cette classe d'écoulements compressibles nécessite le développement d'actionneurs performants, tels que : des micro-jets fluidiques continus ou pulsés, des jets synthétiques, des actionneurs plasma (DBD, JSP, micro-ondes…), des actionneurs piézo-électriques et magnétostrictifs, MEMS.

Le développement de ces activités passe par l'élaboration de sujets de thèse et l'encadrement de jeunes chercheurs (doctorants, post-docs). Ces sujets de thèse se feront à la fois dans le cadre de projets internes à l'ONERA et de travaux collaboratifs avec des laboratoires universitaires et du CNRS d'Orléans. En effet, la thématique de contrôle des écoulements fait partie des axes de recherche des laboratoires PRISME, particulièrement dans l'axe *Ecoulements et Systèmes Aérodynamiques* (ESA), et ICARE à travers la plateforme expérimentale *FAST*. Les moyens expérimentaux de l'ONERA à grand nombre de Mach et

haute pression viendront compléter à la fois ceux de PRISME en faible subsonique et ceux d'ICARE en hypersonique basse pression.

Mon projet de recherche se décline suivant plusieurs axes dépendant de la technique de contrôle (actionneurs) utilisée pour agir sur la topologie de l'écoulement, et plus particulièrement sur la région de décollement du fluide. On peut distinguer :

1. des actionneurs fluidiques à jets continus, de type générateurs de tourbillons ;

2. des actionneurs fluidiques pulsés répondant à la dynamique de l'écoulement ;

3. un actionneur plasma jouant sur la structure de l'onde de choc.

Ces trois axes de recherche sont déclinés et décrits ci-dessous.

Concernant le premier type d'actionneurs, un doctorant a été recruté fin 2016 avec un cofinancement de la DGA et un soutien de Dassault Aviation. Le sujet de la thèse, *« Optimisation du contrôle de décollement en écoulement transsonique de canal »*, a pour objectif de contrôler par une méthode d'optimisation l'interaction avec décollement à l'aide d'actionneurs fonctionnant avec un coût énergétique le plus faible possible. Un second sujet faisant partie du projet *« Shock Waves and Flow Control in Innovative Aeronautical Applications »* a été soumis dans le cadre des actions Marie Curie « Innovative Training Networks » du programme de l'Union Européenne pour la recherche et l'innovation *Horizon 2020*. L'objectif visé est de contrôler les écoulements de coin dans une interaction avec décollement produite dans un canal transsonique. Les principaux partenaires associés à ce projet sont : IUSTI, IMFT, Université de Cambridge, Université de Rome La Sapienza, TU Berlin, TU Delft et IMP/PAN (Pologne). Le résultat de l'appel d'offre sera connu en juin 2017.

L'étude du deuxième type d'actionneur, l'actionneur pulsé, fera l'objet d'un projet de recherche mené en collaboration entre l'ONERA et PRISME. Ce projet portera sur la dynamique de l'interaction entre une onde de choc et une couche limite turbulente décollée dans un écoulement transsonique. L'analyse pourra être étendue aux problématiques plus applicatives que sont le régime de pompage dans une entrée d'air supersonique et le phénomène de tremblement d'une voilure d'avion (suite du projet de recherche fédérateur PRF *BUFET'N CO* de l'ONERA, pour lequel Azeddine Kourta faisait partie du comité scientifique de pilotage). PRISME a déjà travaillé sur ces problématiques dans le cadre de l'ANR *SPICEX* et a bénéficié de données expérimentales de l'ONERA pour valider des modèles de turbulence à équations de transport. Un objectif à plus long terme sera le développement d'actionneurs performants et de stratégie du contrôle. Dans ce contexte, l'identification de certains modes fréquentiels des instationnarités présentes dans ce type d'écoulement va permettre d'optimiser les dispositifs de contrôle testés dans un premier temps en boucle ouverte, mais également d'orienter dans le choix des capteurs à utiliser pour des scénarios de contrôle en boucle fermée. Ainsi, la collaboration avec PRISME, qui existe déjà dans le cadre du GDR *Contrôle des décollements*, sera renforcée par l'intégration des axes de recherche pour le contrôle des écoulements compressibles avec présence d'ondes de choc. Dans le cadre de cette action collaborative, il est prévu de faire une demande de cofinancement de thèse par la DGA et le doctorant recruté sera inscrit à l'Université d'Orléans.

L'étude du troisième type d'actionneur, l'actionneur plasma, fera l'objet d'un projet de recherche dans lequel l'ONERA et ICARE seront impliqués. Le projet est orienté sur le contrôle d'écoulements supersonique et hypersonique à basse enthalpie, et plus particulièrement sur le contrôle des ondes de choc par dépôt d'énergie généré par plasma. Le but est de répondre à deux problématiques touchant les phases de vol super et hypersonique, à savoir : le contrôle de trajectoire et la manipulation des ondes de choc afin de réduire la traînée d'onde de l'écoulement. L'étude expérimentale sera menée sur deux installations différentes et complémentaires : la soufflerie supersonique/hypersonique raréfiée MARHY du laboratoire ICARE et la soufflerie transsonique/supersonique S8Ch de l'ONERA. L'intérêt de ce projet prend appui sur la complémentarité des domaines de fonctionnement des deux moyens d'essais impliqués, permettant d'étudier l'efficacité de l'actionneur à la fois en régime raréfié simulant le vol des engins à haute altitude et en régime transsonique correspondant à des altitudes plus basses. Les différents régimes de pression reproduits en soufflerie influant sur l'interaction du couplage écoulement / plasma, la compréhension de ce phénomène est capitale pour la mise en œuvre et l'amélioration de ce type d'actionneurs. Ce projet devrait prendre forme par la soumission d'une ANR (a priori ASTRID) coordonnée par Viviana Lago.

6. CURRICULUM VITAE

BUR Reynald
14, rue Jean Jaurès
91430 Igny
01 46 23 51 98 (Pro) / 06 31 98 36 46 (Perso)

Né le 1 Novembre 1962
Nationalité française
Marié, 2 enfants

Docteur en mécanique
Ingénieur spécialiste et maître de recherche 1 à l'ONERA

Formation

1991 Doctorat de Mécanique de l'Université Paris VI - Mention Très Honorable
ONERA / Division Aérodynamique Fondamentale
1987 DEA Conversion de l'Energie de l'Université Paris VI - Mention Bien
1985 Diplôme d'ingénieur ESTACA - Option Aéronautique et Espace

Activités professionnelles

Domaine d'activités

Ingénieur au sein du Département d'Aérodynamique Fondamentale et Expérimentale (DAFE) de la Branche Mécanique des Fluides et Energétique, mes activités d'étude et de recherche s'exercent dans le domaine de l'expérimentation, de la modélisation et du contrôle des phénomènes d'interaction entre les ondes de choc et les couches limites en présence de décollement. Mes travaux sont actuellement soldés par dix-sept publications dans des revues à comité de lecture.

Depuis 2003, je suis responsable de l'unité des souffleries de recherche du Département DAFE. Cette unité comporte à ce jour seize personnes en charge d'une dizaine de souffleries allant du bas subsonique à l'hypersonique froid.

Enseignements

De 2003 à 2009 : chargé de cours et de TD en 4ème et 5ème année de l'EPF (23 heures par an).

Depuis 2012 : chargé de Modex en Aérodynamique en 2ème année de l'ENSTA (20 heures par an).

Depuis 2012 : chargé de cours et de TD en Aérodynamique dans le Master 2 Dynamique des Fluides et Energétique de l'Université Paris Sud (30 heures par an).

7. LISTE DES PUBLICATIONS

Thèse

Bur, R., «Etude fondamentale sur le contrôle passif de l'interaction onde de choc / couche limite turbulente en écoulement transsonique», Thèse de Doctorat de l'Université Paris VI, 15 mars 1991 (et ONERA Note Technique 1991-9 ; Traduction anglaise ESA TT 1278).

Publication d'un ouvrage

Délery, J., et Bur, R., «Traité d'aérodynamique compressible - Volume 4 : exercices d'application avec corrigés», HERMES Science Publications, ISBN : 978-2-7462-2584-8, 432 pages, 2010.

Publications soumises à évaluation par un comité de lecture

Bur, R., «Passive Control of a Shock Wave / Turbulent Boundary Layer Interaction in a Transonic Flow», *Aerospace Research*, No. 1992-6, Nov.-Dec. 1992, pp. 11-30.

Bur, R., Délery, J., et Corbel, B., «Basic Study of Passive Control Applied to a Two-Dimensional Transonic Interaction», Notes on Numerical Fluid Mechanics, Vol. 56 (Euroshock-Drag Reduction by Passive Shock Control), Stanewsky, E., Délery, J., Fulker, J., Geissler, W. (Eds.), Vieweg, Wiesbaden (Germany), 1997, pp. 89-111.

Bur, R., Délery, J., Corbel, B., Soulevant, D., et Soares Morgadinho, R., «A Basic Experimental Investigation of Passive Control Applied to a Transonic Interaction», *Aerospace Science and Technology*, Vol. 2, No. 1, Jan. 1998, pp. 61-73.

Bur, R., Corbel, B., et Délery, J., «Study of Passive Control in a Transonic Shock Wave / Boundary Layer Interaction», *AIAA Journal*, Vol. 36, No. 3, Mar. 1998, pp. 394-400.

Benay, R., Berthouze, P., et Bur, R., «Modeling of Controlled Shock-Wave / Boundary-Layer Interactions in Transonic Channel Flow», *AIAA Journal*, Vol. 39, No. 12, Dec. 2001, pp. 2293-2301.

Bur, R., Benay, R., Corbel, B., et Délery, J., «Study of Control Devices Applied to a Transonic Shock Wave / Boundary Layer Interaction», Notes on Numerical Fluid Mechanics and Multidisciplinary Design, Vol. 80 (Euroshock II-Drag Reduction by Shock and Boundary Layer Control), Stanewsky, E., Délery, J., Fulker, J., De Matteis, P. (Eds.), Springer, Berlin (Germany), 2002, pp. 133-152.

Bur, R., et Berthouze, P., «Forced Oscillation of a Shock-Wave in a Transonic Channel Flow», Proceedings of the IUTAM Symposium Transsonicum IV, Göttingen (Germany), Sept. 2-6, 2002, Vol. 73, Sobieczky, H. (Ed.), Kluwer Academic Publishers, 2003, pp. 47-52.

Galli, A., Corbel, B., et Bur, R., «Control of Forced Shock-Wave Oscillations and Separated Boundary Layer Interaction», *Aerospace Science and Technology*, Vol. 9, No. 8, Nov. 2005, pp. 653-660.

Bur, R., Benay, R., Galli, A., et Berthouze, P., «Experimental and Numerical Study of Forced Shock-Wave Oscillations in a Transonic Channel», *Aerospace Science and Technology*, Vol. 10, No. 4, May 2006, pp. 265-278.

Bur, R., et Chanetz, B., «Experimental study on the PRE-X vehicle focusing on the transitional shock-wave / boundary-layer interactions», *Aerospace Science and Technology*, Vol. 13, No. 7, Oct.-Nov. 2009, pp. 393-401, DOI 10.1016/j.ast.2009.09.002.

Bur, R., Coponet, D., et Carpels, Y., «Separation control by vortex generator devices in a transonic channel flow», *Shock Waves Journal*, Vol. 19, No. 6, Dec. 2009, pp. 521-530, DOI 10.1007/s00193-009-0234-6.

Bur, R., «Nozzle Forced Shock Oscillations with Wall Bump», Notes on Numerical Fluid Mechanics, Vol. 114 (Unsteady Effects of Shock Wave Induced Separation), Doerffer, P., Hirsch, C., Dussauge, J-P., Babinsky, H., Barakos, G.N. (Eds.), Springer-Verlag, Berlin (Germany), 2010, pp. 135-161.

Sartor, F., Losfeld, G., et Bur, R., «PIV Study on a Shock-Induced Separation in a Transonic Flow», *Experiments in Fluids*, Vol. 53, No. 3, 2012, pp. 815-827, DOI 10.1007/s00348-012-1330-4.

Molton, P., Dandois, J., Lepage, A., Brunet, V., et Bur, R., «Control of Buffet Phenomenon on a Transonic Swept Wing», *AIAA Journal*, Vol. 51, No. 4, April 2013, pp. 761-772, DOI 10.2514/1.J051000.

Molton, P., Hue, D., et Bur, R., «Drag Induced by Flat-Plate Imperfections in Compressible Turbulent Flow Regimes», *Journal of Aircraft*, Vol. 52, No. 2, March-April 2015, pp. 667-679, DOI 10.2514/1.C032911.

Sartor, F., Mettot, C., Bur, R., et Sipp, D., «Unsteadiness in transonic shock-wave / boundary-layer interactions: experimental investigation and global stability analysis», *J. Fluid Mech.*, Vol. 781, 2015, pp. 550-577, DOI 10.1017/jfm.2015.510.

Merienne, M-C., Molton, P., Bur, R., et Le Sant, Y., «Pressure-Sensitive Paint Application to an Oscillating Shock Wave in a Transonic Flow», *AIAA Journal*, Vol. 53, No. 11, Nov. 2015, pp. 3208-3220, DOI 10.2514/1.J053744.

8. ENCADREMENT ET PROGRAMME DE RECHERCHE

Responsabilités d'encadrement

Thèses

Pascal Berthouze (1998 - 2001)
- sujet : Ecoulement transsonique instationnaire de canal
- directeur de thèse : T. Alziary de Roquefort (Université de Poitiers)

Arnaud Galli (2001 - 2005)
- sujet : Contrôle de l'oscillation de choc en écoulement transsonique de canal
- directeur de thèse : J.-P. Dussauge (Université de Provence/Aix Marseille)

Cyril de Champvallins (2005 - 2008)
- sujet : Etude du contrôle du phénomène de pompage dans une entrée d'air supersonique
- directeur de thèse : J.-P. Dussauge (Université de Provence/Aix Marseille)

Fulvio Sartor (2010 - 2014)
- sujet : Unsteadiness in Transonic Shock-Wave / Boundary-Layer Interactions: Experimental Investigation and Global Stability Analysis
- directeur de thèse : J.-P. Dussauge (Université de Provence/Aix Marseille)

Quentin Chanzy (en cours)
- sujet : Optimisation du contrôle de décollement en écoulement transsonique de canal
- directeur de thèse : E. Garnier (ONERA, Université de Paris Saclay)

Rapporteur de thèse

Paul Bruce (Université de Cambridge - 13 février 2009)
- sujet : Transonic Shock / Boundary Layer Interactions Subject to Downstream Pressure Perturbations
- directeur de thèse : H. Babinsky (Université de Cambridge)

Todd Davidson (Université de Cambridge - 29 novembre 2016)
- sujet : Effect of Incoming Boundary Layer State on Flow Development Downstream of Normal Shock Wave / Boundary Layer Interactions
- directeur de thèse : H. Babinsky (Université de Cambridge)

Stages de courte durée (4 à 6 mois)

Encadrement de seize stagiaires : stages de fin d'étude (ENSAé, ENSMA et EPF) et de Master 2 (Ecole Polytechnique, ENS Cachan, Universités Paris 6, Saint-Quentin-en-Yvelines/Versailles et Poitiers)

Encadrements dans le cadre d'échange et de collaboration

Collaboration avec l'Université Aoyama Gakuin, Tokyo, sur des travaux à caractère fondamental en soufflerie de recherche (visite d'un mois du Prof. N. Saida en septembre 1996)

Collaboration, dans le cadre des échanges ONERA/DLR, avec des collègues du DLR-Cologne sur des travaux de simulation numérique d'écoulement hypersonique (visites de trois mois en 1997 et en 1999)

Programme d'échange et de collaboration de chercheurs avec l'Université Technique d'Istanbul, Turquie, dans le cadre des activités du Nato/RTA/AVT Panel, portant sur les interactions onde de choc / tourbillons se développant sur une aile delta (visites croisées d'une semaine en 2001)

Principaux programmes de recherche

Optimisation de la prise d'air du statoréacteur
- programme PREPHA (1993-1998)

Etude de l'aérodynamique des entrées d'air supersoniques
- programme ATSF *Avion de transport supersonique de 2ème génération* (1993-2004)
- PRF *Etudes d'écoulements relatifs à l'avion supersonique* (2000-2004)
- projet dans le cadre d'appels d'offre du Ministère de la Recherche (2001-2005)
- groupe GARTEur AG34 *Aérodynamique des entrées d'air supersoniques* (2001-2006)
- projet européen HISAC *High Speed Aircraft* (2005-2008)

Contrôle des interactions en vue d'améliorer les performances des avions de transport civils
- projets européens EUROSHOCK 1 & 2 (1993-1999)
- responsable ONERA du programme *Contrôle des écoulements* dans le cadre de la coopération DLR-ONERA sur le thème « Avions civils » (2002-2006)

Contrôle des interactions transsoniques en écoulement instationnaire
- projet européen UFAST *Unsteady Effects in Shock Wave induced Separation* (2006-2009)
- PRF BUFET'N CO *BoUcle FErmée appliquée au Tremblement 3D : démonstratioN du COntrôle* (2007-2012)

Etude de la transition laminaire / turbulent sur les interactions onde de choc / couche limite
- projet européen TFAST *Transitional Effects on Shock Wave / Boundary Layer Interaction* (2012-2015)

Réduction de la traînée d'un corps par apport d'énergie au voisinage du point d'arrêt
- projet ANR ASTRID *Perche laser* (en cours)

Nota : PRF = projet de recherche fédérateur interne à l'ONERA

ANNEXE A - CONTROL OF FORCED SHOCK-WAVE OSCILLATIONS AND SEPARATED BOUNDARY LAYER INTERACTION

Galli A., Corbel B. et Bur R.

Aerospace Science and Technology, Vol. 9, No. 8, Nov. 2005, pp. 653-660

Available online at www.sciencedirect.com
SCIENCE DIRECT®
Aerospace Science and Technology 9 (2005) 653–660
Aerospace Science and Technology
www.elsevier.com/locate/aescte

Control of forced shock-wave oscillations and separated boundary layer interaction

Contrôle de l'interaction de l'oscillation forcée d'une onde de choc avec une couche limite décollée

Arnaud Galli, Bernard Corbel, Reynald Bur *

ONERA, Fundamental and Experimental Aerodynamics Department, 8, rue des Vertugadins 92190 Meudon, France

Received 25 May 2005; received in revised form 22 July 2005; accepted 22 July 2005

Available online 24 August 2005

Abstract

The purpose of the present study is to analyze the unsteady aspects of the transonic interaction between an oscillating shock-wave and a separated boundary layer in a channel flow. Oscillation of the shock-wave is forced thanks to a periodic variation of the downstream throat section given by a rotating elliptical shaft located near this throat, in the middle of the channel, inducing pressure perturbations moving upstream. The channel's lower wall is equipped with a contour profile – or a bump – allowing for flow separation. Flow field visualizations during a shock-wave oscillation cycle have been carried out using a continuous light system coupled with a high-speed camera and a spark light system coupled with a drum camera. Continuous and unsteady wall pressure measurements have been conducted. Spectral analysis of the signals has shown that response from sensors is driven by the leading shock oscillation of the λ-shock structure and also has allowed for the phase velocity of the downstream perturbations to be determined. Two-component laser Doppler velocimetry probings have been carried out and phase-averaged fields obtained thanks to a time information given by a marker located on the rotating shaft. The evolution of the separated bubble during a shock-wave oscillation period has been accurately quantified. The impact of control techniques – passive and active by suction – on the boundary layer and on the forced oscillation of the shock-wave has been characterized. The control device is a cavity covered by a perforated plate located in the interaction region. Active control has decreased the shock oscillation amplitude thanks to the suction of the separated boundary layer across the perforated plate.

Résumé

La présente étude a pour objectif d'analyser les aspects instationnaires de l'interaction transsonique entre une onde de choc oscillante et une couche limite décollée en écoulement de canal. L'oscillation de l'onde de choc est forcée par une évolution périodique de la section d'un col aval, au moyen d'une came elliptique en rotation placée au voisinage de ce col, au milieu du canal. La came en rotation génère des ondes de pression qui vont remonter l'écoulement. La paroi inférieure du canal est évolutive – en forme de bosse – afin de permettre un décollement de l'écoulement. Des visualisations de l'écoulement durant une période d'oscillation du choc ont été réalisées à l'aide d'une caméra rapide couplée à une lampe continue et d'une caméra à tambour couplée à un générateur d'éclairs. Des mesures de pressions pariétales continues et instationnaires ont été effectuées. L'analyse spectrale des signaux a montré que la réponse des capteurs est pilotée par l'oscillation de la branche amont du choc en lambda ; elle a permis également de déterminer la vitesse de phase des perturbations aval. Des sondages à l'aide d'un vélocimètre laser bidirectionnel ont été réalisés. Le traitement des mesures est fait par analyse conditionnelle grâce à la synchronisation des acquisitions à un top par tour au niveau de la came tournante. L'évolution du bulbe de décollement pendant le cycle d'oscillation du choc a été quantifiée avec précision. L'impact de techniques de contrôle – passive et active par aspiration – sur la couche limite et sur l'oscillation forcée de l'onde de choc a été caractérisé. Le dispositif de contrôle consiste en une cavité recouverte par une plaque perforée ; il est situé dans la région de l'interaction. Le contrôle actif a permis de diminuer l'amplitude de l'oscillation du choc par aspiration de la couche limite décollée à travers la paroi perforée.

* Corresponding author. Tel.: +33 1 46 23 51 98; fax: +33 1 46 23 51 58.
E-mail address: reynald.bur@onera.fr (R. Bur).

1270-9638/$ – see front matter
doi:10.1016/j.ast.2005.07.008

Keywords: Unsteady flow; Transonic flow; Shock-wave; Separated flow; Flow control

Mots-clés : Ecoulement instationnaire ; Régime transsonique ; Onde de choc ; Ecoulement décollé ; Contrôle de l'écoulement

1. Introduction

Internal flows are often the subject of shock-waves, which interact strongly with turbulent boundary layers [6]. The result is an amplification of dissipative effects, which translates into losses in terms of stagnation pressure, and frequently the formation of separation with always negative consequences: fall of efficiency and high amplitude fluctuations related to the development of large turbulent structures in the separated zones of the flow. The occurrence of excited, unsteady fluctuations in air inlets limits the performance of supersonic aircraft propulsion systems.

Experimental studies were performed by Sajben et al. on shock response to downstream perturbations [2,11,12] or in self-excited response [3,5]. In these configurations, the flow is either attached or undergoes shock-induced separation, depending on shock strength or presence of an adverse pressure gradient. Similar work was conducted by Ott et al. [10] for an excited frequency range of 0 to 180 Hz. These experiments mainly used schlieren visualizations and pressure measurements. Recently, Bur and Berthouze obtained a precise description of unsteady flow by laser Doppler velocimetry (LDV) measurements [1,4]. In this study, the evolutions in space and time of attached boundary layer and oscillating shock were characterized.

The aim of the present study is to investigate a two-dimensional unsteady transonic flow in a channel with strong interaction between an oscillating shock and a separated boundary layer. Schlieren visualizations, unsteady pressure acquisitions and LDV measurements are carried out. Control devices located in the interaction region are tested to evaluate their effects on shock-wave oscillation.

2. Experimental conditions and means of investigation

2.1. Wind tunnel and tested configurations

Experiments were performed in the S8Ch wind tunnel of the ONERA Meudon Center. This facility is a continuous wind tunnel supplied with desiccated atmospheric air. The transonic channel is 100 mm high and has a span of 120 mm at the entrance of the test section. The test set-up consists of a rectilinear upper wall and a lower wall equipped with a contour profile (bump). Nearly-sinusoidal pressure perturbations were introduced at the downstream end of the channel by periodic variation of the second throat section thanks to a rotating elliptical shaft. This system caused forced shock-wave oscillations at a known adjustable frequency.

Control devices – passive and active – have been tested to show theirs effects on the oscillating shock-wave/boundary layer interaction. Passive control is defined by natural flow recirculation through a cavity covered by a perforated plate placed in the shock oscillation region, between the high pressure region downstream of the shock and the upstream low pressure region. Active control means flow suction through the perforated plate. The cavity has a depth of 110 mm and a length of 70 mm. The nominal characteristics of the perforated plate are: porosity 5.67% and 0.3 mm-diameter holes, inclined at 45° with respect to the surface (in the downstream direction) in the upstream half part of the plate and normal to it in its downstream half part. A photograph of the test set-up is shown in Fig. 1 with control devices.

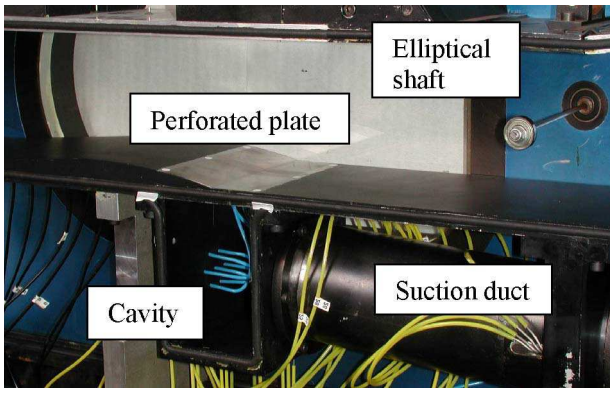

Fig. 1. Photograph of the test set-up with control devices.

The stagnation conditions were near ambient pressure and temperature: $p_{st} = 0.96 \times 10^5 \pm 300$ Pa and $T_{st} = 300 \pm 10$ K. The unit Reynolds number is around 14×10^6. The nominal Mach number is equal to 1.45.

2.2. Flow field visualizations

To visualize the flow field and control the shock-wave positions in the test section, a schlieren apparatus is used. The different recording devices are: a high speed camera Phantom V4.1 coupled with HBO light, a camera Nikon D100 or a Strobodrum™ coupled with a spark light (spark duration: 20 ns). The high-speed camera characteristics are: a resolution of 512 × 512 pixels and an acquisition speed of 1000 frames per second. The Strobodrum™ characteristics are: a rotation of 1200 tr/mn, and a spark frequency of 3000 Hz. As a result, the frame height is 10 mm, and visualization of the upper boundary layer missing.

2.3. Pressure taps and sensors

The lower wall of the test set-up is equipped with 39 continuous pressure taps located on a line at 10 mm from the median plane and 12 unsteady pressure sensors, 6 of which are located on the median plane and 6 along the spanwise direction (only for the reference case). The sketch of Fig. 2 shows the distribution of the pressure taps and sensors along the lower wall (G = Grid, P = Plate).

Nomenclature

c	sound velocity
f	shock oscillation frequency
f_c	excitation (shaft) frequency
M	Mach number
p_{st}	stagnation pressure
Q	suction mass flow rate
Q_0	wind tunnel mass flow rate
T	shock oscillation period
T_{st}	stagnation temperature
$U(X,t)$	instantaneous velocity, measured by the LDV system
X	streamwise coordinate along the channel lower wall, origin at the beginning of the lower wall
Y	coordinate normal to the channel lower wall
$\gamma_{x,y}(f)$	coherence between pressure signals
$\phi_{x,y}(f)$	phase lag between pressure signals
$\varnothing$	sonic throat diameter

Operators

$\langle\rangle$	phase-averaged operator
$\overline{\ }$	ensemble-averaged operator
$\sim$	cyclic operator
$'$	fluctuating operator

The continuous pressure taps have a diameter of 0.4 mm and are connected to Statham^{TM} transducers via rubber tubes. The unsteady pressure transducers are absolute or differential 15 psi Kulite^{TM} XCS093 sensors with a diameter of 0.8 mm.

The origin of the co-ordinate system is located at the beginning of the lower wall, in the median plane.

2.4. LDV system and phase-averaged technique

Probings of the interaction region have been performed by using a two-component laser Doppler velocimetry system (LDV) synchronized with a signal emanating from the rotating shaft. The following results were obtained only from the reference case for an excitation frequency $f_c = 15$ Hz produced by the elliptical shaft.

In order to have a precise description of the upper and lower boundary layers, and to avoid optical problems due to wall proximity, the mesh used for LDV acquisitions was split in two parts for a total of around 5000 points. The first part of the mesh covers the lower boundary layer and the core flow; the second is focused on the upper boundary layer. The longitudinal extension of the mesh is: $285 \leqslant X\,(\text{mm}) \leqslant 445$, which includes the shock oscillation zone. The flow was seeded by DEHS (Di Ethyl Hexyl Sebacate) particles. The average particle size is equal to 0.3 μm.

The phase-averaged technique, introduced by Hussain and Reynolds [9], is applied to LDV measurements to characterize the velocity field. The technique presented here was previously used for the study of a flow over a deep cavity at high-subsonic speed [7]. It can distinguish between the "coherent" motion related to the periodic excitation and a random fluctuating part. The velocity $U(X,t)$ is broken down into three terms:

$$U(X,t) = \overline{U}(X) + \widetilde{U}(X,t) + U'(X,t) \tag{1}$$

where $\overline{U}(X)$ is the ensemble average component, $\widetilde{U}(X,t)$ the cyclic component and $U'(X,t)$ the fluctuating component. The phase-averaged component is defined as:

$$\langle U(X,t)\rangle = \overline{U}(X) + \widetilde{U}(X,t). \tag{2}$$

The remaining fluctuating component should be interpreted as residue characterizing events, which are not in phase with the main signal. In the present case, the phase-averaged velocity is evaluated using a time information. One oscillation period is divided into 60 intervals of 6° each. The beginning of the period is given by an electronic circuit, which locates a marker placed on the rotating shaft. The use of the TSI RMR (Rotating Machinery Resolver) then allows for each laser sample to be arranged in its arrival time in the period.

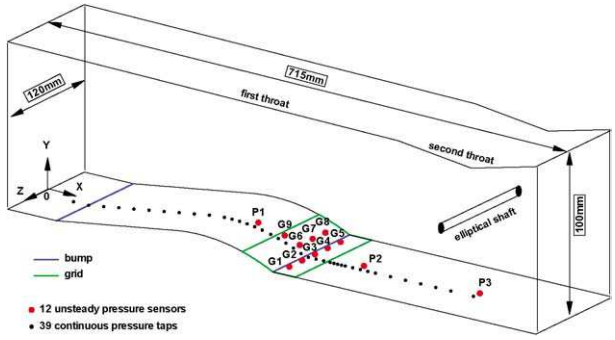

Fig. 2. Sketch of the continuous pressure taps and Kulite sensors positions in the channel.

3. Results for the reference case without control

3.1. Schlieren visualizations

Fig. 3 shows the extreme positions of the shock-wave in the channel for an excitation frequency of $f_c = 15$ Hz. The shock oscillates at a frequency $f = 30$ Hz, which is twice the excitation frequency due to the shape of the shaft. The interaction region is characterized by a large λ-shock structure in the core flow. The behavior of the boundary layer is different between these two positions: in the upstream position, the boundary layer is separated with important vortices structures in the mixing layer; in the downstream position, the boundary layer is attached.

Other excitation frequencies have been tested [8]. As already observed by Ott et al. [10], and Berthouze and Bur [1], the shock oscillation amplitude decreases with increasing excitation frequency. This behavior is due to the existence of a limit condition at high frequencies where the pressure remains

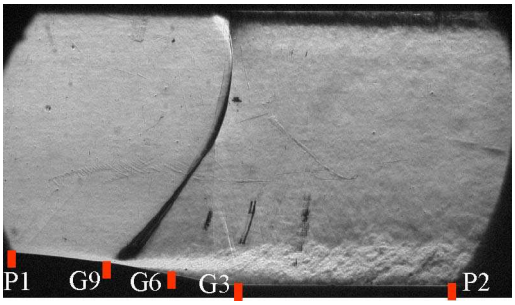

(a)

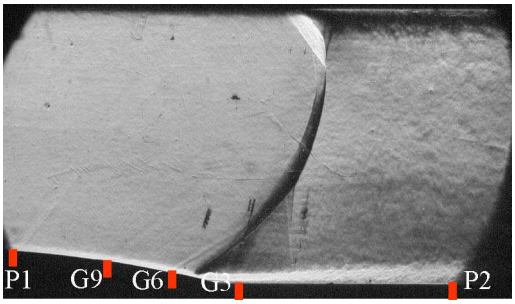

(b)

Fig. 3. Shock-wave positions for an oscillation frequency of 30 Hz – positions of the Kulite sensors in the median plane. (a) Upstream position. (b) Downstream position.

Table 1
Shock oscillation amplitude for three excitation frequencies

f_c (Hz)	f (Hz)	Shock oscillation amplitude (mm)
5	10	50
15	30	30
30	60	21

stable and the shock will not move any longer. Table 1 gives the shock oscillation amplitude for three excitation frequencies. The shock-wave positions in the channel are estimated in the core flow, at $Y \cong 75$ mm, where the shock-wave is nearly-normal.

3.2. Unsteady pressure measurements

Fig. 4 shows the longitudinal evolution of the pressure fluctuations spectra obtained from signals measured by sensors located in the test section median plane, for an excitation frequency $f_c = 15$ Hz. These spectra are represented in Sound Pressure Level (SPL) expressed in dB, by Eq. (3):

$$SPL(\text{dB}) = 20 \times \log_{10}\left(\frac{\sqrt{S_{p'p'}}}{p_{\text{ref}}}\right) \tag{3}$$

where $S_{p'p'}$ is the spectrum modulus, in Pa^2, and p_{ref} is equal to 2×10^{-5} Pa.

The sample frequency is 6000 Hz for each sensor; the spectrum average is obtained from 50 blocks and 8192 samples. The P1 sensor spectrum (at $X = 281.4$ mm) exhibits no particular frequencies because it is located in the supersonic zone of the flow and is not sensible to downstream perturbations. The G9 sensor (at $X = 316.4$ mm) gives a peak at the shock oscillation fundamental frequency $f = 30$ Hz, and some harmonics. These peaks have a weak intensity because this sensor is in border of the shock-wave oscillation. The G6 sensor (at $X = 336.4$ mm) has several harmonics and the fundamental peak very energetic (at $f = 30$ Hz). This sensor picks up very well the shock-wave oscillation. The G3 sensor (at $X = 356.4$ mm, just downstream of the bump) gives the fundamental peak (at $f = 30$ Hz), and only one harmonic is observed. The fundamental peak is less energetic than that of the G6 sensor (160 dB instead of 170 dB). This can be explained by the location of the sensor. Indeed, according to the schlieren visualization (see Fig. 3), this sensor is always located downstream of the strong leading shock, so all the harmonics – except one – have disappeared. The P2 sensor (at $X = 421.4$ mm) and P3 sensor (at $X = 575$ mm, under the shaft) have the same spectrum. These two sensors, which are located in the subsonic zone, are mainly sensible to the downstream pressure perturbation.

Table 2
Phase lag between the P3 sensor and P2, G3, G6 and G9 sensors

Sensors	$\phi_{x,y}$ (rad)
P3/P3	0
P3/P2	−0.5024
P3/G3	−0.8158
P3/G6	−0.8754
P3/G9	−0.8899

In this study, one estimated the coherence between the P3 sensor and the five others located in the median plane. The coherence of the pressure signals has been determined by Eq. (4):

$$\gamma^2_{x,y}(f) = \frac{Co^2_{x,y}(f) + Qu^2_{x,y}(f)}{\|G_{x,x}(f)\|\|G_{y,y}(f)\|} \tag{4}$$

where $Co_{x,y}(f)$ is the co-spectrum and $Qu_{x,y}(f)$ the quad-spectrum; $\gamma^2(f)$ gives the dependence between the signals $x(t)$ and $y(t)$ at the frequency f. If the coherence is equal to 1, the signals are related. There is an important correlation between the P3 sensor and P2, G3, G6 and G9 sensors, but there is no coherence between the P3 and P1 sensors, due to the location of the P1 sensor in the supersonic region.

Table 2 gives the phase lag between the P3 sensor and P2, G3, G6 and G9 sensors. The phase lag between the signals is given by Eq. (5):

$$\phi_{x,y}(f) = \tan^{-1}\left[\frac{Qu_{x,y}(f)}{Co_{x,y}(f)}\right]. \tag{5}$$

Thanks to the values reported in Table 2, the downstream perturbation velocity is obtained by Eq. (6):

$$C(f) = \frac{2\pi f}{\nu(f)} \tag{6}$$

where $\nu(f)$ is the average slope of the straight line in Fig. 5. The downstream perturbation phase velocity, at the frequency of $f = 30$ Hz, is equal to around 52 m/s.

This phase velocity obtained from unsteady pressure measurements is nearly equal to $(c - U)$, where c is the sound speed and U the average flow velocity downstream of the interaction region.

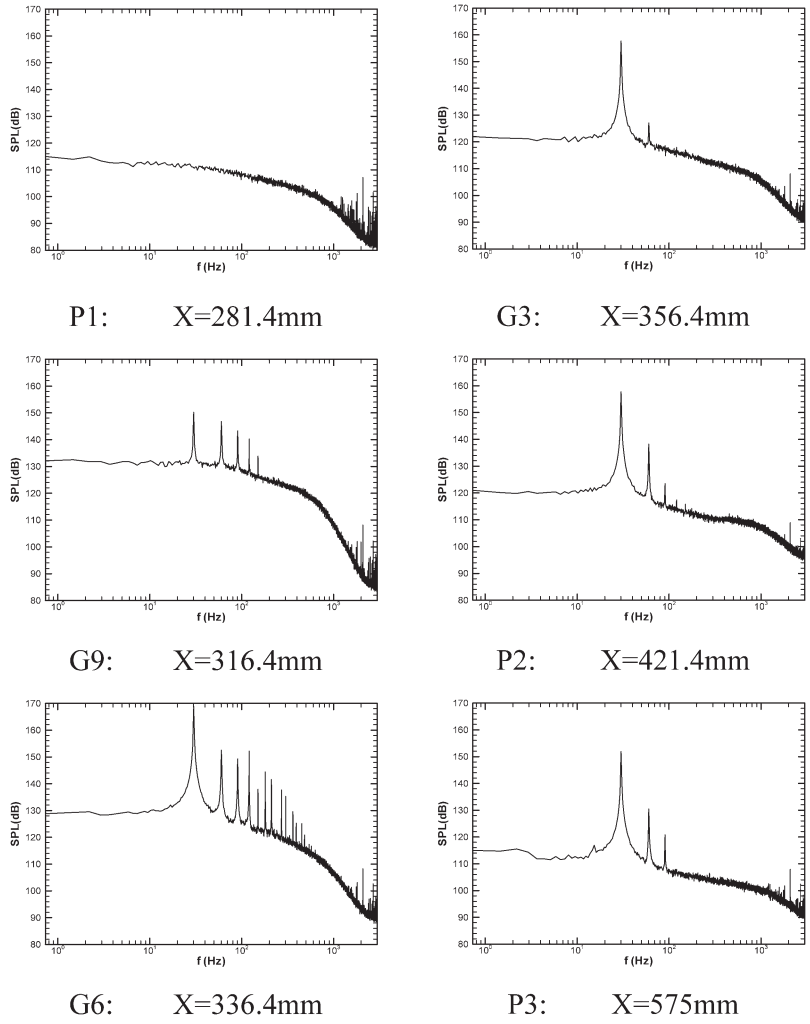

Fig. 4. Longitudinal evolution of the pressure fluctuations spectra for a 30 Hz shock oscillation.

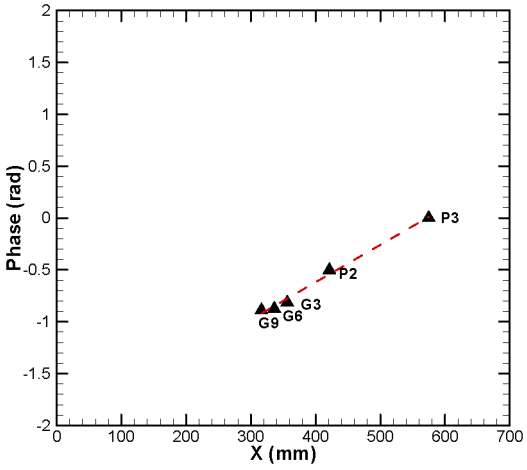

Fig. 5. Phase lag between the P3 sensor and P2, G3, G6 and G9 sensors at the shock frequency $f = 30$ Hz.

3.3. LDV results

Fig. 6 shows the evolution of the Mach number during a period T of the shock oscillation. The large λ-shock structures of the interaction region are very similar to those observed on the schlieren visualizations (see Fig. 3). For $t = 0$, the shock-wave is in its upstream position, the Mach number in front of the shock being around 1.3. Moreover, the LDV measurements allow for the separated flow to be quantified: the longitudinal extension of the separated bubble is equal to 62 mm (from $X = 328$ mm to $X = 390$ mm). The maximum negative velocity is equal to -77 m/s. When the shock-wave is in downstream position, at $t = T/2$, the Mach number is equal to 1.5 and there is no separated region. Moreover, a slip line is clearly observed in the visualization. The shock oscillation amplitude is equal to 30 mm, which has already been highlighted by the schlieren visualizations analysis (see in Table 1).

4. Control devices effects

Two control devices, passive and active, have been tested to analyze theirs effects on the shock-wave/boundary layer interaction, especially on the shock-wave oscillation amplitude.

4.1. Passive control case

As for the reference case, schlieren visualizations have been obtained for a shock-wave oscillation frequency equal to 30 Hz.

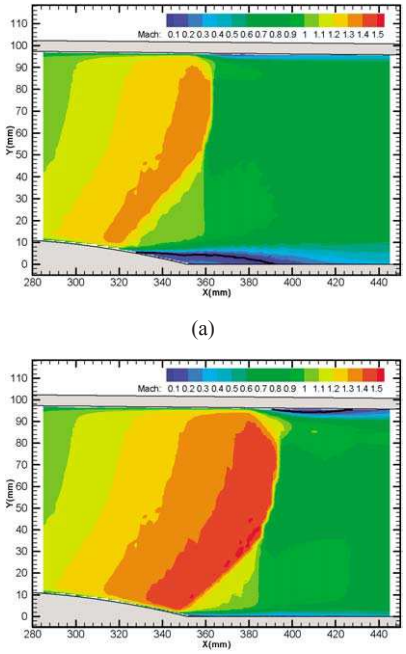

(a)

(b)

Fig. 6. Mach number distributions obtained by LDV measurements during a period T of the shock oscillation ($f = 30$ Hz). (a) Upstream position ($t = 0$). (b) Downstream position ($t = T/2$).

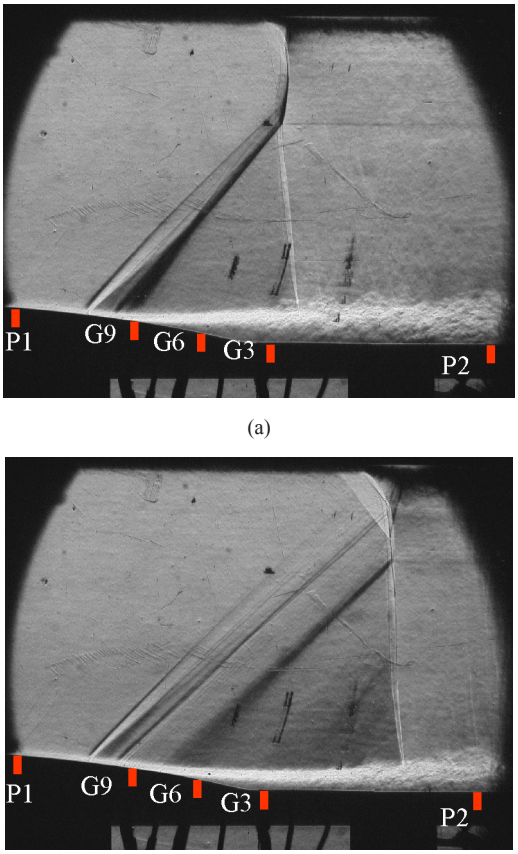

(a)

(b)

Fig. 7. Shock-wave positions with passive control – positions of the Kulite sensors in the median plane. (a) Upstream position. (b) Downstream position.

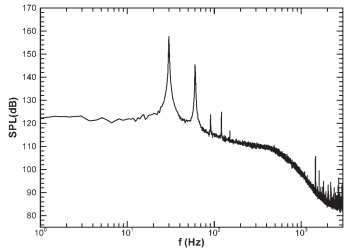

G9: X=316.4mm

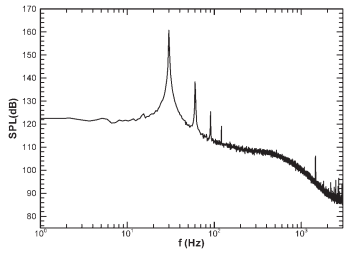

G6: X=336.4mm

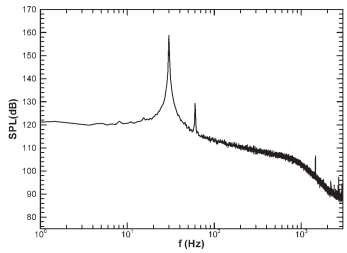

G3: X=356.4mm

Fig. 8. Longitudinal evolution of the pressure fluctuations spectra for a 30 Hz shock oscillation with passive control.

Fig. 7 shows the extreme positions of the shock-wave in the channel. The main difference with the reference case is concerned with the shock structure. Indeed, the triple point is located higher in the channel. An effect of viscous ramp, due to the injection of the flow in the upstream part of the perforated plate, forced the position of the leading shock. Furthermore, the boundary layer is always destabilized. The shock-wave amplitude is equivalent to that of the reference case ($\Delta X = 30$ mm). So the passive control has no effect on the shock-wave oscillation.

Fig. 8 shows the longitudinal evolution of the pressure fluctuations spectra with passive control, only for the three sensors located in the shock oscillation region (see Fig. 7). The G9 and G6 sensors have the same spectrum with a fundamental peak (at $f = 30$ Hz) and few harmonics almost at the same levels. This behavior is due to the fact that the G9 sensor corresponded to the upstream location of the leading shock and the G6 sensor to its downstream position. The G3 sensor always remains downstream of the leading shock and also has an equivalent behavior to that of the reference case.

4.2. Active control case

Fig. 9 shows the extreme positions of the shock-wave for an oscillation frequency $f = 30$ Hz, with the active control. The

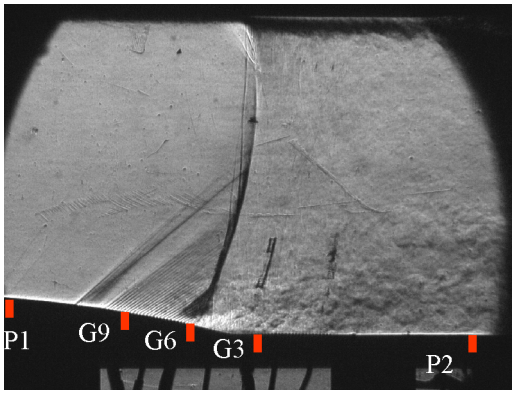

(a)

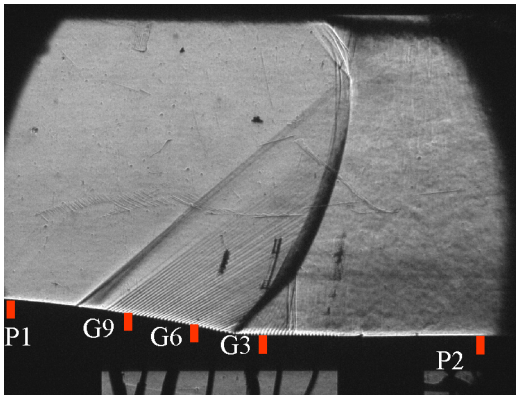

(b)

Fig. 9. Shock-wave positions with active control ($Q/Q_0 = 1\%$) – positions of the Kulite sensors in the median plane. (a) Upstream position. (b) Downstream position.

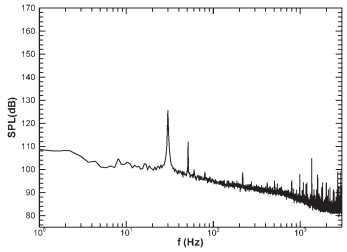

G9: X=316.4mm

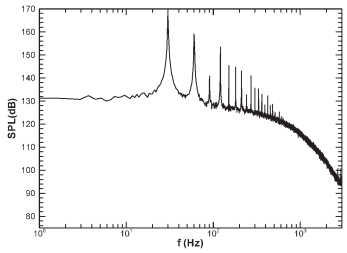

G6: X=336.4mm

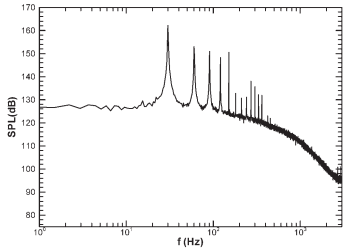

G3: X=356.4mm

Fig. 10. Longitudinal evolution of the pressure fluctuations spectra for a 30 Hz shock oscillation with active control ($Q/Q_0 = 1\%$).

suction mass flow rate is measured by means of a sonic throat. Several sonic throat diameters have been tested: 10, 15, 20 and 30 mm. The visualizations of Fig. 9 are obtained with a sonic throat diameter of 20 mm, which leads to a normalized suction mass flow rate $Q/Q_0 = 1\%$. The shock-wave structure is modified by the active control. In the upstream shock position, the λ-shock structure and the boundary layer separation have almost disappeared. The shock oscillation amplitude is strongly reduced. This indicates that the active control has a significant effect in reducing the shock-wave oscillation thanks to suction of the boundary layer through the perforated plate.

Fig. 10 shows the impact of active control by suction on the pressure fluctuations spectra for the sensors located in the shock oscillation region (see Fig. 9). In this case, the G9 sensor has a weak mean level and only two peaks. This sensor is located in the supersonic flow region. The G6 and G3 sensors have important mean levels with a fundamental peak and several harmonics. These two sensors catch very well the shock-wave oscillation. The G6 sensor spectrum is close to that of the reference case. But the behavior of the G3 sensor is totally different to that of the reference case (see Fig. 4) because of the decrease in the shock-wave amplitude thanks to the active control.

Table 3 gives a comparison on the shock oscillation amplitude between the reference case and the cases with passive and active control. Active control by suction enables a decrease in the shock oscillation amplitude. For a moderate value of the suction mass flow rate, equal to 20.3 g/s, thus 1% of the total mass flow rate ($Q_0 = 2.3 \times 10^3$ g/s), the decrease in oscillation amplitude is around 20% (from 30 mm to 23.6 mm).

Table 3
Evolution of the amplitude of the shock-wave oscillation with control devices

Diameter of sonic throat ∅ (mm)		Suction mass flow rate		Amplitude of the oscillation ΔX (mm)
		Q (g/s)	Q/Q_0 (%)	
Reference case				30
Passive control				30
Active control	10	7.8	0.4	27
	15	14.3	0.6	25
	20	20.3	1	23.6
	30	Choked rate		23.6

5. Conclusion

The experimental study of a two-dimensional unsteady transonic flow was carried out in a channel with strong interaction between an oscillating shock-wave and a separated boundary layer. The aim of the study was to obtain a precise description of the unsteady flow in order to characterize the evolution in space and time of the separated boundary layer and the shock.

Results were obtained from shock-wave response to downstream perturbations generated by a rotating elliptical shaft at an excited frequency of 15 Hz. For the reference case, without control, schlieren visualizations allowed to have a precise description of the shock-wave/boundary layer interaction and to quantify the shock oscillation amplitude. Unsteady pressure measurements coupled with a spectral analysis showed the effect of the leading shock oscillation of the λ-shock structure on the response of the sensors; moreover, it enabled the determination of the downstream perturbations phase velocity. Two-component laser Doppler velocimetry probings were carried out and phase-averaged fields obtained thanks to a time information given by a marker located on the rotating shaft. The results allowed for the evolution of the separated bubble to be quantified during a shock-wave oscillation period.

The effects of control devices – passive and active by suction – on the boundary layer and the forced oscillation of the shock-wave were characterized. Passive control had no effect on the shock oscillation amplitude. On the contrary, active control decreased the shock oscillation amplitude thanks to suction of the separated boundary layer across the perforated plate.

Acknowledgements

The authors wish to thank D. Soulevant for the laser Doppler velocimetry campaign in S8Ch wind tunnel. They would also thank P. Geffroy for his helpful advice.

References

[1] P. Berthouze, R. Bur, Experimental investigation of the response of a transonic shock-wave to downstream perturbations, AIAA Paper 2001-3295, 2001.

[2] T.J. Bogar, M. Sajben, J. Kroutil, Response of a supersonic inlet to downstream perturbations, AIAA Paper 83-2017, 1983.

[3] T.J. Bogar, M. Sajben, J. Kroutil, Characteristics frequencies of transonic diffuser flow oscillations, AIAA J. 21 (9) (1983) 1232–1240.

[4] R. Bur, P. Berthouze, Forced oscillation of a shock-wave in a transonic channel flow, in: H. Sobieczky (Ed.), Proceedings of the IUTAM Symposium Transonicum IV, Göttingen, Germany, September 2–6, 2002, vol. 73, Kluwer Academic Publishers, 2003, pp. 47–52.

[5] C. Chen, M. Sajben, J. Kroutil, Shock-wave oscillations in a transonic diffuser flow, AIAA J. 17 (10) (1979) 1076–1083.

[6] J. Délery, J. Marvin, Shock-wave/boundary layer interactions, in: E. Reshotko (Ed.), AGARDograph AG-280, 1985.

[7] N. Forestier, L. Jacquin, P. Geffroy, The mixing layer over a deep cavity at high-subsonic speed, J. Fluid Mech. 475 (2003) 101–145.

[8] A. Galli, B. Corbel, R. Bur, Forced shock-wave oscillations and separated boundary-layer interaction, AIAA Paper 2004-5199, 2004.

[9] A. Hussain, W. Reynolds, The mechanics of an organised wave in turbulent shear flow, J. Fluid Mech. 41 (2) (1970) 241–258.

[10] P. Ott, A. Bölcs, T. Fransson, Experimental and numerical study of the time-dependent pressure response of a shock-wave oscillating in a nozzle, ASME J. Turbomachinery 117 (1995) 106–114.

[11] M. Sajben, T.J. Bogar, J. Kroutil, Forced oscillation experiments in supercritical diffuser flows, AIAA J. 22 (4) (1984) 465–474.

[12] J.T. Salmon, T.J. Bogar, M. Sajben, Laser Doppler velocimeter measurements in unsteady, separated, transonic diffuser flows, AIAA J. 21 (12) (1983) 1690–1697.

ANNEXE B - SEPARATION CONTROL BY VORTEX GENERATOR DEVICES IN A TRANSONIC CHANNEL FLOW

Bur R., Coponet D. et Carpels Y.

Shock Waves Journal, Vol. 19, No. 6, Dec. 2009, pp. 521-530

Shock Waves (2009) 19:521–530
DOI 10.1007/s00193-009-0234-6

ORIGINAL ARTICLE

Separation control by vortex generator devices in a transonic channel flow

Reynald Bur · Didier Coponet · Yves Carpels

Received: 4 February 2009 / Revised: 10 July 2009 / Accepted: 1 October 2009 / Published online: 23 October 2009

Abstract An experimental study was conducted in a transonic channel to control by mechanical vortex generator devices the strong interaction between a shock wave and a separated turbulent boundary layer. Control devices—co-rotating and counter-rotating vane-type vortex generators—were implemented upstream of the shock foot region and tested both on a steady shock wave and on a forced shock oscillation configurations. The spanwise spacing of vortex generator devices along the channel appeared to be an important parameter to control the flow separation region. When the distance between each device is decreased, the vortices merging is more efficient to reduce the separation. Their placement upstream of the shock wave is determinant to ensure that vortices have mixed momentum all spanwise long before they reach the separation line, so as to avoid separation cells. Then, vortex generators slightly reduced the amplitude of the forced shock wave oscillation by delaying the upstream displacement of the leading shock.

Keywords Transonic flow · Shock wave · Boundary layer · Separated flow · Vortex generator

PACS 47.27.nd · 47.40.Nm · 47.32.Ff · 47.85.L−

1 Introduction

Both external and internal flows are often the subject of shock waves, which interact strongly with turbulent boundary layers. The result is frequently the formation of separation with always negative consequences: drag penalty, fall of efficiency and high amplitude fluctuations related to the development of large turbulent structures in the separated zones of the flow. This leads to decrease the performance of a supercritical wing aircraft and to limit the efficiency of supersonic aircraft or missile propulsion systems.

Thus, mechanical vortex generator devices (VGs) allowing momentum transfer have been successfully used for a long time to delay flow separation [1]. They introduced vorticity of an appropriate sign and direction and increased the mixing between the upper and lower layers of the turbulent boundary layer. Recent reviews [2–4] on flow control technology associated with their range of applicability have given a list of vortex generator devices tested to control the boundary layer separation. They may take the form of vanes or obstacles, air jets or mass-less jets. Nevertheless, control of shock-induced separation by such vortex generator devices is not widely discussed in the literature. McCormick's experiments [5] revealed that sub boundary layer doublet VGs (its height h is equal to 0.36 the incoming boundary layer thickness δ) significantly suppress the shock-induced separation bubble and improve the boundary layer properties downstream of the shock. However, he noticed a wave drag penalty due to the modification of the shock pattern from a λ-foot shock system to a quasi-normal shock wave. Ashill et al. [6] reported tests on a transonic airfoil equipped with several VGs devices. The sub counter-rotating vane-type VGs (h at the scale of the boundary layer displacement thickness δ^*) produced a 20% increase of the maximum lift when their location towards the shock position is well chosen; i.e., $70\,h$ upstream of the shock. The choice of the distance between the VGs and the interaction region to efficiently control the shock-induced separation is well evidenced by Babinsky et al. [7]. It was observed that the most

Communicated by J.-P. Dussauge.

R. Bur (✉) · D. Coponet · Y. Carpels
Fundamental and Experimental Aerodynamics Department,
ONERA, 92190 Meudon, France
e-mail: Reynald.Bur@onera.fr

efficient location of micro counter-rotating vane-type VGs (around 20% of the incoming boundary layer thickness δ) depends on the nominal (diffuser entry) Mach number. When the Mach number is increased, a downstream placement of the VGs closer to the separation onset was found to be more beneficial.

The purpose of the present experimental study is to control by mechanical (passive) vortex generator devices the strong interaction between a shock wave and a separated turbulent boundary layer in a transonic channel. Control devices—co-rotating and counter-rotating vane-type VGs—are implemented upstream of the shock foot region and are tested both on a steady shock wave and on a forced shock oscillation configurations.

2 Experimental conditions and means of investigation

2.1 Wind tunnel and flow conditions

Experiments were performed in the S8Ch wind tunnel of the ONERA Meudon Center. This facility is a continuous wind tunnel supplied with desiccated atmospheric air. The transonic channel is 100 mm high and has a span of 120 mm at the entrance of the test section (see Fig. 1). The test set-up consists of a rectilinear upper wall and a lower wall equipped with a contour profile (bump). The shape of the bump has been specially designed to induce a strong interaction between the boundary layer and the shock when it takes place at the level of the rear part of the bump, the nominal Mach number being equal to 1.45. Such an interaction induced an extended separated zone.

The stagnation conditions were near ambient pressure and temperature: $p_{st} = 0.96 \times 10^5 \pm 300$ Pa and $T_{st} = 300 \pm 10$ K. Probing using a two-component laser Doppler velocimetry (LDV) system has been performed in the front part of the bump, where the flow is still subsonic, in order to give inlet flow conditions for computations [8]. At the station $X = 135$ mm (see Fig. 4 for the definition of the co-ordinate system), the boundary layer on the bump is fully turbulent with the following characteristics: physical thickness $\delta = 4$ mm, displacement thickness $\delta^* = 0.46$ mm, momentum thickness $\theta = 0.25$ mm, and incompressible shape parameter $H_i = 1.6$. The associated unit Reynolds number is around $14 \times 10^6\,\mathrm{m}^{-1}$, which leads to a value of $Re_\theta = 3500$ for the incoming flow. Moreover, previous experiments on the same configuration have allowed to determine the boundary layer properties at the beginning of the rear part of the bump, upstream of the interaction region [9]. These properties are very similar to those obtained in the converging part of the channel, the pressure gradients being weak in the bump crest region (sonic flow condition).

Fig. 1 Photograph of the test set-up in the S8Ch wind tunnel

Nearly sinusoidal pressure perturbations were introduced at the downstream end of the channel by periodic variation of the second throat section thanks to a rotating elliptical shaft located near this throat, in the middle of the channel [10]. This device caused forced shock-wave oscillations at a known adjustable frequency. In these experiments, the shock oscillation frequency is equal to 30 Hz, which produces a shock oscillation amplitude of around 30 mm. Similar experimental studies on shock response to downstream perturbations were performed by Sajben et al. [11,12] and Ott et al. [13].

2.2 Vortex generator devices

The mechanical vane-type vortex generators were triangular elements whose angular position is fixed at 18° with regard to the main flow direction. It is consistent with the results of Pauley et al. [14] who observed a linear increase of the vortices strength up to an angle of 18°. Several parameters have been tested both for co-rotating VGs and counter-rotating VGs (see Fig. 2). An important parameter to take into account in the study is the VGs height h, as referred to in previous studies [3,4,15]. Then, conventional VGs (with $h/\delta = 1$, noted CoC and C) have been compared to sub-VGs (with $h/\delta = 0.5$, noted CoS and S). Concerning the counter-rotating VGs, the effect of spacing between each couple of VGs have been tested ($\lambda/h = 10$ and 5, respectively, for the devices C1, S1 and C2, S2).

Moreover, the number of VGs has been adapted for each configuration in order to cover the entire span of the test set-up. The VGs devices are located along a line situated at 10 mm downstream of the bump crest. This position has been selected thanks to 3D numerical simulations carried out to optimize the efficiency of VGs to delay the separation [16]. It corresponds to a distance upstream of the shock foot equal to 32δ for the sub-VGs (16δ for the conventional VGs), which is in the range of values found in the literature [3–7]. Finally,

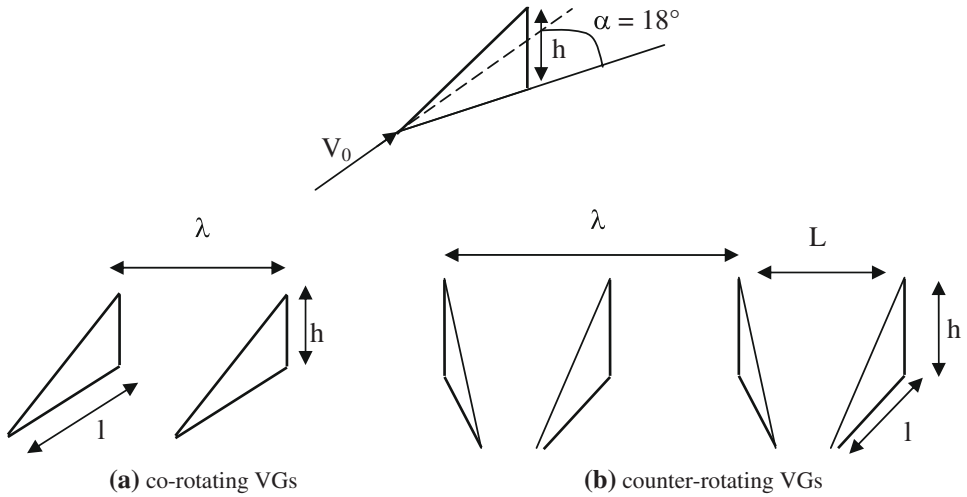

Fig. 2 Definition of the vane-type vortex generators

(a) co-rotating VGs **(b)** counter-rotating VGs

Table 1 Geometrical parameters of the vane-type vortex generators

	Co-rotating VGs		Counter-rotating VGs			
	CoC1	CoS1	C1	C2	S1	S2
h/δ	1	0.5	1	1	0.5	0.5
l/h	2.5	2.5	2.5	1.25	2.5	1.25
L/h	–	–	3	1.5	3	1.5
λ/h	6	6	10	5	10	5
Number	5	9	3	5	5	11

six configurations of vane-type vortex generators were under study in these experiments (see Table 1; Fig. 3).

One notices that the efficiency of these VGs devices to control the shock-induced separation should be compared to passive and active bleed devices tested in a previous study. This device consisted of a cavity covered by a perforated plate placed in the interaction region. Passive control is defined by a natural flow recirculation through the cavity and active control means flow suction through the perforated plate [10].

2.3 Flow visualizations

A schlieren apparatus was used to visualize the flow field and control the shock wave positions in the test section. It used a conventional z-type mirror system with a horizontal knife edge. The recording device is a high-speed camera Phantom V7.0 coupled with HBO light. The high-speed camera characteristics are a resolution of 800 × 400 pixels and an acquisition speed of 4,000 frames per second.

Laser sheet visualizations and oil flow visualizations—by means of coloured viscous coat—were performed to allow tracking of the trajectories of the small-scale streamwise vortices emanating from the VG devices and their interaction with the boundary layer and the shock wave. For the laser sheet visualizations, the set-up used is a Millenia Spectra Physics diode pump laser, with a 5-W light power. The wave length of the light is $\lambda = 532 \times 10^{-3}$ µm, which corresponds to the green colour. The flow was seeded by synthetic smoke (Pro-Smoke Super Fluid containing polyglycols) emanating from the settling chamber of the wind tunnel. Concerning oil flow visualizations, viscous coat is applied before each test along the span of the test section just upstream of the VG devices.

2.4 Pressure taps and sensors

The lower wall of the test set-up was equipped with 39 continuous pressure taps located on a line at 10 mm from the median plane and six unsteady pressure sensors (named P and G) located on the median plane, primarily in the interaction region. Figure 4 shows their distributions along the lower wall of the channel.

The continuous pressure taps have a diameter of 0.4 mm and are connected to Statham^{TM} transducers via rubber tubes. The unsteady pressure transducers are absolute or differential 15psi Kulite^{TM} XCS093 sensors with a diameter of 0.8 mm. Pressure measurement uncertainties are ±800 Pa for the Statham^{TM} transducers and ±105 Pa for the Kulite^{TM} sensors, respectively.

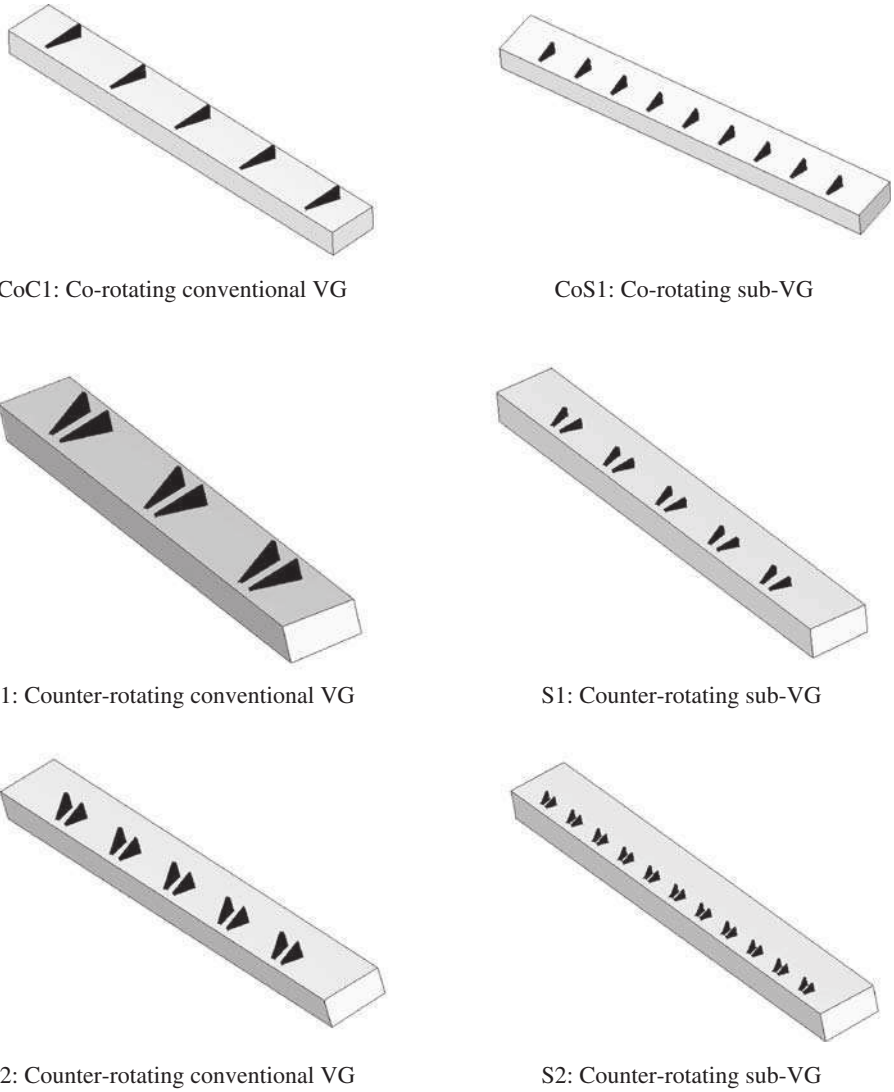

Fig. 3 Configurations of the vane-type vortex generators under study

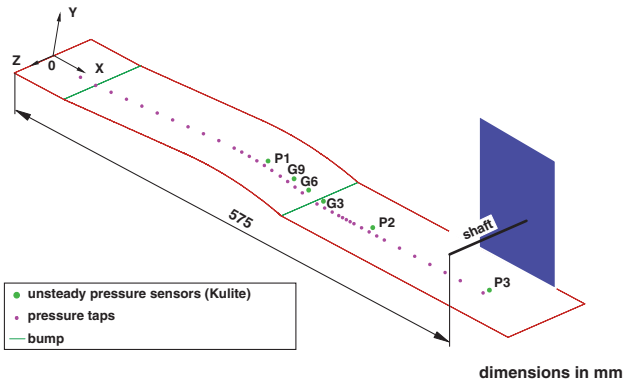

Fig. 4 Sketch of the pressure taps and Kulite sensors positions along the lower wall of the channel

The origin of the co-ordinate system is at the beginning of the lower wall (see Fig. 4). The X-axis is along the lower wall in the streamwise direction, Y is normal to the lower wall and the bump chord and Z is along the spanwise direction ($Z = 0$ in the median plane). The origin of the bump is at $X = 65$ mm. Its length is 286.4 mm and its crest 12 mm. The VG devices are located at $X = 261.4$ mm, 10 mm downstream of the bump crest.

3 Results for the steady shock wave configuration

3.1 Schlieren visualizations

Figure 5 compares the schlieren visualizations between the reference case without control and the control case with counter-rotating VG-C2. In the reference case (see Fig. 5a), the interaction region is characterized by a large λ-shock structure in the core flow. The oblique leading shock, downstream of which the Mach number is still supersonic, and the trailing shock meet at the triple point from which starts the

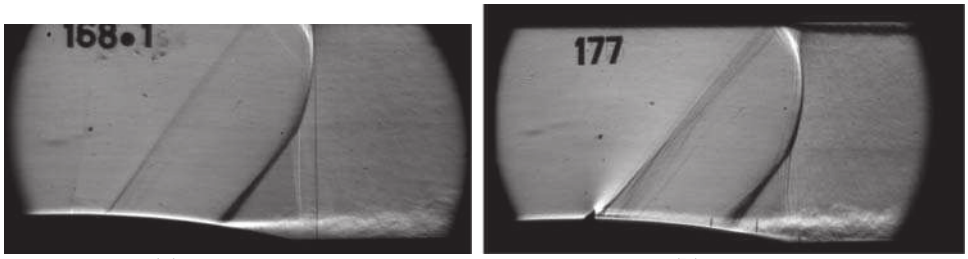

(a) reference case **(b)** VG-C2

Fig. 5 Schlieren visualizations for steady shock wave configuration without control **(a)** and with VG-C2 device **(b)**

single strong shock. The boundary layer is destabilized with massive separation and large vortex structures are developed in the shear stress layer. The wave visible upstream of the interaction region is created by the junction between the bump and the insert manufactured for the clean case, like those of Fig. 3 without VGs. However, the intensity of this wave is very weak and does not generate perturbation in the interaction region [8]. For the control case (see Fig. 5b), the size of the λ-shock structure is reduced compared to the reference case, the position of the triple point being lower in the channel. The trails of the vortices generated by the VGs are observed near the curved wall. The extension of the separation region is reduced under the effects of VGs and the shear layer is growing. The presence of VGs generates expansion waves followed by moderate compression waves in the channel flowfield.

3.2 Wall pressure distributions

The lower wall pressure distributions are plotted in Fig. 6 for the reference case without control and the six VG devices. The reference case distribution reveals the existence of a large separation region corresponding to a quasi-plateau pressure level after the intense recompression of the flow. According to previous experiments with LDV measurements [8,10], the separation point is located near $X = 328$ mm and the reattachment point around $X = 390$ mm. When control by VGs is applied, the plateau pressure seems to disappear and the efficiency of VGs to delay the separation region increases when the spacing between VGs is decreasing (S2 compared to S1, C2 to C1). Then, the VG-S2 device (11 pairs of counter-rotating sub-vortex generators) seems to suppress the separation in the near-median plane of the test section. For this configuration with a large number of VGs in the spanwise direction, previous numerical simulations have indicated that the pairs of vortices emanating from each VG do not merge in the boundary layer upstream of the interaction region [16].

The flow perturbations—expansion and compression waves observed on schlieren visualization (see Fig. 5b)—generated by the VGs have a slight intensity and only have a local effect on the pressure distributions. In term of drag penalties, the way to reduce the effects of these perturbations

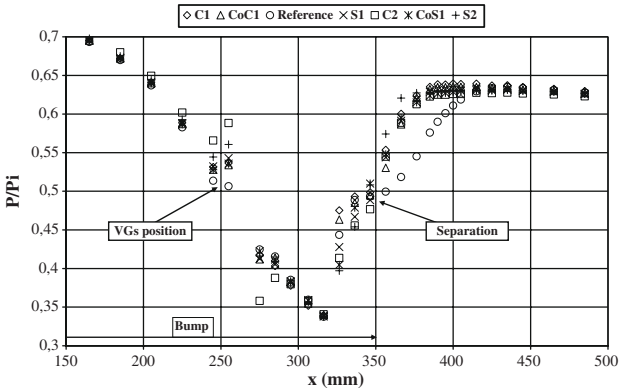

Fig. 6 Wall pressure distributions for steady shock wave configuration without control and with VG devices

is to impose the height of the VGs at a value less than the sonic line of the incoming boundary layer [5–7]. Probing of the boundary layer on the rear part of the bump, upstream of the interaction region, has allowed to determine sonic condition at $h^* = 0.5$ mm [9]. In these experiments, the height of the tested VG devices is always greater than the location of the sonic line; i.e., $h/h^* = 8$ and 4 for the conventional and sub-VGs, respectively.

3.3 Laser sheet visualizations

Figure 7 shows laser sheet visualizations for four spanwise planes located between the conventional counter-rotating VG-C2 device and the separation flow region. In the first plane located in the near-wake of the VG device (see Fig. 7a), one can observe the birth of pair of vortices emanating from the VGs, with a singular comma-shape due to the triangular surface of the VGs. In the plane located at 5δ downstream of VGs (see Fig. 7b), well-formed vortices are convected inside the boundary layer, as already observed in the schlieren picture of Fig. 5b. For the plane located at 15δ downstream of VGs, near the shock foot region (see Fig. 7c), the distance between two vortices (generated by a VG device) is growing compared to those of the previous planes. Considering the last plane located inside the separation region (see Fig. 7d), one notices a significant modification of the near-wall flow pattern. Due to the presence of shock waves, the size of the

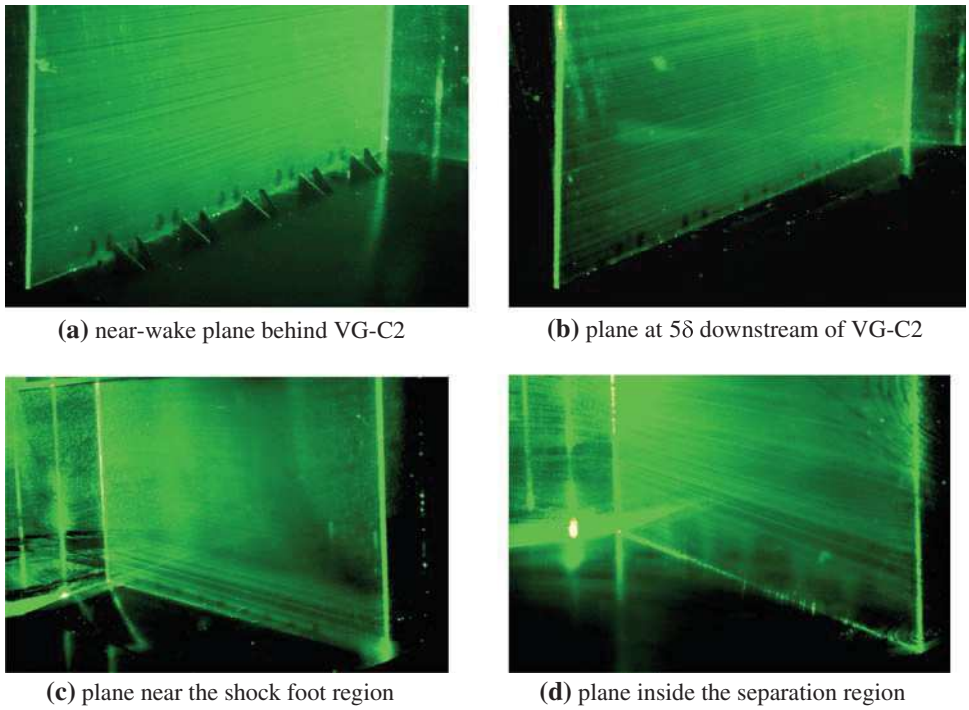

(a) near-wake plane behind VG-C2

(b) plane at 5δ downstream of VG-C2

(c) plane near the shock foot region

(d) plane inside the separation region

Fig. 7 Laser sheet visualizations for steady shock wave configuration—spanwise planes located between the VG-C2 device and the separation region

vortices is increased; the vorticity rate is modified due to the reduction of the axial velocity after the crossing of vortices through the shock system. Their trajectories are slightly changed, but the distance between vortices is still increasing; then, a vortex emanating from a VG device is merging with a vortex issuing from the next VG to form a large vortex structure (see in the plane the black pockets without seeding particles). This mechanism allows to catch the flow from the upper layer of the boundary layer to the less energetic inner layer and, then, to strongly reduce the separation region of the flow.

3.4 Oil flow visualizations

Coloured oil flow visualizations have been performed for the steady shock wave configurations without control and with several VG devices. A comparison between the reference case (see Fig. 8a) and the control case with VG-C2 device (see Fig. 8b) allows to notice an important modification of the flow separation pattern: the separation line located in the rear part of the bump is replaced by a corrugated separated line due to the presence of intense vortices. The flow seems to be partially reattached under the action of VGs vortices. The merging of vortices created by two close VG devices to form large vortex structures is evidenced by their footprints on the lower wall. For the VG-C2 device, the four vortex footprints are corresponding to the four black pockets observed by laser sheet visualization (see Fig. 7d). The effect of VG height is discussed by a comparison between the conventional VG-C2 (see Fig. 8b) and the sub-VG-S1 (see Fig. 8c). The VG height seems to have a slight influence on the flow topology, especially on flow separation extension. One notes a significant interaction with corner flows, which are not controlled in this study. Then, a comparison between counter-rotating VG-S1 (see Fig. 8c) and co-rotating VG-CoS1 (see Fig. 8d) shows that a non symmetrical flow topology is obtained for the co-rotating VGs with smaller footprints of vortices at the wall. This co-rotating VGs configuration is more adapted to control a full 3-D flow, for instance, on a swept wing. The skin friction lines pattern near the leading edge of the wing leads to choose an averaged value for the VGs angular position regarding the upstream flow direction, which is easier to achieve with co-rotating VGs device [6,17].

4 Results for the forced shock oscillation configuration

4.1 Schlieren visualizations

Figure 9 shows the extreme positions of the shock wave in the channel for the shock oscillation frequency of 30 Hz, considering the reference case without control. The corresponding shock oscillation amplitude is equal to 30 mm. The shock positions in the channel are estimated in the core flow, at $Y = 75$ mm, where the shock wave is nearly normal. The interaction region is characterized by a large λ-shock structure in the core flow. The behaviour of the boundary layer is different between these two shock positions: in the upstream position, the boundary layer is separated with important vortex structures in the shear layer; in the down-

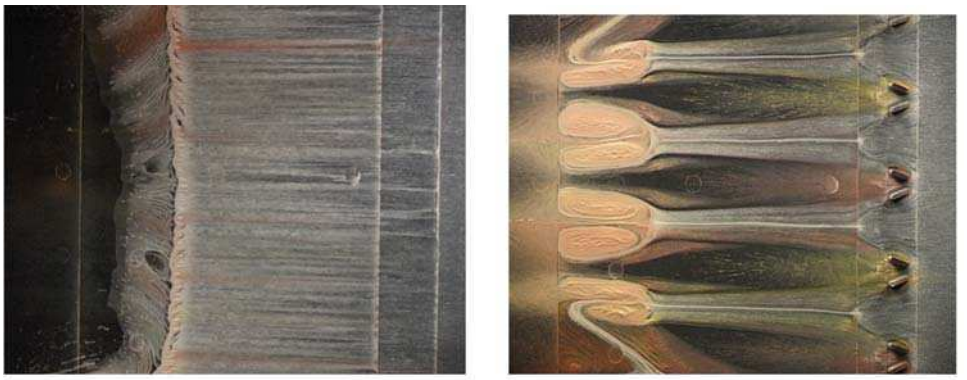

(a) reference case **(b)** conventional counter-rotating VG-C2

(c) counter-rotating sub-VG-S1 **(d)** co-rotating sub-VG-CoS1

Fig. 8 Oil flow visualizations for steady shock wave configuration without control and with several VG devices (direction of the flow is *right-to-left*)

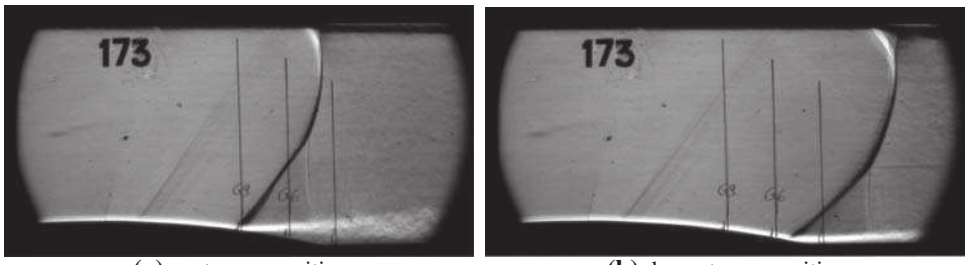

(a) upstream position **(b)** downstream position

Fig. 9 Schlieren visualizations for 30 Hz-forced shock oscillation configuration—reference case without control

stream position, the boundary layer is attached. More in-depth analysis of the flowfield was obtained in a previous study by LDV probing with phase-averaged technique using time information given by a marker placed on the rotating shaft [8,10].

4.2 Unsteady pressure measurements

Figure 10 shows the longitudinal evolution of the pressure fluctuations spectra obtained from signals measured by sensors located in the test section median plane, at the 30 Hz shock oscillation, for the reference case without control. These spectra are represented in sound pressure level (SPL) expressed in dB, by

$$\mathrm{SPL(dB)} = 20 \times \log_{10}\left(\frac{\sqrt{S_{p'p'}}}{p_{\mathrm{ref}}}\right)$$

where $S_{p'p'}$ is the spectrum modulus, in Pa^2, and p_{ref} is equal to 2×10^{-5} Pa. The sample frequency is 6,000 Hz for each sensor; the spectrum average is obtained from 50 blocks and 8,192 samples.

The P1 sensor spectrum (at $X = 281.4$ mm) exhibits no particular frequencies because it is located in the supersonic zone of the flow and is not sensible to downstream perturbations. The G9 sensor (at $X = 316.4$ mm) gives a peak at the shock oscillation fundamental frequency $f = 30$ Hz, and some harmonics. These peaks have a weak intensity because

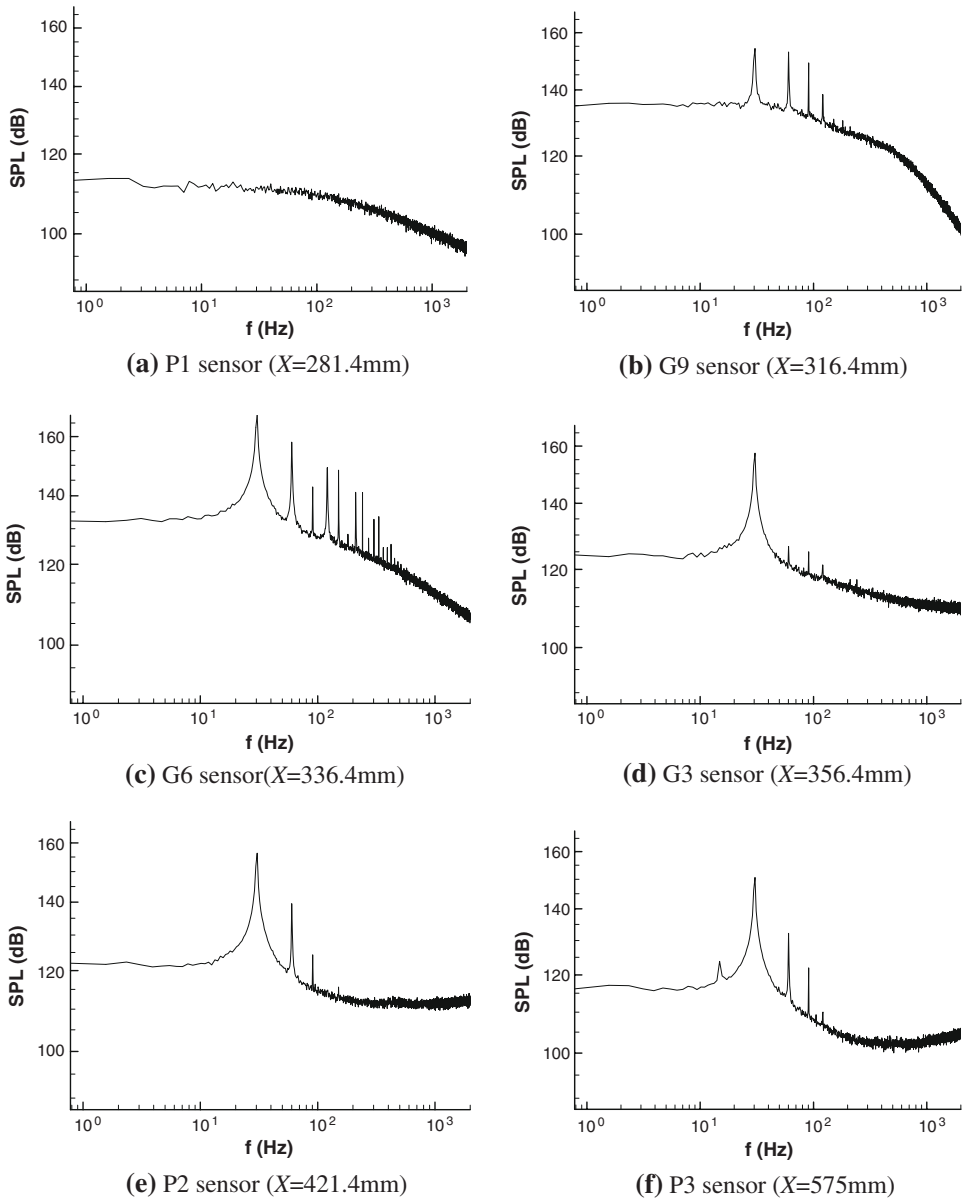

Fig. 10 Longitudinal evolution of the pressure fluctuations spectra for 30 Hz-forced shock oscillation configuration—reference case without control

this sensor is in border of the shock wave oscillation. The G6 sensor (at $X = 336.4$ mm) has several harmonics and the fundamental peak very energetic (at $f = 30$ Hz). This sensor picks up very well the shock wave oscillation. The G3 sensor (at $X = 356.4$ mm, just downstream of the bump) gives the fundamental peak (at $f = 30$ Hz) and very weak harmonics. The fundamental peak is less energetic than that of the G6 sensor (158 dB instead of 168 dB). This can be explained by the location of the sensor. Indeed, according to the schlieren visualizations (see Fig. 9), this sensor is always located downstream of the leading shock, so all the harmonics have nearly disappeared. The P2 sensor (at $X = 421.4$ mm) and P3 sensor (at $X = 575$ mm, under the shaft) have almost the same spectrum. These two sensors, which are located in the subsonic zone, are mainly sensible to the downstream pressure perturbations.

Comparisons between the reference case and control cases with VG devices, for the 30 Hz forced shock oscillation configuration, are carried out on the evolution of the pressure fluctuations, respectively, for their RMS levels (see Fig. 11) and spectra (see Fig. 12, only for the three sensors located in the shock oscillation region and with the VG-C2 device). Concerning the G9 sensor, control by VGs allows to maintain the RMS pressure level at the level measured in the upstream supersonic region (P1 sensor), whereas this level is strongly increased without control. So, the extreme location of the leading shock of the λ-shock structure is moving in the downstream direction due to VGs effects, which leads to a

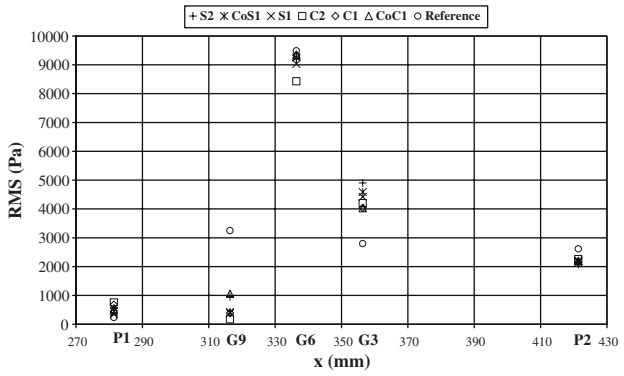

Fig. 11 RMS pressure levels for 30 Hz-forced shock oscillation configuration without control and with VG devices

reduction of the shock oscillation amplitude. The corresponding spectrum for the VG-C2 device (see Fig. 12a) has a lesser broadband level (−25 dB) compared to the reference case one, similar to that of the supersonic region (see Fig. 10a). The presence of weak peaks means that the upstream location of the leading shock is at the limit of the sensor location. Nevertheless, these passive VG devices are less efficient in diminishing the shock displacement than an active control device—flow suction through a perforated plate placed in the interaction region—tested in a previous study for inlet buzz control [10]. Indeed, for a moderate value of the suction mass flow rate (equal to 20 g/s, which means around 1% of the channel mass flow rate), the decrease in shock oscillation amplitude is around 20% (from 30 to 24 mm). The very high RMS pressure level obtained with the G6 sensor is related to the presence of a recirculation bubble at this location, i.e., the rear part of the bump. Then, both spectra have the same behaviour with a 30 Hz fundamental peak and few harmonics almost at the same levels (see Fig. 12b). For the G3 sensor, discrepancies on the RMS pressure level are observed between the VG devices, this location corresponding to the

Fig. 12 Longitudinal evolution of the pressure fluctuations spectra for 30 Hz-forced shock oscillation configuration without control (*left*) and with VG-C2 device (*right*)

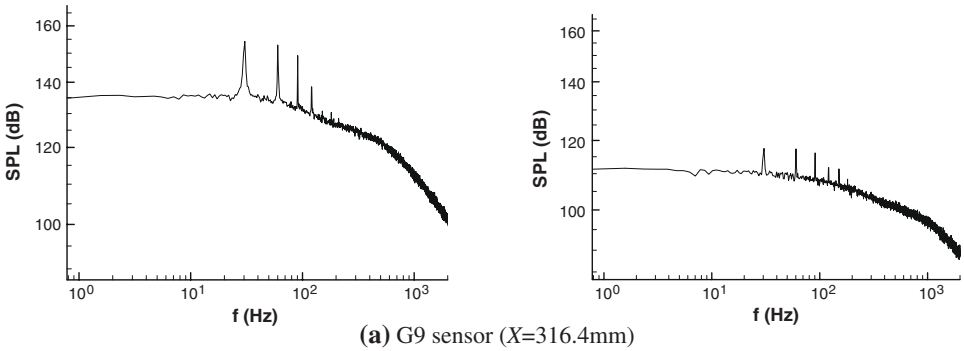

(a) G9 sensor (X=316.4mm)

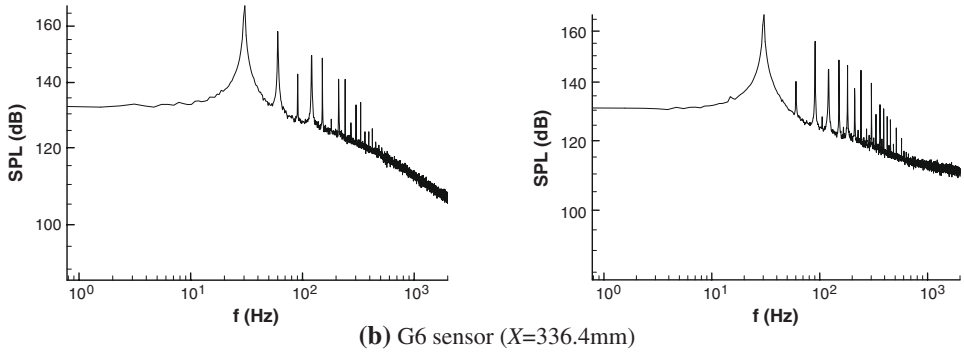

(b) G6 sensor (X=336.4mm)

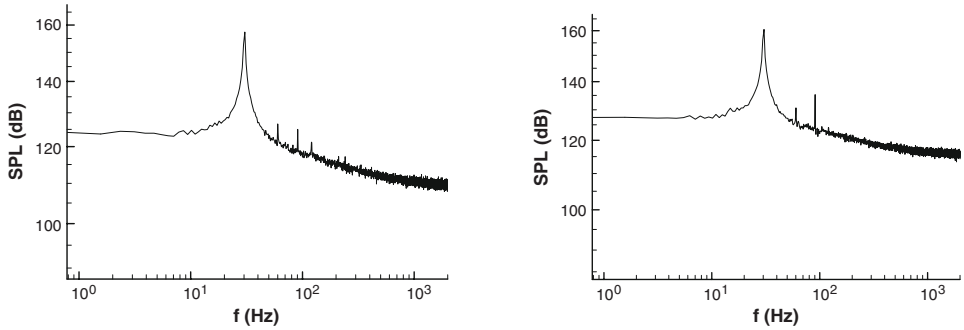

(c) G3 sensor (X=356.4mm)

reattachment flow region. However, this sensor always being located downstream of the leading shock, the spectrum corresponding to the VG-C2 device has an equivalent behaviour to that of the reference case one (see Fig. 12c). The moderate RMS level remaining for the P2 sensor (compared to the upstream residual P1 level) means that the reattached boundary layer has not yet reached a new equilibrium state.

5 Conclusion

The aim of the experimental study was to control by mechanical vortex generator devices the strong interaction between a shock wave and a separated turbulent boundary layer in a transonic channel. Control devices—co-rotating and counter-rotating vane-type vortex generators—were implemented upstream of the shock foot region and tested both on a steady shock wave and on a forced shock oscillation configurations. Continuous and unsteady wall pressure measurements allowed to quantify the effects of vortex generators on the flow separation region and the shock oscillation amplitude. Laser sheet visualizations and oil flow visualizations permitted to track the trajectories of the small-scale streamwise vortices emanating from the vortex generator devices and their interaction with the boundary layer and the shock wave.

The spanwise spacing of vortex generator devices along the channel appeared to be an important parameter to control the flow separation region. When the distance between each device is decreased, the vortices merging is more efficient to reduce the separation. Moreover, their placement upstream of the shock wave is determinant to ensure that vortices have mixed momentum all spanwise long before they reach the separation line, so as to avoid separation cells. The expansion and compression waves generated by the vortex generators have a slight intensity. But in term of drag penalties, the way to reduce the effects of these perturbations should be to impose the height of the vortex generators at a value less than the sonic line of the incoming boundary layer.

Then, vortex generators reduced the amplitude of the forced shock wave oscillation by delaying the upstream displacement of the leading shock. Nevertheless, active control by flow suction through a perforated plate placed in the interaction region was more efficient to diminish the shock displacement.

Further investigations will be focused on the flowfield measurements in the main and spanwise directions by means of particule image velocimetry (PIV) technique, with emphasis near the wall to accurately determine the trajectories of vortices and the extension of the (residual) separation region. Laser sheet visualizations recorded on a high-speed camera will allow to point out the unsteady behaviour of vortices, especially after vortex merging in the interaction region. Control of corner flows will be tested to reduce the three-dimensionality of the flow and to see their impact on the separation benefit given by the vortex generators.

Acknowledgments The research reported here was undertaken as part of the UFAST project (Unsteady effects in shock wave induced separation) funded by the European Union.

References

1. Pearcey, H.H.: Shock induced separation and its prevention by design and boundary layer control. In: Lachmann, G.V. Boundary Layer and Flow Control, vol. 2, pp. 1312–1314. Pergamon, Oxford (1961)
2. Stanewsky, E.: Adaptive wing and flow control technology. Prog. Aero. Sci. **37**, 583–667 (2001)
3. Ashill, P.R., Fulker, J.L., Hackett, K.C.: A review of recent developments in flow control. Aeronaut. J. **109**, 205–232 (2005)
4. Lin, J.C.: Review of research on low-profile vortex generators to control boundary layer separation. Prog. Aero. Sci. **38**, 389–420 (2002)
5. McCormick, D.C.: Shock-boundary layer interaction control with low-profile vortex generators and passive cavity. AIAA Paper 92-0064, 30th AIAA Aerospace Sciences Meeting and Exhibit, Reno, NV (1992)
6. Ashill, P.R., Fulker, J.L., Hackett, K.C.: Research at DERA on sub boundary layer vortex generators (SBVGs). AIAA Paper 2001-0887, 39th AIAA Aerospace Sciences Meeting and Exhibit, Reno, NV (2001)
7. Babinsky, H., Makinson, N.J., Morgan, C.E.: Micro-vortex generator flow control for supersonic engine inlets. AIAA Paper 2007-0521, 45th AIAA Aerospace Sciences Meeting and Exhibit, Reno, NV (2007)
8. Galli, A.: Contrôle de l'oscillation d'une onde de choc en écoulement transsonique de canal. Ph. D. thesis, University of Provence Aix-Marseille I (2005)
9. Délery, J.: Analysis of the separation due to shock wave - turbulent boundary layer interaction in transonic flow. Aero. Res. **6**, 305–320 (1978)
10. Galli, A., Corbel, B., Bur, R.: Control of forced shock-wave oscillations and separated boundary layer interaction. Aero. Sci. Tech. **9**, 653–660 (2005)
11. Sajben, M., Bogar, T.J., Kroutil, J.: Forced oscillation experiments in supercritical diffuser flows. AIAA J. **22**, 465–474 (1984)
12. Salmon, J.T., Bogar, T.J., Sajben, M.: Laser Doppler velocimeter measurements in unsteady, separated, transonic diffuser flows. AIAA J. **21**, 1690–1697 (1983)
13. Ott, P., Bölcs, A., Fransson, T.: Experimental and numerical study of the time-dependent pressure response of a shock-wave oscillating in a nozzle. ASME J. Turbo. **117**, 106–114 (1995)
14. Pauley, W.R., Eaton, J.K.: Experimental study of the development of longitudinal vortex pairs embedded in a turbulent boundary layer. AIAA J. **26**, 816–823 (1988)
15. Godard, G., Stanislas, M.: Control of a decelerating boundary layer. Part 1: Optimization of passive vortex generators. Aero. Sci. Tech. **10**, 181–191 (2006)
16. Coudert, L.: Contrôle par générateurs de tourbillons d'une interaction onde de choc / couche limite avec décollement en écoulement transsonique. Master 2 report of University of Poitiers (2007)
17. Dandois, J., Brunet, V., Molton, P., Abart, J-C., Lepage, A.: Buffet Control by Means of Mechanical and Fluidic Vortex Generators. CEAS/KATnet II Conference, Bremen, Germany (2009)

ANNEXE C - PIV STUDY ON A SHOCK-INDUCED SEPARATION IN A TRANSONIC FLOW

Sartor F., Losfeld G. et Bur, R.

Experiments in Fluids, Vol. 53, No. 3, 2012, pp. 815-827

Exp Fluids
DOI 10.1007/s00348-012-1330-4

RESEARCH ARTICLE

PIV study on a shock-induced separation in a transonic flow

Fulvio Sartor · Gilles Losfeld · Reynald Bur

Received: 23 December 2011 / Revised: 13 April 2012 / Accepted: 21 May 2012

Abstract A transonic interaction between a steady shock wave and a turbulent boundary layer in a Mach 1.4 channel flow is experimentally investigated by means of particle image velocimetry (PIV). In the test section, the lower wall is equipped with a contour profile shaped as a bump allowing flow separation. The transonic interaction, characterized by the existence in the outer flow of a lambda shock pattern, causes the separation of the boundary layer, and a low-speed recirculating bubble is observed downstream of the shock foot. Two-component PIV velocity measurements have been performed using an iterative gradient-based cross-correlation algorithm, providing high-speed and flexible calculations, instead of the classic multi-pass processing with FFT-based cross-correlation. The experiments are performed discussing all the hypotheses linked to the experimental set-up and the technique of investigation such as the two-dimensionality assumption of the flow, the particle response assessment, the seeding system, and the PIV correlation uncertainty. Mean velocity fields are presented for the whole interaction with particular attention for the recirculating bubble downstream of the detachment, especially in the mixing layer zone where the effects of the shear stress are most relevant. Turbulence is discussed in details, the results are compared to previous study, and new results are given for the turbulent production term and the return to isotropy mechanism. Finally, using different camera lens, a zoom in the vicinity of the wall presents mean and turbulent velocity fields for the incoming boundary layer.

F. Sartor (✉) · G. Losfeld · R. Bur
ONERA, 8 rue des Vertugadins, 92190 Meudon, France
e-mail: fulvio.sartor@onera.fr

G. Losfeld
e-mail: reynald.bur@onera.fr

R. Bur
e-mail: reynald.bur@onera.fr

1 Introduction

Shock wave/boundary layer interaction (SWBLI) in transonic aerodynamics has been the subject of several experimental and numerical studies in the past. The interaction of shock waves with boundary layers is a basic fluid dynamics phenomenon that has both fundamental and practical importance. From a concrete standpoint, the interaction can have a significant influence on aircraft or rocket performance and often leads to extremely undesirable effects, such as drag rise, massive flow separation, shock unsteadiness, and high wall heating (Délery and Marvin 1986). From the fundamental point of view, this problem involves the basic structure of a shock interacting with separated flows, which represents one of the simplest occurrences of a strong inviscid–viscous interaction.

SWBLI embodies all of the effects of compressibility, turbulence, and separation that present special challenges for both experimentalists and theoreticians alike. Both external and internal flows are often the subject of shock waves, which interact strongly with turbulent boundary layers. The result is frequently the formation of separation related to the development of large turbulent structures in the separated zones of the flow. The origin of these fluctuations is not totally understood, and several models have been suggested to explain their development (Piponniau et al. 2009), deemed highly correlated to the transonic buffet problem (Crouch et al. 2009).

Many experimental efforts over the last decades have sought to gain a better understanding of the SWBLI problem. However, those studies have generally been

Published online: 12 June 2012

frustrated by the limitations of the experimental techniques used (Dolling 2001). Even though pressure or hot-wire measurements (Smits and Muck 1987) and laser Doppler velocimetry (Délery 1978) have focused on specific aspects in these flows, a whole-field quantitative information is still needed in order to characterize the dynamical aspect of the phenomenon. Furthermore, whereas numerical simulations of these flows have achieved some degree of success, they have been generally hampered by the recognized deficiencies of the available turbulence models (Hadjadj and Dussauge 2009; Knight and Degrez 1998). Recently, direct numerical simulation (Pirozzoli and Grasso 2006; Wu and Martin 2007) and large eddy simulation (Garnier et al. 2002) have been applied to the shock wave/boundary layer problem, but mostly for supersonic configurations without a massive separation of the mean flow.

Particle image velocimetry (PIV) has become an essential tool for flow diagnosis and is therefore widely used in industrial as well as academic situations. However, it has some limitations, such as the time necessary to compute the vector fields from the images, or the spatial resolution linked to the windows interrogation size and the difficulty to characterize flow fields where both high and low values of velocity are present. In that respect, over the last decade, high-speed dual-PIV (Souverein et al. 2009), multi-laser multi-camera systems (Hou et al. 2002), or dense PIV based on GPU's (Champagnat et al. 2011) as FOLKI-PIV[1] have been developed in order to overcome the typical PIV limitations.

Since its invention, the PIV technique has become a tool widely used for incompressible flows investigation. When studying phenomena at high Mach number, the effects of compressibility bring with them technical problems such as seeding, optical access through the wind tunnel windows, or lighting. Thanks to the advances in laser and digital imaging technology, in the last decade, PIV has been applied to a variety of typical compressible flows, ranging from transonic to hypersonic configuration with and without shock wave. According to Hadjadj and Dussauge (2009), the SWBLI problems can be divided into three family: the transonic shock wave–boundary layer separation, the oblique shock impinging turbulent boundary layer, and supersonic flow over a compression ramp. To the authors knowledge, among these three different SWBLI configurations, research has focused on compression ramp (Ganapathisubramani et al. 2007) or the corner flow (Selig at al. 1989) and, even more commonly, on impinging shock wave interaction (Dupont et al. 2006; Hou et al. 2003; van Oudheusden et al. 2011): few PIV studies (Hartmann et al. 2011) have been applied to a transonic interaction with a strong shock wave that causes massive separation of the boundary layer. Even considering LDV investigation (Délery 1978; Muller et al. 2001), a deeper physical understanding is still needed for this particular case that presents the additional disadvantage that, in the same field, a supersonic, a high subsonic, and a low-speed reverse flow zones coexist. From a technical point of view, thanks to the presence of a high turbulence level due to the separation of the boundary layer, further seeding problems arise in addition to the classical complication of the supersonic flow PIV.

The purpose of the present study is thus to investigate by means of PIV the transonic interaction between a strong shock wave and a turbulent boundary layer and the resulting separation of the flow using the capability of the recently developed software FOLKI-PIV (Champagnat et al. 2011). An important effort has been made to discuss all the hypotheses of the study: the two-dimensionality assumption of the flow is justified, thanks to multi-plane PIV inspection, the repeatability of the measurements is assured by an air dryer to exclude any displacement of the shock in different test runs, the seeding system is described, and a particle response assessment is presented to show the fidelity of the tracer for the measurement conditions. The whole mean velocity field is discussed in details, providing a wide analysis on the interaction, the recirculating bubble, and the velocity profiles in the mixing layer. By analyzing the velocity fluctuations, a survey on the statistical properties has been accomplished in order to qualify the turbulent flow field and its anisotropic behavior. Finally, a zoom in the vicinity of the wall shows the main properties of flow, and both mean velocity and turbulent profiles are discussed for a transonic boundary layer upstream of the shock wave.

2 Experimental set-up

2.1 Wind tunnel

The experiments were performed in the S8Ch transonic wind tunnel of the ONERA Meudon center, a continuous open-loop wind tunnel supplied with desiccated atmospheric air. The stagnation conditions were near ambient pressure and temperature: $p_{st} = 0.96 \times 10^5 \pm 300$ Pa and $T_{st} = 300 \pm 10$ K. The associated unit Reynolds number is around $Re = 14 \times 10^6$ m^{-1}, which leads to a value of $Re_\Theta = 3{,}500$ for the incoming boundary layer. A air dryer is placed after the air inlet to control the humidity of the flow: during every test run, the rise in the total temperature was lower than 2 °C degrees, and the dew point is maintained around –50 °C.

The test section has a span of 100 × 120 mm, as shown in Fig. 1. The upper wall is rectilinear, slightly convergent

[1] French acronym for Iterative Lucas-Kanade Optical Flow.

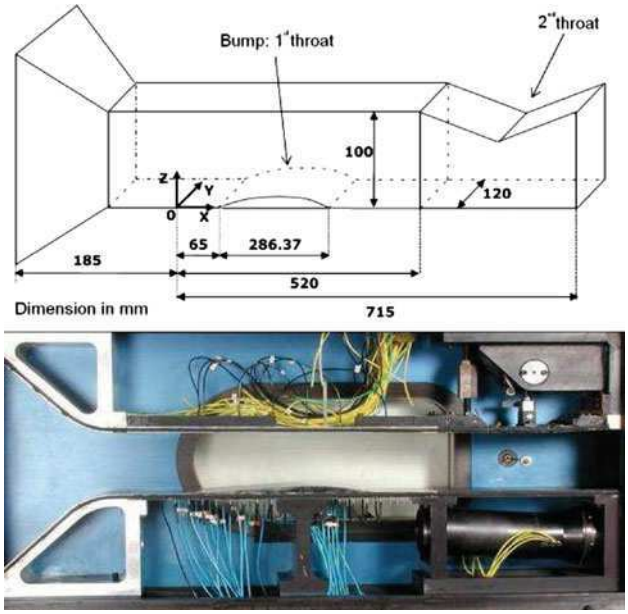

Fig. 1 Schematic diagram and photograph of the test section of the S8Ch wind tunnel

with a slope of 0.55 °, whereas the lower wall is a contoured profile designed to produce a uniform supersonic flow. This half profile or bump is 286.37 mm long and 12 mm tall at the crest and is composed of a first linear part sloped of 4 ° that joins a circular arc up to the trailing edge. A second throat of adjustable cross section is placed at the test section outlet, allowing to produce, by choking effect, a shock wave whose position and intensity can be adjusted in a continuous manner. In the present conditions, the ratio between the two throat sections is 1.12, the corresponding nominal Mach number is equal to 1.4, the shock occurs at the end of the profile, and the detachment of the boundary layer starts already on the bump.

Two-component (2C) LDV measurements in that facilities (Bur et al. 1998, 2009) showed that on the bump, upstream of the shock, the boundary layer is fully turbulent with the following characteristics: physical thickness $\delta = 4$ mm, displacement thickness $\delta^* = 0.46$ mm, momentum thickness $\Theta = 0.25$ mm, and incompressible shape parameter $H_i = 1.6$. Comparing to similar studies (Dupont et al. 2008; Humble et al. 2006; Lapsa and Dham 2011), the thickness of the boundary layer is very small, and consequently, measurements close to the wall are more involved because of optic problems, as will be explained in the next paragraph.

To visualize the flow field and monitor the shock position in the test section, a Schlieren apparatus is used. As any light source disturbs the PIV camera, the Schlieren visualization is employed only to check the initial conditions when the wind tunnel is started. Then, the position of the shock is monitored by the evolution of static pressure through 36 pressure taps on the lower wall. Previous studies (Galli et al. 2005) showed that there is an optimal position of the lambda shock to achieve the maximal size of the recirculation zone, obtained when the tangent of the shock normal to the lower wall is 12.6 mm downstream of the end of the bump. As the present study focuses on the separation of the boundary layer, the shock wave is maintained in that position in order to enhance the recirculating zone.

Downstream of the shock wave, the nominal Mach number is approximately 0.75 in the upper zone, where the shock can be considered as normal, and its value increases up to a sonic value as approaching the triple point described in Sect. 3. The incoming supersonic flow has longitudinal velocity of about 400 m/s, while the recirculation zone with detached flow does not exceed 40 m/s. This huge difference between the two velocity values is one of the most important problem of the PIV analysis: the goal of the study is to characterize the transonic SWBLI with separated flow. In a very close distance inside the field persists a separated zone, whose dynamics depend on a very low velocity field, hence the need of a great sensitivity in a speed range from –30 to 30 m/s, and a supersonic flow, whose dynamics rest on a speed range from 380 to 420 m/s.

2.2 PIV system

All the results presented stem from a 2C PIV investigation: the two velocity components observed are the horizontal along x and the vertical along y. Measurements are thus performed along a plane located in the middle of the wind tunnel test section (see Fig. 2), where the three-dimensional effects due to sidewalls are less pronounced. The test section is supposed to be large enough to justify the neglect of the wall effects studied by Bruce et al. (2011). A multiplanar evaluation was performed to examine the effects non-uniformity in the spanwise direction. The laser sheet plane was displaced few millimeters from the middle of the wind tunnel, and the resulting velocity field for different

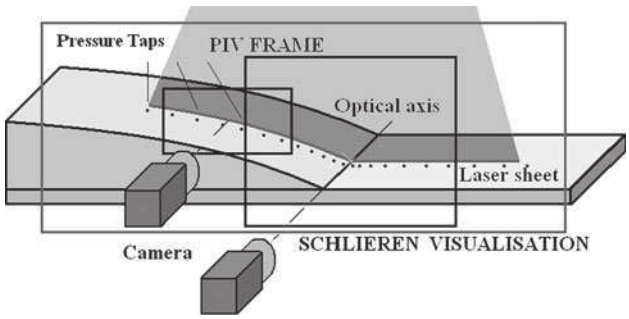

Fig. 2 Scheme of the experimental apparatus

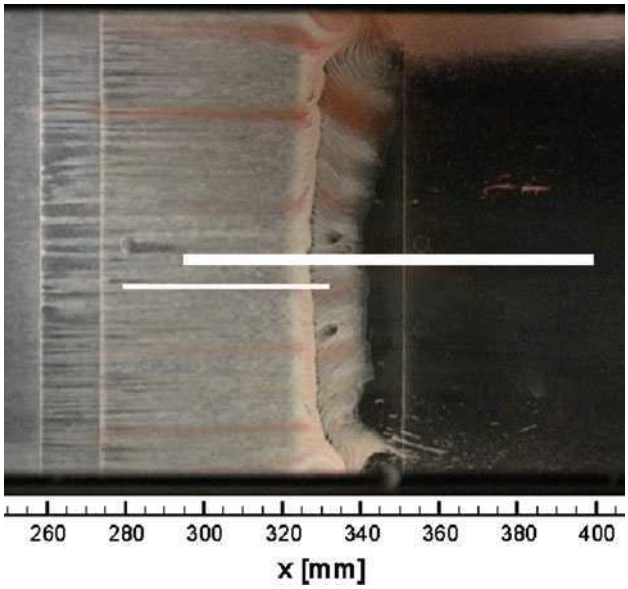

Fig. 3 Oil flow visualizations: upper view, the flow is coming from the left. The *white lines* identify the laser sheet positions for the two investigations

laser positions was compared to each other: since there were no observed significant differences between the resulting fields, one concludes that the two-dimensionality assumption of the flow is correct. The absence of non-uniformity spanwise effect in the center of the wind tunnel can be confirmed also by the oil flow visualization in Fig. 3, which shows that the 3D effects are not negligible only near the sidewalls of the test section.

The light sheets are generated by a double pulse ND:YAG laser, which delivers 150 mJ per pulse. The access for the laser light is provided by a window on the top wall of the wind tunnel, so that the light source direction is toward the decreasing of y: this configuration remains unchanged for both the PIV investigation hereafter referred as global field and boundary layer investigation. Laser pulse separations is 2.5 μs for the global fields and 1.5 μs for the zoom on the boundary layer. 1,000 image pairs are acquired at 5.6 Hz, and less than 4 min was sufficient to record the data. A statistical assessment was performed to verify the convergence of the mean field for the number of samples considered. The camera is equipped with a lens of focal length of 105 mm for the global field and a telecentric lens for the boundary layer; as the CCD is 2,048 × 2,048 pixels, the resulting magnification ratio is around 20 pixels/mm and 37 pixels/mm for the two different cases.

The parameter that mostly affects the results is the size of the interrogation window: this window must be sufficiently large to contain enough particles for the correlation, but the smaller it is, the more detailed are the results, since each interrogation window returns a vector as result. In our case, the resulting field has one vector for each 20 pixels, which means one vector each millimeter: each field presented had at least 100 × 100 vectors. For the zoom on the boundary layer, the interrogation windows is 10 pixels, thus the field presents 200 × 200 vectors, considering the different magnification ratio that yields one vector every 300 μm.

2.3 Seeding

Flow seeding is a critical aspect of PIV in high-speed flows. Moreover, due to the presence of large zone of boundary layer separation with reverse flow, the pollution on the windows disturbs the information on the kinematics of the flow field. The most effective solution for the tracer in the present case is thus the use of liquid particles of Di-Ethyl-Hexyl-Sebacate (DEHS), produced by an atomizer aerosol generator[2], not only because of the ease of use, but also because of the liquid film that gradually settles on the windows is less "opaque" than the deposit of solid particles as the incense or the titanium dioxide, which are commonly used in supersonic PIV.

The DEHS oil injected has a density of about $\rho_p = 900$ kg/m^3 and a typical particle size of about $d_p = 0.5$ μm. The characteristic particle response time is derived from Stokes law for spherical particles as:

$$\tau_p = \frac{\rho_p d_p^2}{18\,\mu} = 0.7\,\mu\text{s} \tag{1}$$

where μ is the dynamic viscosity of the fluid. Considering a characteristic time of the incoming flow given by:

$$\tau_f = \frac{\delta}{U_\infty} \approx 10\,\mu\text{s} \tag{2}$$

the resulting Stokes number is:

$$S_t = \frac{\tau_p}{\tau_f} \approx 0.07 \tag{3}$$

The profile of the Mach number across the shock wave is shown against the local abscissa s in Fig. 4: $s = 0$ indicates the shock position, and s is normal to the shock wave. As a particle passes through the shock, its normal Mach number M_n decreases from M_{n1} to M_{n2}. The experimental data profile (circles in Fig. 4) indicates that there is a lag in the particle spatial response due to the inertial effect of the tracers. The particle relaxation time can also be estimated from an exponential fit of the post-shock particle response: as indicated in Fig. 4, this leads to a particle response time $\tau_p = 0.9$ μs, slightly bigger than the theoretical estimation 1 because of the particle agglomeration (Ragni et al. 2011). According to Samimy and Lele (1991), in a compressible flow the particle slip is fully negligible if the particle Stokes number is $S_t < 0.1$, so both the experimental measurements and the exponential fit

[2] Topas Gmbh ATM 210.

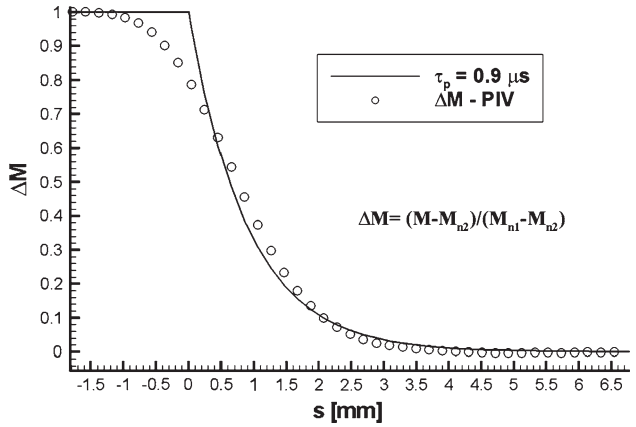

Fig. 4 Particle response to the shock wave: normal Mach number as a function of the local abscissa *s*

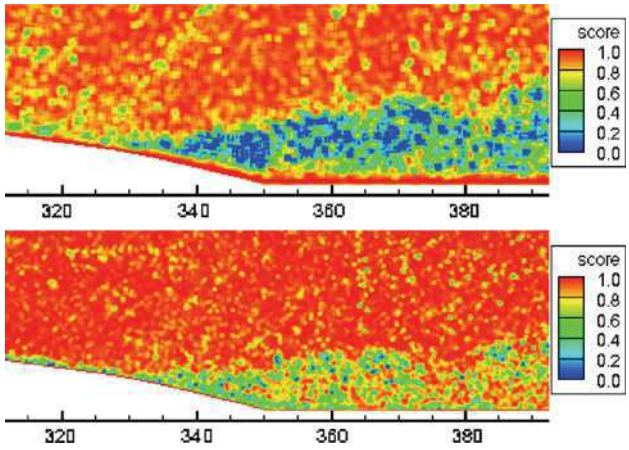

Fig. 5 Score fields for different time between images. *Upper image* the particle displacement is too big, some trace particle have exit the PIV image. *Lower image* sufficient correlation everywhere in the field

referred to our seeding system indicate that the particle response lag is within the limit of a PIV study.

The particle injection system plays an important role in the PIV image quality achieved. Seeding by multi-hole pipes or bent-probe just upstream of the test section was soon discarded for stability and homogeneity reasons. To achieve the most regular seeding without a probe, it is convenient to place the particle generator far upstream of the test chamber, so that the tracers concentration in the flow can homogenize and create a uniform cloud of particles. To do so, the seeding system was placed between the air dryer and the plenum chamber, in a low-speed zone. As the wind tunnel stagnation pressure is less than atmospheric, the particles were naturally sucked into the flow.

2.4 Processing of the PIV images

As previously mentioned, in the present paper, the image processing does not rely on a classical FFT-based PIV software, but on an iterative gradient-based cross-correlation optimization algorithm. The reader is referred to (Champagnat et al. 2011) for a complete explication of the software FOLKI-PIV. The PIV computation is about 50 times faster[3] than a classical FFT-PIV, but the most important quality of FOLKI-PIV is its capability to recognize a particle displacement, regardless if it is of a fraction of pixel or hundreds of pixels. For our wide-range velocity field, this brings an advantage because we can choose a time between the two laser pulses such that the displacement of the particle between two PIV images is considerable both in the subsonic and supersonic part of the field. Imposing a displacement of 30 pixels for each couple of images in supersonic zone yields a movement of at least 2 pixels per image on the separation bubble, where the speeds are about ±20 m/s. Assuming a sensitivity of 0.1 pixels as traditionally done in PIV (Raffel 2007), we can detect dynamics of 1 m/s, which is satisfying even for a subsonic field and more accurate than the other studies in literature (Dupont et al. 2008; Humble et al. 2007).

A limit of the separation time between two laser pulses is the condition that in the two PIV images must be present the same tracer: as described in (Champagnat et al. 2011), to understand whether any particles exit from the laser sheet is sufficient to look at the score field of the results, a number between 0 and 1 that represents the zero-normalized sum squared differences. If the score is more than 0.3, we can trust the result of the SSD calculation. An example of a score field is represented in Fig. 5: if some particles enter or leave the laser sheet because of spanwise velocity in a zone where the three-dimensional effects due to the boundary layer detachment are more pronounced, FOLKI-PIV fails to make the calculation of correlation, and then responds with a low score. Experimental tests have shown that the best compromise between sensitivity and correlation corresponds to a particle displacement of about 30 pixels in the supersonic zone. Finally, the histogram of the velocity field indicates that there is no concentration in integer pixel displacement: the peak locking problem is minimized thanks to a subpixel interpolation and to the scattered light of each particle, which is in the region of 2–6 pixels across on the image.

3 Results

3.1 Mean flow description for the shock-induced separation region

A transonic interaction, if strong enough to cause the separation of the boundary layer, is characterized by the

[3] With images of 2,048 × 2,048 pixels and a TESLA C1060-4 Gb memory, is required less than 1 s per image.

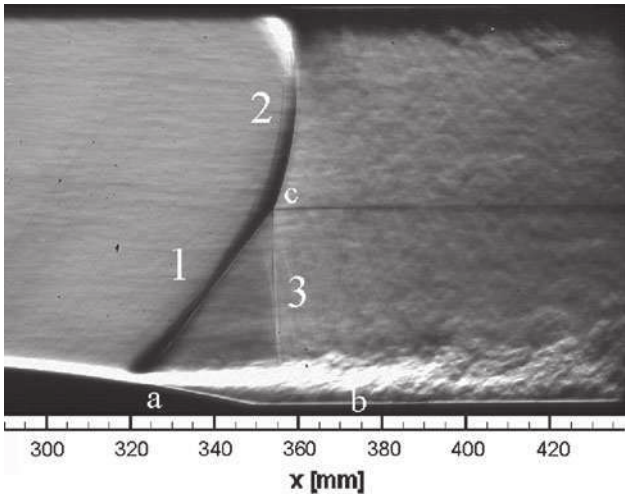

Fig. 6 Schlieren visualization of the lambda shock

existence in the outer flow of a lambda shock pattern, like the one appearing in the Schlieren visualization[4] in Fig. 6: the necessity of this lambda shock pattern comes from the fact that the leading shock (labeled 1 in Fig. 6) is a *weak* oblique shock, whose strength is a function of only the upstream Mach number M_0. Thus, when the leading shock meets the *strong* quasi-normal shock in the far outer field (number 2 in Fig. 6), two states with different pressures and velocity inclinations exist behind these shocks. A third state should be introduced to ensure the compatibility for the two adjacent flows, with the same pressure and velocity orientation of the state downstream of the normal shock. This state is reached through the trailing shock, weaker than the other, which is the strong shock labeled 1, barely visible in the Schlieren picture recording (number 3 in Fig. 6). A locally supersonic zone may exist downstream of this trailing shock. The extent of this zone, called supersonic tongue, depends on the particular conditions for the strong coupling process associated with the deviation towards the wall of the reattaching dissipative layer, and its position in the flow field is determined by the separation bubble. The triple point emerging from the meeting of the shocks cited above (point c in Fig. 6) generates a slip line that surrounds the upper part of the supersonic tongue.

In this PIV investigation, the global field of view is about 100 mm large and is horizontally centered on the downstream end of the bump ($x = 351.4$ mm): in the reference system, the resulting field ranges from $x = 300$ mm to $x = 400$ mm.

Figure 8 shows the structure of the shock as observed in the Schlieren visualization of Fig. 6, and the supersonic tongue (Délery and Marvin 1986) is clearly visible thanks

[4] High-speed camera Phantom V4.1 with a resolution of 752 × 424 pixels and an acquisition speed of 1,000 frames per second, using horizontal knife-edge orientation.

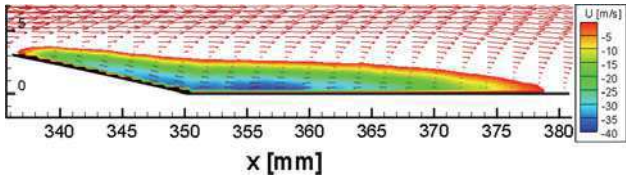

Fig. 7 Mean velocity field, zoom on the separation bubble. Iso-contours correspond to the horizontal velocity component; Velocity vectors are downsampled in horizontal direction, showing 1 every 5 for clarity

to the $Mach = 1$ isocontour line. The separation bubble, characterized by negative values of the longitudinal velocity, is the direct consequence of the boundary layer separation. A zoom in that area, shown in Fig. 7, where there also are velocity vectors, shows the presence of this separation bubble, which starts at the shock foot ($x \simeq 336$ mm) and extends up to $x \simeq 378$ mm. Note that the vectors have been decimated, and the resulting field is more dense. The presence of such a recirculating zone could have been inferred from the Schlieren image in Fig. 6: close to the wall, starting from point a and until point b, there is a zone where the turbulent structures that start from the shock foot are no more visible.

Figure 7 illustrates the complexity of the flow to be measured: while the bulk flow is supersonic, we also aim to characterizing a recirculating bubble that presents limited values of velocity, one order of magnitude smaller than the outer field. With FOLKI-PIV and its multi-resolution framework, this can be done on the same image pair, without the need to acquire additional images focusing on the recirculating bubble. To the authors knowledge, a transonic PIV with an accuracy of 1 m/s (with a subpixel refinement of 0.1 pixel) has never been reported. Unfortunately, in the considered SWBLI, the boundary layer thickness is so small that its dynamics cannot be entirely detected by the spatial resolution of the global field investigation: in this result, we dispose of one vector per millimeter, not sufficient to characterize the boundary layer property. For that reason, the boundary layer investigation has been made with a special camera lens as explained in Sect. 3.3.

Far away from the wall, the velocity field can describe the flow properties in a more accurate way than other studies: PIV results of the current investigation have higher spatial resolution and sensitivity than previous study. Figure 9 presents a comparison with LDV results obtained by Délery (1983). Even if the geometrical configuration is the equivalent for the two studies, the nominal Mach number presents a slight difference between the two investigation. In a transonic interaction over a bump, the Mach number determines the shock position, tightly linked to the separation point of the boundary layer: a small difference in the Mach number can cause a shift of the shock

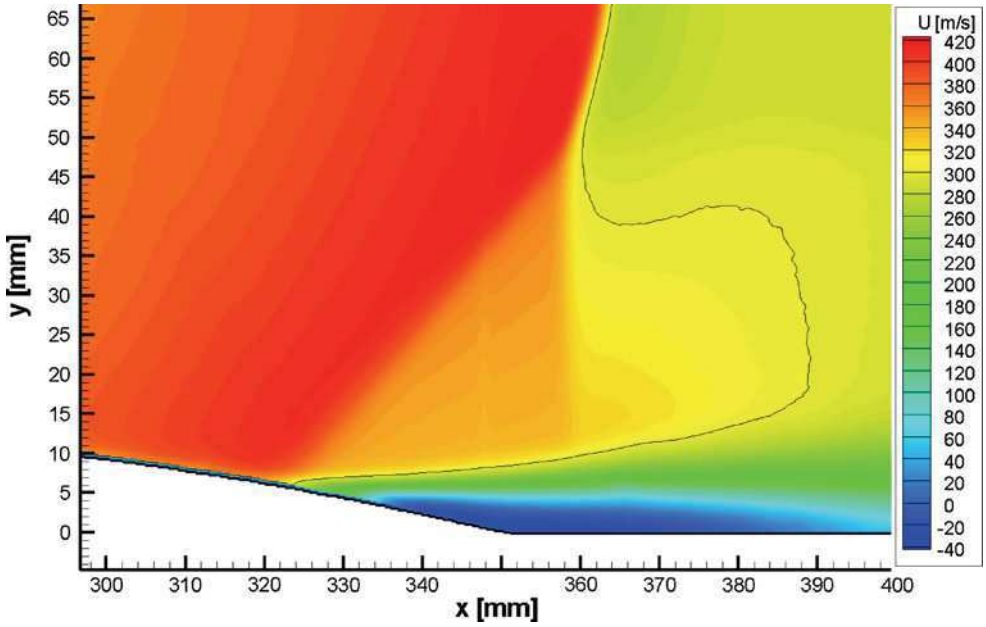

Fig. 8 Iso-contour of the horizontal velocity component for the global field investigation. Mach = 1 *contour line in black*

foot along the bump with consequent displacement of the separating point. Besides that, the center of the recirculating bubble is the same for the two cases, and for that reason, we discuss the profiles inside both of the recirculating bubble.

Following the lines of Piponniau et al. (2009), the profiles presented in Fig. 9 are given by $\frac{u-U_2}{U_1-U_2}$, where U_1 is the external velocity of each profile and U_2 is the highest negative velocity inside the recirculation bubble. This is the only way to proceed that let us compare two cases that, even if with almost the same configuration, present different velocity fields. Note that the velocity U_1 is different for each profile because the recirculating bubble is beneath the lambda shock inside the supersonic tongue, in a zone where the external velocity highly depends on the streamwise position.

Figure 9 describes the velocity distribution along the vertical abscissa, from the separation point to the end of the recirculating zone. The profiles are referred to the external velocity U_1 that, as indicated in the figure, decreases constantly as progressing in the downstream direction. Meanwhile, the y position where this external velocity is completely reached increases, starting from $y = 6$ mm for the profile at $x = 340$ mm and arriving up to $y = 16$ mm when considering the last profile. Regarding the internal velocity U_2, its value decreases as approaching the center of the bubble, situated approximately at $x = 355$ mm and then begins to rise. The positive value of U_2 in the last profile indicates that the end of the recirculating zone is between $x = 380$ mm and $x = 390$ mm. Note that the non-slip condition is not assured for the LDV measurements because of the low spatial resolution, while the dashed line, referred to the PIV measurements, shows in the very first part of the profile a gradual transition from u = 0 to the minimal LDV measured velocity U_2.

All the mean velocity profiles are very similar to profiles observed in subsonic separated flows by Kiya (1983). They exhibit a quasi-linear behavior in the central region, from $y = 4$ mm to $y = 8$ mm, where large convective eddies due to Kelvin–Helmholtz instability are developed and then shed into the downstream flow. The slope of this linear region decreases going downstream from $x = 340$ mm to $x = 390$ mm, indicating an increase of the mixing layer thickness, which can be calculated from

$$\delta_\omega(x) = \frac{U_1(x) - U_2(x)}{\partial u(x)/\partial x} \tag{4}$$

and used to give an appraisal of the spreading rate of the mixing layer, given by $\delta'_\omega = \delta_\omega(x)/x$. The spreading rate is found to be constant and equal to $\delta'_\omega \approx 0.105$. The value is in a good agreement with the spreading rate of the mixing layer proposed by Papamoschou and Roshko (1988) for the compressible turbulent shear layer.

3.2 Turbulence properties evolution in the interaction region

As a result of PIV correlation, FOLKI-PIV gives the r.m.s of the horizontal and vertical velocity fluctuation components. From these quantities, one can derive turbulent kinetic energy and the Reynolds shear stresses, which for our bidimensional study are as follows:

$$k = \frac{1}{2}(\overline{u'^2} + \overline{v'^2}) \quad \text{and} \quad R_{12} = -\overline{u'v'} \tag{5}$$

The evolution of the first quantity, normalized with the characteristic velocity $U_\infty = 300\,\mathrm{m/s}$, is presented in Fig. 10. The field shows that there is a shear layer where

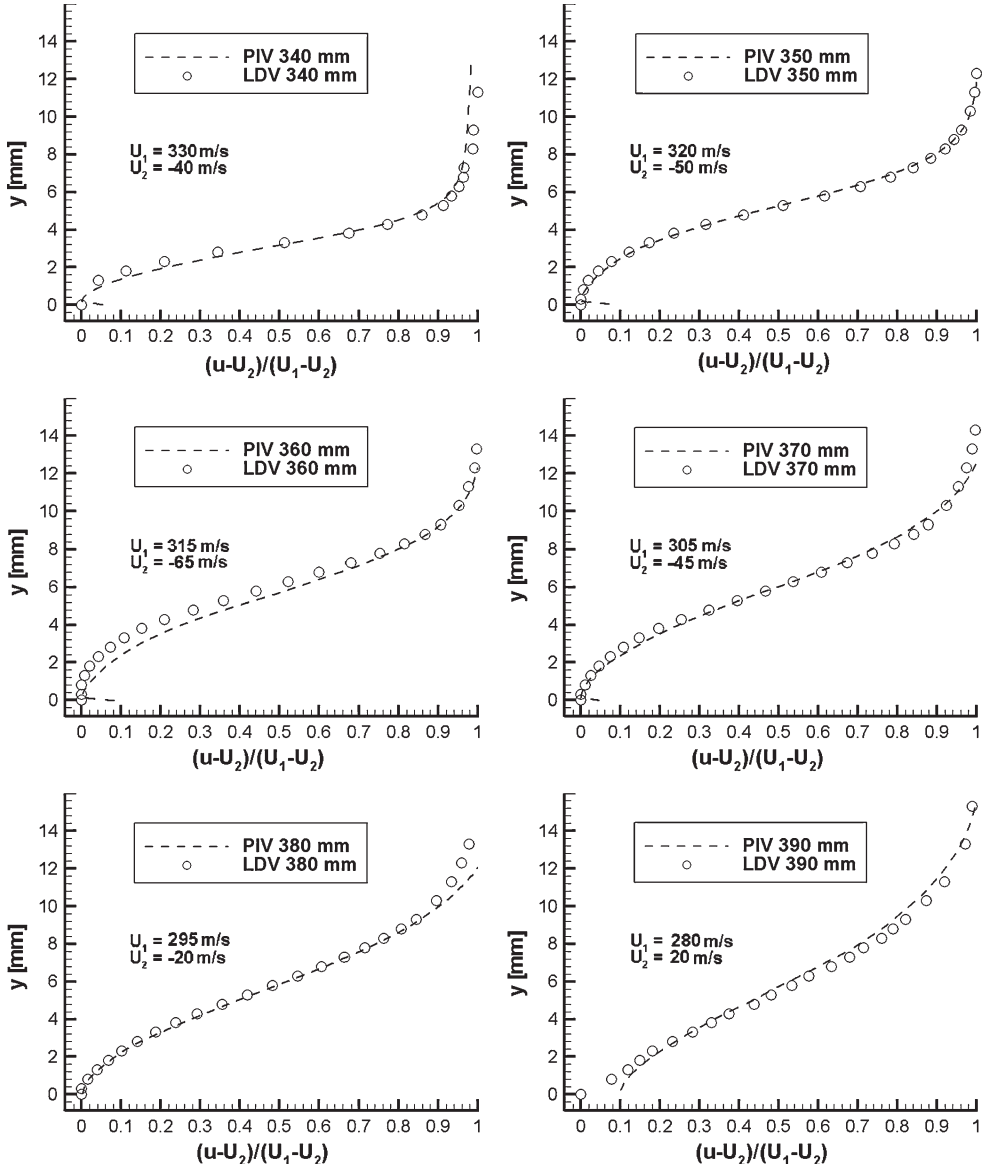

Fig. 9 Comparison of mean velocity profiles inside the recirculating bubble, PIV data of the present study, and LDV (Déler 1983)

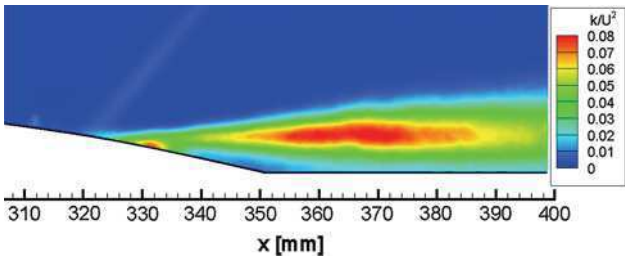

Fig. 10 Evolution of the 2D turbulent kinetic energy k normalized with U_∞^2

turbulence achieves its maximum value that starts from the detachment of the boundary layer and persists above the recirculating zone: this bulk of fluctuation is localized where the medium-scale turbulent structures of Fig. 6 are more evident. Once k has achieved its maximum value, it rapidly decays, suggesting a redistribution of the fluctuation on all the components of velocity. Beneath the shear layer, from $x = 340$ mm to $x = 360$ mm, a low-level turbulence zone indicates that the recirculating bubble presents a uniform recirculation at the end of the bump, characterized by a constant reverse flow.

It is worthwhile to say that the concentration of fluctuation on the bump just downstream of the shock foot (from $x = 330$ mm to $x = 335$ mm) is deemed to be a small blemish: this spot is due to a heap of tracer that forms a drop of oil, which remains between the window and the bump. As the laser flashes on this drop, a random reflection disturbs the PIV images, and the result is a spurious value of the velocity fluctuations. This reflection affects the results only for the interrogation windows that surround the spot.

To confirm the redistribution of fluctuation, it is useful to see separately the two contribution of the energy $u'/U = \overline{u'}/U_\infty$ and $v'/U = \overline{v'}/U_\infty$. Figure 11 shows that the contribution of the longitudinal velocity is the most important (in order to see the relatively small effect of $\overline{v'}$, the scale changes between $\overline{u'}/U_\infty$ and $\overline{v'}/U_\infty$). The streamwise fluctuations are seen to exceed the vertical fluctuation by a factor of 3. This result is in contrast to a plane mixing layer where $\overline{u'}$ is only 30 % higher than $\overline{v'}$, but similar observations are reported by Johnson et al. (1981). This behavior indicates the presence of a high anisotropy turbulence above the separation bubble. However, in the very last part of the field, where the shear layer ends and $\overline{v'}$ achieve its maximal values, the energy is equally divided by the two fluctuation contributions. We can reasonably suppose that the decrease of the turbulent kinetic energy is due to a redistribution of the fluctuation from $\overline{u'}$ to $\overline{v'}$ and also to the unmeasured $\overline{w'}$, suggesting a return to isotropy mechanism.

The anisotropy of the flow plays a significant role in the turbulent production. For an incompressible flow, the production term of the $\overline{u'}$ transport equation is as follows:

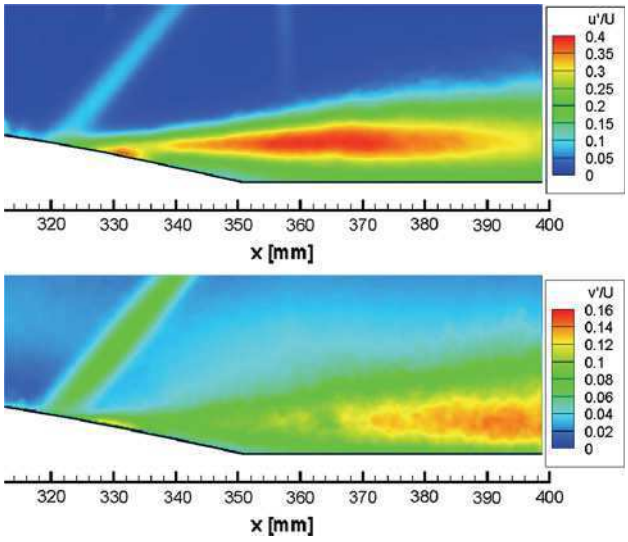

Fig. 11 Evolution of the fluctuation for the normalized longitudinal and vertical velocity components $\overline{u'}/U_\infty$ and $\overline{v'}/U_\infty$)

$$P_u = -2\overline{u'v'}\frac{\partial \overline{u}}{\partial y} - 2\overline{u'^2}\frac{\partial \overline{u}}{\partial x} \tag{6}$$

The results obtained are presented in Fig. 12. For the current transonic interaction, the density presents a variation across the viscous layer of about $\rho_e/\rho_w = 0.85$, deemed to be small enough to neglect the compressibility effect. In the first part of the interaction process, the term involving the streamwise derivative is as large as the term involving the strain rate $\partial u/\partial y$ due to the strong retardation of the whole dissipative flow: P_u is here the sum of two large positive terms. Downstream, the normal stress contribution becomes rapidly negligible. The results are in good agreement with Délery (1983). The contribution of the vertical derivative is linked to the development of the boundary layer: on the wall, we can see upstream the detachment a positive value, and in the reverse flow zone, a negative value. Furthermore, on the wall, downstream of the reattachment point, the production of turbulence begins to rise, suggesting the presence of a redeveloping boundary layer. Far from the wall, both terms in the production are important and achieve their maximal values in the shear layer zone.

The most interesting result is the Reynolds shear stress $-\overline{u'v'}/U_\infty^2$, whose distribution is presented in Fig. 13. For compressible flows, the Reynolds shear stress is given by $-\overline{\rho}\overline{u'v'}$. However, for the transonic interaction under investigation, the change of density across the dissipative layer is small, so that $-\overline{u'v'}/U_\infty^2$ can be considered as a non-dimensional Reynolds shear stress.

The maximum value of the normalized turbulent shear stress is 0.023, in good agreement with the results obtained with LDV measurements (Bur et al. 2006; Délery and Marvin 1986), where the maximal value in a similar configuration (shock in upstream position) was 0.026. Regarding the evolution in the shear layer, we can say that the maximum of the shear stress is downstream of the recirculating zone: as suggested by Ardonceau (1984), the large values of the Reynolds shear stress imply the existence of a large-scale eddies, consistent with the Schlieren visualization of Fig. 6. In comparison to the turbulent kinetic energy, the shear stress grows at a relatively slower

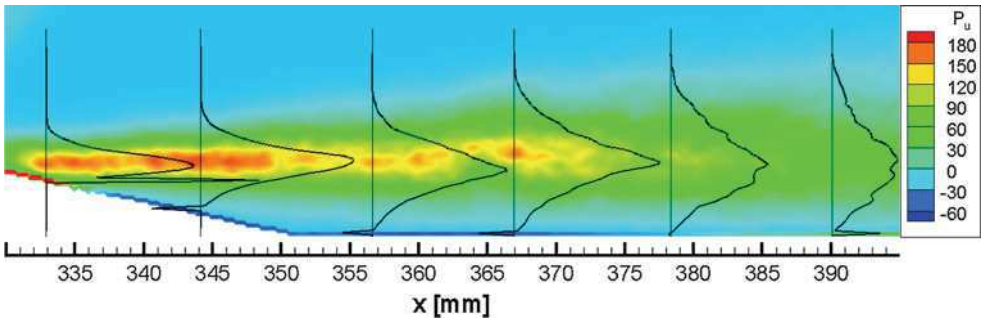

Fig. 12 Evolution of turbulence production term of the $\overline{u'}$ transport equation P_u

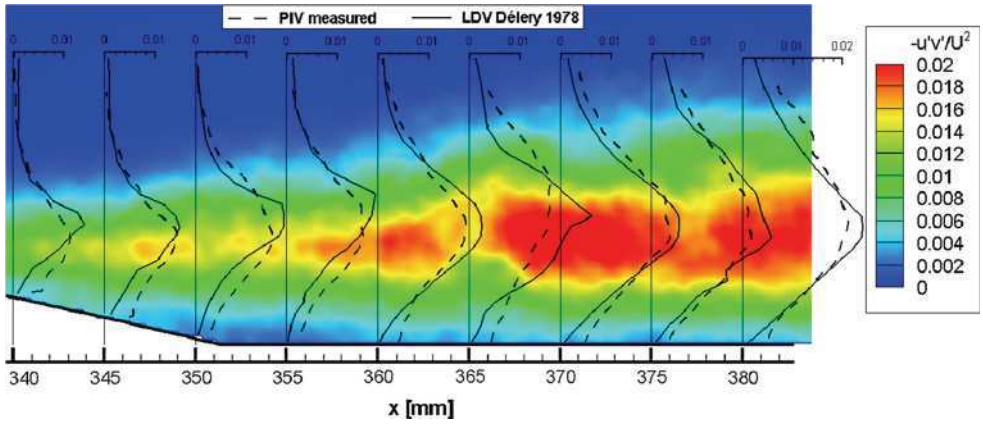

Fig. 13 Evolution of the Reynolds shear stress $-\overline{u'v'}$, normalized with U_∞^2. Flow field and *dashed line* PIV measurements (present study). *Solid line* LDV measurements by Délery (1978)

rate and reaches its maximum value downstream of the point where k culminates. For separated flows, the location of maximum shear stress often coincides with the reattachment point (see Délery 1999), visible in Fig. 7.

The presence of the first branch of the lambda shock is always visible in the turbulent fields, particularly in the shear stress and in the $\overline{v'}$ distributions: an oblique line upstream of the detachment point indicates a significant raise of the fluctuations immediately downstream of the shock wave and roughly parallel to it. These fluctuations highlight the unsteady behavior of the leading shock. In this zone of the flow, as explained by Elsinga et al. (2005), the optical aberration effects introduced by the inhomogeneous refraction index may affect the measurements, as also observed in several other PIV studies (Humble et al. 2007; Mitchell et al. 2011). Besides the oblique line close to the shock, the results obtained for the Reynolds stress are in very good agreement with a similar study, made on the same configuration, by Délery (1978).

3.3 Boundary layer

This section discusses the boundary layer upstream of the shock. The results have been obtained with a particular lens called telecentric, whose property is to filter all the oblique rays not parallel to the optical axis. This property can be exploited to reduce part of the laser reflections on the wall, while the light intensity of each image remains high because of the wide aperture of the objective. The resulting fields cannot be directly compared with other studies on the same configuration, because our PIV data have a much better resolution in the near-wall region than the LDV measurements of (Délery 1978). However, all the profiles presented below are in good agreement with similar supersonic turbulent boundary layer investigations over a bump (Webster et al. 1996) or in shock reflection case (Dupont et al. 2008; Humble et al. 2007).

The main problem of the configuration is that the boundary layer is much thinner than other similar studies. Even if the PIV system is able to measure up to 300 μm from the wall, in terms of normalized distance, this means that the first reachable point is located at $y/\delta = 0.1$. In terms of non-dimensional distance y^+, assuming a friction velocity of $u_\tau \approx 20$ m/s, the first PIV point is at $y^+ = 100$, but a departure of the experimental data from the profile expected from a classical boundary layer profile can be observed starting from $y^+ = 200$. Notwithstanding, the spatial resolution and the wall approach are satisfactory for boundary layer investigation.

Even if with some wall approach limitation, the velocity field can be almost entirely characterized as shown in Fig. 14: the mean longitudinal velocity in the boundary layer upstream of the shock is measured up to the wall, even if the results can be considered rigorously accurate only down to $y/\delta = 0.1$, because of the PIV resolution. Both the mean velocity and the turbulent profiles presented in this section have been extracted at $x = 315$ mm; the mean velocity has been normalized with the external bulk velocity, indicated with U_0, whose value upstream of the shock is about $U_0 = 380$ m/s. To compare turbulence results with the interaction investigation, the velocity fluctuation profiles have been normalized with the same U_∞ used in the previous section.

Figure 15 presents a comparison between the two components of the velocity fluctuation. The variation of these two quantities compares favorably with other studies such as (Dupont et al. 2008) or (Lapsa and Dham 2011) even if in a flat plate configuration, and the turbulence properties attain their free-stream values upstream of the shock wave, which is about 0.02 as depicted in Fig. 11. For the longitudinal velocity fluctuation, the region of high level of turbulence starts near the wall and reaches its maximal values of $U_\infty/10$ in $y/\delta = 0.1$. The near-wall peak described in Fig. 15 cannot be deemed completely resolved because, as mentioned at the beginning of the section, the first measurable point is located in $y/\delta = 0.1$. Nevertheless, we included in the plot a point in $y/\delta = 0.04$ even if it probably stems out of an interpolation

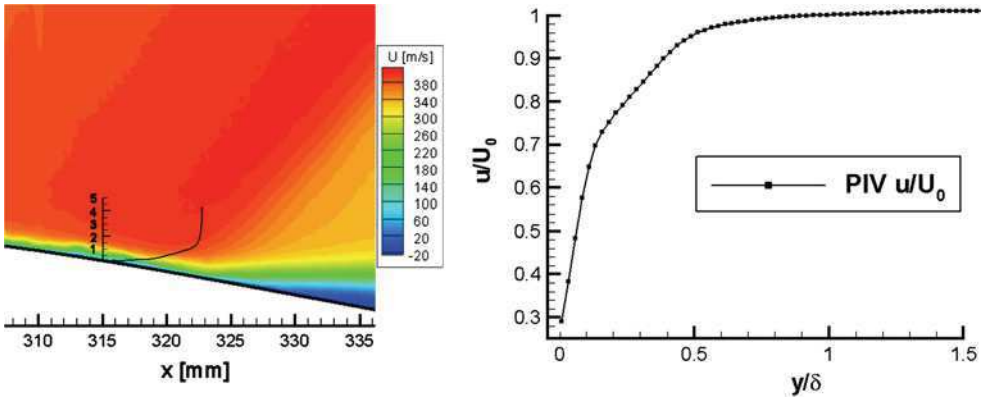

Fig. 14 Mean longitudinal velocity measurement in the boundary layer upstream of the shock: on the *left*, the iso-contour of the mean flow, and on the *right*, a velocity profile referred to the position $x = 315$ mm

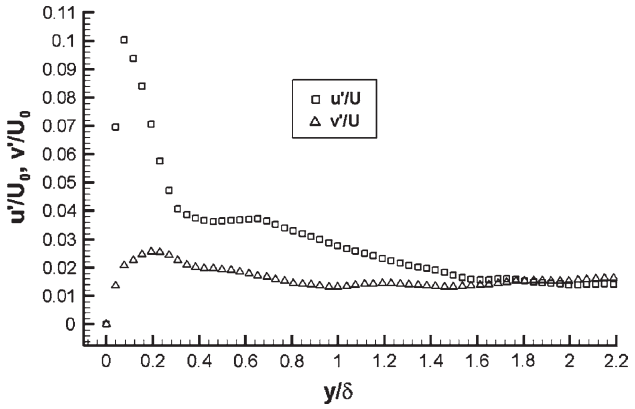

Fig. 15 Velocity fluctuation measurement in the boundary layer upstream of the shock

process between the point $u' = 0$ at the wall and the first completely accurate point in $y/\delta = 0.1$. To the authors knowledge, PIV measurements of a turbulent boundary layer have been reported with more accuracy only by Humble et al. (2006), who disposed of a boundary layer almost 10 times thicker, or more recently by Lapsa and Dham (2011), but in a configuration with a supersonic flow without shock wave.

The near-wall peak extends up to $y/\delta = 0.3$, and then, the velocity fluctuation decreases constantly through the boundary layer. Starting from $y/\delta = 1.7$, the fluctuation attains its free-stream value $u'/U = 0.02$ as mentioned before. A similar behavior can be observed for the vertical component v'/U of the turbulence intensity that if compared to u'/U attains a smaller maximum value of about $\overline{v'}/U_0 = 0.03$ at $y/\delta = 0.2$, in good agreement with the already mentioned similar studies (Dupont et al. 2008; Humble et al. 2007; Webster et al. 1996).

4 Conclusions

The aim of this study was to characterize the shock wave/boundary layer interaction on a bump and the resulting separating flow. Two-component PIV measurements allowed to obtain a full description of the flow field in one single view, providing details on the turbulent velocity field in the interaction region. A multi-planar evaluation in the spanwise direction assured the validity of the two-dimensionality hypothesis, and a particle response assessment validated the accuracy of the seeding system.

The results presented in this paper give a complete description of the effect of a shock-induced separation in a transonic flow over a bump, providing new insight in the SWBLI case of a normal shock. The accuracy of the measurements was validated through a comparison with a similar study on the same configuration where possible, and all the results are in good agreement with similar investigation. The mean velocity field is deemed to be resolved with an accuracy of 1 m/s and a spatial resolution of 1 mm, while thanks to a zoom in the near-wall region, the boundary layer is characterized up to 300 μm from the wall. The bidimensional fluctuating field far from the wall is completely resolved, and the results can be used to validate turbulence closure models.

The boundary layer is shown to be completely developed, and its size increases while approaching the shock due to the curvature of the bump. The main effect of the shock wave is the flow detachment with consequent negative velocity field. The boundary layer recovery starts gradually downstream of the recirculating bubble. Three regions of the flow, supersonic, subsonic, and reverse flow, are completely characterized, and mixing layer is also observed starting from the shock foot. Its spreading rate is calculated thanks to velocity profiles, and the resulting value is in agreement with the theory.

Velocity fluctuation measurements allow a full description of the turbulent behavior of the interaction, showing that initially the flow exhibits strong anisotropy, the streamwise fluctuation exceeding the vertical fluctuation by more than a factor of 3. Turbulent kinetic energy has suggested the position of large-scale eddies in the flow, whose presence was confirmed by the Schlieren

visualization. Furthermore, turbulence measurements have shown that the first part of the interaction process entails a very large turbulence production, which mainly affects the streamwise component. A gradual relaxation through a return to isotropy mechanism is observed far away from the detachment point.

In future work, we envisage to pursue on this configuration with a three-component PIV in order to have access to the spanwise velocity, and we will also consider a time-resolved PIV to investigate on the unsteady behavior of the transonic shock wave/boundary layer interaction with massive separation.

Acknowledgments The authors wish to thank Yves Le Sant and Benjamin Leclaire for their valuable support with FOLKI-PIV software.

References

Ardonceau P (1984) The structure of turbulence in a supersonic shock-wave/boundary-layer interaction. AIAA J 22(9):1254–1262

Bruce P, Burton D, Titchener N, Babinsky H (2011) Corner effect and separation in transonic channel flows. J Fluid Mech 679:247–262

Bur R, Benay R, Galli A, Berthouze P (2006) Experimental and numerical study of forced shock-wave oscillations in a transonic channel. Aerosp Sci Technol 10(4):265–278

Bur R, Coponet D, Carpels Y (2009) Separation control by vortex generator devices in a transonic channel flow. Shock Waves 19(6):521–530

Bur R, Corbel B, Délery J (1998) Study of passive control in a transonic shock wave/boundary-layer interaction. AIAA J 36(3):394–400

Champagnat F, Plyer A, Le Besnerais G, Leclaire B, Davoust S, Le Sant Y (2011) Fast and accurate PIV computation using highly parallel iterative correlation maximization. Exp Fluids 50(3):1–14

Crouch J, Garbaruk A, Magidov D, Travin A (2009) Origin of transonic buffet on aerofoils. J Fluid Mech 628:357–369

Délery J (1978) Analysis of the separation due to shock wave-turbulent boundary layer interaction in transonic flow. La Recherche Aerospatiale pp 305–320

Délery J (1983) Experimental investigation of turbulence properties in transonic shock/boundary-layer interactions. AIAA J 21:180–185

Délery J (1999) Flow physics involved in shock wave/boundary layer interaction control. In: IUTAM symposium on mechanics of passive and active flow control: proceedings of the IUTAM symposium held in Göttingen, Germany, 7–11 September 1998, vol 53. Springer, Netherlands, p 15

Délery J, Marvin J (1986) Shock-wave boundary layer interactions. AGARDograph

Dolling D (2001) Fifty years of shock-wave/boundary-layer interaction research: what next?. AIAA J 39(8):1517–1531

Dupont P, Haddad C, Debiève J (2006) Space and time organization in a shock-induced separated boundary layer. J Fluid Mech 559: 255–278

Dupont P, Piponniau S, Sidoren A, Debiève J (2008) Investigation by particle image velocimetry measurements of oblique shock reflection with separation. AIAA J 46(6):1365–1370

Elsinga G, Van Oudheusden B, Scarano F (2005) Evaluation of aero-optical distortion effects in PIV. Exp Fluids 39(2):246–256

Galli A, Corbel B, Bur R (2005) Control of forced shock-wave oscillations and separated boundary layer interaction. Aerosp Sci Technol 9(8):653–660

Ganapathisubramani B, Clemens N, Dolling D (2007) Effects of upstream boundary layer on the unsteadiness of shock-induced separation. J Fluid Mech 585:369–394

Garnier E, Sagaut P, Deville M (2002) Large eddy simulation of shock/boundary-layer interaction. AIAA J 40(10):1935–1944

Hadjadj A, Dussauge J (2009) Shock wave boundary layer interaction. Shock Waves 19(6):449–452

Hartmann A, Klaas M, Schröder W (2011) Time-resolved stereo PIV measurements of shock–boundary layer interaction on a super-critical airfoil. Exp Fluids 50(3):1–14

Hou Y, Clemens N, Dolling D (2002) Multi-frame PIV imaging of shock/turbulent boundary layer interactions. In: APS meeting abstracts vol. 1

Hou Y, Clemens N, Dolling D (2003) Wide-field PIV study of shock-induced turbulent boundary layer separation. AIAA paper 2003-0441

Humble R, Scarano F, Van Oudheusden B (2006) Experimental study of an incident shock wave/turbulent boundary layer interaction using PIV. AIAA paper 2006-3361

Humble R, Scarano F, Van Oudheusden B (2007) Particle image velocimetry measurements of a shock wave/turbulent boundary layer interaction. Exp Fluids 43(43):173–183

Johnson D, Bachalo W, Owen F (1981) Transonic flow past a symmetrical airfoil at high angle of attack. J Aircr 18(1):7–14

Kiya M, Sasaki K (1983) Structure of a turbulent separation bubble. J Fluid Mech 137:83–113

Knight D, Degrez G (1998) Shock wave boundary layer interactions in high mach number flowsa critical survey of current cfd prediction capabilities. AGARD AR-319 2:1–1

Lapsa A, Dahm W (2011) Stereo particle image velocimetry of nonequilibrium turbulence relaxation in a supersonic boundary layer. Exp Fluids 50(1):89–108

Mitchell D, Honnery D, Soria J (2011) Particle relaxation and its influence on the particle image velocimetry cross-correlation function. Exp Fluids 50(5):1–15

Muller J, Mummler R, Staudacher W (2001) Comparison of some measurement techniques for shock-induced boundary layer separation. Aerosp Sci Technol 5(6):383–395

Papamoschou D, Roshko A (1988) The compressible turbulent shear layer: an experimental study. J Fluid Mech 197(453)

Piponniau S, Dussauge J, Debiève J, Dupont P (2009) A simple model for low-frequency unsteadiness in shock-induced separation. J Fluid Mech 629:87–108

Pirozzoli S, Grasso F (2006) Direct numerical simulation of impinging shock wave/turbulent boundary layer interaction at m = 2.25. Phys Fluids 18:065,113

Raffel M (2007) Particle image velocimetry: a practical guide. Springer, Berlin

Ragni D, Schrijer F, van Oudheusden B, Scarano F (2011) Particle tracer response across shocks measured by PIV. Exp Fluids 50(1):53–64

Samimy M, Lele S (1991) Motion of particles with inertia in a compressible free shear layer. Phys Fluids A 3:1915

Selig MS, Andreopoulos J, Muck KC, Dussauge JP, Smits AJ (1989) Turbulence structure in a shock wave/turbulent boundary-layer interaction. AIAA J 27(7):862–869

Smits A, Muck K (1987) Experimental study of three shock wave/turbulent boundary layer interactions. J Fluid Mech 182:291–314

Souverein L, Van Oudheusden B, Scarano F, Dupont P (2009) Application of a dual-plane particle image velocimetry (dual-PIV) technique for the unsteadiness characterization of a shock wave turbulent boundary layer interaction. Meas Sci Technol 20:1–16

van Oudheusden B, Jöbsis A, Scarano F, Souverein L (2011) Investigation of the unsteadiness of a shock-reflection interaction with time-resolved particle image velocimetry. Shock Waves 21:1–13

Webster D, DeGraaff D, Eaton J (1996) Turbulence characteristics of a boundary layer over a two-dimensional bump. J Fluid Mech 320:53–70

Wu M, Martin M (2007) Direct numerical simulation of supersonic turbulent boundary layer over a compression ramp. AIAA J 45(4):879–889

ANNEXE D - UNSTEADINESS IN TRANSONIC SHOCK-WAVE / BOUNDARY-LAYER INTERACTIONS: EXPERIMENTAL INVESTIGATION AND GLOBAL STABILITY ANALYSIS

Sartor F., Mettot C., Bur R. et Sipp D.

Journal of Fluid Mechanics, Vol. 781, 2015, pp. 550-577

J. Fluid Mech. (2015), *vol.* 781, *pp.* 550–577. © Cambridge University Press 2015
doi:10.1017/jfm.2015.510

Unsteadiness in transonic shock-wave/boundary-layer interactions: experimental investigation and global stability analysis

F. Sartor[1,†], C. Mettot[1], R. Bur[1] and D. Sipp[1]

[1]ONERA/DAFE, 8 rue des Vertugadins, 92190 Meudon, France

(Received 4 January 2015; revised 15 June 2015; accepted 26 August 2015;
first published online 24 September 2015)

A transonic interaction between a shock wave and a turbulent boundary layer is experimentally and theoretically investigated. The configuration is a transonic channel flow over a bump, where a shock wave causes the separation of the boundary layer in the form of a recirculating bubble downstream of the shock foot. Different experimental techniques allow for the identification of the main unsteadiness features. As recognised in similar shock-wave/boundary-layer interactions, the flow field exhibits two distinct characteristic frequencies, whose origins are still controversial: a low-frequency motion which primarily affects the shock wave; and medium-frequency perturbations localised in the shear layer. A Fourier analysis of a series of Schlieren snapshots is performed to precisely characterise the structure of the perturbations at low- and medium-frequencies. Then, the Reynolds-averaged Navier–Stokes (RANS) equations closed with a Spalart–Allmaras turbulence model are solved to obtain a mean flow, which favourably compares with the experimental results. A global stability analysis based on the linearization of the full RANS equations is then performed. The eigenvalues of the Jacobian operator are all damped, indicating that the interaction dynamic cannot be explained by the existence of unstable global modes. The input/output behaviour of the flow is then analysed by performing a singular-value decomposition of the Resolvent operator; pseudo-resonances of the flow may be identified and optimal forcings/responses determined as a function of frequency. It is found that the flow strongly amplifies both medium-frequency perturbations, generating fluctuations in the mixing layer, and low-frequency perturbations, affecting the shock wave. The structure of the optimal perturbations and the preferred frequencies agree with the experimental observations.

Key words: absolute/convective instability, compressible flows, shock waves

1. Introduction

Shock-wave/boundary-layer interaction (SWBLI) has been the subject of many studies during the last 60 years (Dolling 2001). Three configurations are commonly studied: the case of a compression ramp; the oblique shock impinging on a flat-plate boundary layer; and the normal shock on a wall (or profile). The latter configuration,

† Email address for correspondence: fulvio.sartor@onera.fr

which is the focus of the current study, is common in air intakes, nozzle exits or in transonic flow over aerofoils.

Regardless of the configuration, many experimental and numerical studies have shown the coexistence of two distinct characteristic frequencies: shock motions involve low frequencies, while the mixing layer downstream of the separation exhibits unsteadiness whose frequencies are higher than those observed in the shock motions, but are still below the energetic scales of incoming turbulence. Inside the recirculation bubble both motions are at play. Turbulent boundary layer fluctuations are referred to as high-frequency unsteadiness.

As commonly done in SWBLI (Erengil & Dolling 1991*b*), one can introduce a dimensionless frequency (or Strouhal number) defined as $St_L = fL_{int}/U_e$ where U_e is the external velocity and L_{int} is the interaction length scale. Using this scaling, Dussauge, Dupont & Debiève (2006) have shown that a value of $St_L = 0.02$–0.05 characterises the shock motions in several configurations. Concerning medium-frequency motions in the mixing layer, typical values spanning $St_L = 0.1$ to $St_L = 0.5$ are common for shock-induced separations. Those motions have been associated to Kelvin–Helmholtz instabilities, which can generate a vortex shedding phenomenon.

The origin of low-frequency motions affecting shock waves is controversial. One of the first answers was suggested by Plotkin (1975), who developed a mathematical model where the shock foot is affected by the passage of turbulent eddies, while the 'stability' of the mean flow tends to restore the shock to its original position. The hypothesis of shock motions caused by organised structures in the incoming flow has been assessed by several experimental investigations: Andreopoulos & Muck (1987) found that the frequency of the shock unsteadiness is of the same order as the bursting frequency of the upstream boundary layer. Subsequently, Erengil & Dolling (1991*a*) and Dolling & Erengil (1991) found correlations between pressure fluctuations in the upstream boundary layer and the shock velocity, but in a more recent study Beresh, Clemens & Dolling (2002) suggest that a thickening/thinning boundary layer is not the cause of the shock unsteadiness, and that shock motions are inherited from eddies in the incoming flow.

While the shock is undoubtedly affected by the passage of low- or high-speed perturbations, upstream events might be only one of several causes of shock unsteadiness. To prove it, Touber & Sandham (2009) performed large-eddy simulations (LES) in a shock-reflection configuration, where special care was devoted to prevent the development of coherent structures in the incoming flow. Low-frequency shock motions could still be observed. Dupont, Haddad & Debiève (2006) also found very weak coherence between the pressure fluctuations in the upstream boundary layer and those at the shock foot. On the contrary, fluctuations at the shock were strongly correlated with the separated zone. According to those studies, low-frequency oscillations are not caused by incoming turbulent eddies, but by the coupling between the dynamics of the separated zone and the shock, either through global instability of the separation bubble, or through some mechanism of self-sustainment.

The two theories described above, even if in disagreement on the location, support the idea that the instability is driven by a unique source. However, a plausible model is that the interaction responds as a dynamical system which is forced by external disturbances (Clemens & Narayanaswamy 2014). In this respect, Touber & Sandham (2011) proposed an original derivation of the Plotkin (1975) equation and stated that the low-frequency unsteadiness was related to a fundamental property of the shock wave. The model combines numerical evidence and analytical theory to prove that the coupling between the shock and the boundary layer is mathematically equivalent to a

first-order low-pass filter: low-frequency unsteadiness is not caused by a forcing, either from upstream or downstream of the shock, but is an intrinsic property of the global system.

Linear stability analysis has become a tool commonly used in fluid dynamics, which can often help to understand flow unsteadiness (Sipp *et al.* 2010; Theofilis 2011). According to Huerre (2000), occurrences of unsteadiness can be classified into two main categories: the flow can behave as an oscillator, with an absolute instability imposing its own dynamics, or as a noise-amplifier, if the system filters and amplifies existing environmental noise. In the first case, a global-mode decomposition has the ability to identify the mechanism responsible for the self-sustained unsteadiness. Otherwise the unsteadiness is characterised by a broadband spectrum and requires an external forcing to persist. The flow does not exhibit any unstable global mode and the linearised Navier–Stokes operator acts as a linear filter of the upstream disturbance environment. In such cases a singular-value decomposition of the Navier–Stokes or the resolvent operators highlights optimal growth or pseudo-resonance phenomena (Trefethen *et al.* 1993; Schmid & Henningson 2001). The connection between transient growth and convective instability has been discussed by Cossu & Chomaz (1997) and numerous studies have successfully applied these methods to different configurations (Ehrenstein & Gallaire 2005; Abdessemed *et al.* 2009; Alizard, Cherubini & Robinet 2009; Brandt *et al.* 2011).

In SWBLI, only few studies have tried to answer the question of the origins of the unsteadiness through stability analyses. In a laminar interaction, Robinet (2007) found an unstable global mode. However, the mode was three-dimensional and non-oscillatory and cannot therefore account for the low-frequency shock oscillations. In a transonic flow over a profile, Crouch *et al.* (2009) and Sartor, Mettot & Sipp (2015) showed that an unstable global mode appears at a critical value of the angle of attack (or Mach number), above which the shock starts to oscillate. Also, it was found that the oscillation frequency accurately matches the global mode frequency. This picture is similar to the case of vortex shedding in a cylinder wake (Jackson 1987) and may be described as a Hopf bifurcation. In a shock impinging on a turbulent boundary layer configuration, Touber & Sandham (2009) performed a global-mode decomposition of a mean flow obtained by time- and span-averaging of a three-dimensional LES computation. The most unstable global mode was stationary, so the result cannot be considered as relevant to explain flow unsteadiness. Following a similar approach, Pirozzoli *et al.* (2010) confirmed the presence of a non-oscillatory exponentially growing mode, but documented also the presence of slightly damped oscillatory eigenvalues. Those modes, even if stable, display frequencies comparable to the unsteadiness observed in full LES.

These partial results indicate that the interaction dynamics could be captured by a linear stability analysis. Yet an eigenvalue decomposition may not be the correct approach. If the interaction behaves as a noise amplifier, then the unsteady behaviour of the flow could be better characterised by an input/output analysis focusing on the receptivity of the flow to external forcing. In separation bubbles, the existence of optimal growth phenomena has been proven by Marquet *et al.* (2008) and Blackburn, Barkley & Sherwin (2008), who described the flow dynamics by determining the optimal initial perturbations which maximise the energy gain over a given time horizon. In configurations where there is a strong frequency-selection process, working in the frequency instead of the temporal domain has a deeper physical meaning (Farrell & Ioannou 1996). Hence, following Alizard *et al.* (2009) and Cerqueira & Sipp (2014), the existence of pseudo-resonances in a given frequency

range may explain the existence of a peak in the frequency spectrum of an unsteady flow. A singular-value decomposition of the resolvent operator may be able to identify these pseudo-resonances. The outcome of such an analysis yields for all frequencies an optimal gain, an optimal forcing and an optimal response. The peaks of the optimal gain curve may then correspond to the preferred frequencies of the flow, the structure of the optimal response to the structure of the flow unsteadiness, while the spatial structure of the optimal forcing may indicate where upstream noise or turbulence could optimally trigger this perturbation. This approach has already been used to describe the most amplified modes in a channel flow configuration (Jovanovic & Bamieh 2005), in a turbulent pipe flow (McKeon & Sharma 2010) and in a Blasius boundary layer (Brandt *et al.* 2011).

Linear stability analyses are rigorous and widely used in the case of laminar, transitional flows. Extension to turbulent flows is not straightforward (Mettot, Sipp & Bézard 2014*b*). In the case of turbulent flows for which the scale decoupling assumption holds (Rodi 1997; Iaccarino *et al.* 2003; Lawson & Barakos 2011), the dynamics of the large scales of the flow may be captured using unsteady Reynolds-averaged Navier–Stokes (RANS) equations. The impact of the small scale dynamics on the large ones is accounted for by a turbulence model, which results in an additional viscosity (eddy viscosity). Stability analyses involving the linearization of the full RANS equations have already successfully been performed in the case of transonic flow over a profile (Crouch *et al.* 2009; Sartor *et al.* 2015) or open cavity flow (Mettot, Renac & Sipp 2014*a*). Both configurations exhibit well-defined peaks in the frequency spectrum linked to the existence of a globally unstable mode. In the present article, we will follow this line of thought and assume that the above-mentioned low- and medium-frequencies of the SWBLI are captured by time integration, while the high-frequency motions are taken into account by the turbulence model.

In this work, we propose to characterise the unsteadiness of the well-documented transonic SWBLI over the Délery bump (Délery 1978; Bur *et al.* 2006). We will compare experimental measurements to linear stability analyses. First (§ 2), the frequency selection process is highlighted using wall-pressure and skin-friction measurements. Then, Fourier-mode decompositions of Schlieren photography reveal the spatial location of low- and medium-frequency unsteadiness, whilst cross-correlation maps illustrate their spatial structures. Second (§ 3), we will perform linear stability analyses of a mean-flow obtained by a RANS approach. After a brief presentation of the stability approaches and of the discretisation choices, we will discuss the results of the global-mode decomposition – the eigenvalues of the full linearised RANS equations – and those of the singular-value decomposition of the resolvent. We will assess the ability of stability both approaches to predict the flow unsteadiness observed experimentally.

2. Experimental investigation

The experiments were conducted in the S8Ch transonic wind tunnel of the ONERA Meudon centre, a continuous open-loop facility supplied with desiccated atmospheric air. Total pressure and temperature were near ambient conditions: $p_{st} = 0.96 \times 10^5 \pm 300$ Pa and $T_{st} = 300 \pm 10$ K. The unit Reynolds number is around $Re = 14 \times 10^6$ m^{-1}, which leads to a value of $Re_\Theta = 3500$ for the incoming boundary layer. An air dryer is placed after the air inlet to control the flow humidity: during every test, the temperature rise was lower than 2 °C, and the dew point is maintained around −50 °C.

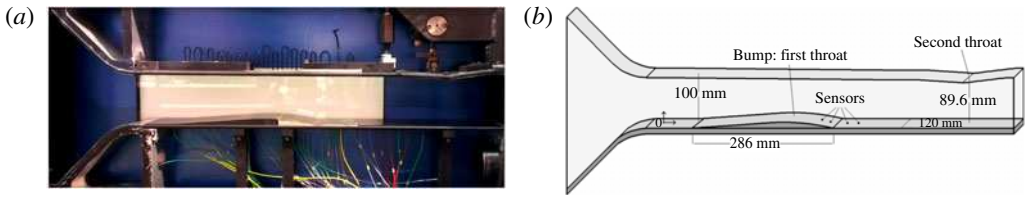

FIGURE 1. (Colour online) The transonic S8Ch wind tunnel in the ONERA Meudon centre. (*a*) Photo of the test section. (*b*) Schematic diagram.

The test section (figure 1) has a span of 100×120 mm and its lower wall is a profile designed to produce a uniform supersonic flow. A second throat of adjustable cross section is placed at the outlet and causes by choking effect a shock wave whose position and intensity can be adjusted in a continuous manner. The ratio between the two sections is 1.12, and the shock occurs at Mach number $Ma = 1.4$ outside the interaction region.

Two-component laser Doppler velocimetry (LDV) measurements performed in the same configuration and facility (Bur, Corbel & Délery 1998; Bur, Coponet & Carpels 2009) have shown that upstream of the shock, the boundary layer on the bump is fully turbulent with a physical thickness $\delta = 4$ mm and a momentum thickness $\Theta = 0.25$ mm. The shock position is monitored by the evolution of static pressure through 36 pressure taps on the lower wall (see figure 12*b*). The mean velocity field has been analysed by Sartor, Losfeld & Bur (2012), who performed a particle image velocimetry (PIV) investigation on the same configuration. Downstream of the shock, the nominal Mach number is approximately $Ma = 0.75$ in the upper zone, and its value increases up to $Ma = 0.95$ on approaching the triple point where the two shock legs merge together, as shown in figure 5. The second throat produces a further supersonic zone which acts like a filter to the existing downstream noise coming from the wind-tunnel engines. A Schlieren apparatus is used to visualise the flow and monitor the shock position.

2.1. *Unsteadiness at the wall*

Low- and medium-frequency fluctuations have been investigated through sensors placed on the lower wall (figure 2). Both Kulite and hot-film sensors are employed, giving access to pressure and skin-friction fluctuations, respectively. The output was amplified and digitised at a sampling frequency of 100 kHz, then Fourier analysis has been performed using 50 % overlap and a Hanning window function, on blocks of 32 768 samples each. This yields, for every spectrum and for both measurement techniques, a frequency resolution of $f = 3$ Hz. The unsteadiness being not very energetic, 500 blocks were recorded for averaging the spectra and obtaining smooth results.

2.1.1. *Pressure fluctuations*

Pressure fluctuations are investigated through high-frequency response pressure transducers (Kulite series XCQ-093-15A, XCS-093-15D and XCS-093-5D) following the work of Dupont *et al.* (2006). As displayed in figure 2, all the sensors were located on the lower wall: one at the shock foot ($x = 315$ mm), one inside the recirculating bubble on the bump ($x = 335$ mm), one on the reattachment point ($x = 395$ mm) and two next to it, respectively at $x = 390$ mm and $x = 400$ mm.

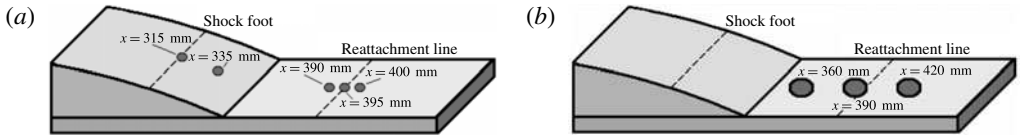

FIGURE 2. Sensors position on the bump for wall-pressure and skin-friction measurement. (*a*) Kulite sensors: unsteady pressure; (*b*) hot-film: skin-friction measurements.

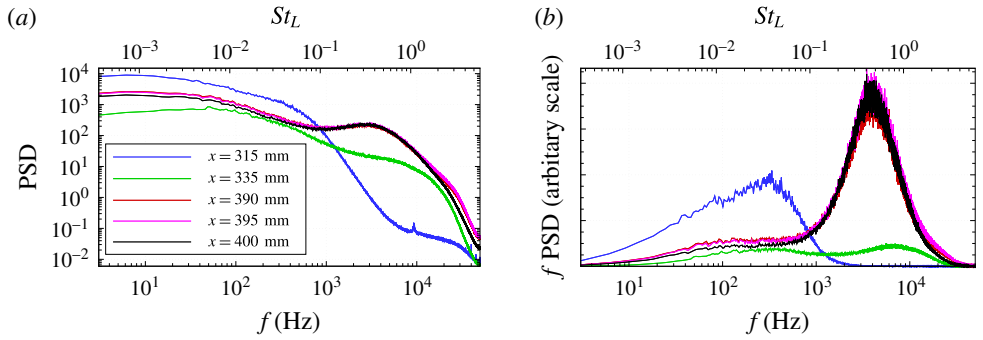

FIGURE 3. (Colour online) Wall-pressure fluctuations on the centreline of the test section. (*a*) Power spectral density; (*b*) premultiplied spectrum.

As shown in figure 3(*a*), the unsteadiness is broadband, without a single predominant peak. All sensors display high power spectral density (PSD) in the low-frequency range, regardless of their location. Then, depending on the distance from the shock-foot, the spectra can present a medium-frequency bump, with a PSD one order of magnitude lower than the one in the low-frequency zone. The high-frequency content due to the turbulent structures in the boundary layer probably occurs at frequencies higher than 50 kHz, not measured because of the bandwidth of the sensors (around 20 kHz).

Figure 3(*b*) displays the weighted PSD, where the product between the PSD and the frequency f is shown as a function of the frequency logarithm. This representation, called premultiplied spectrum, gives access to the frequency content of the energy fluctuations. The area below this curve corresponds to the total fluctuating energy. The sensor at the shock foot reveals that most of the energy is in the low-frequency range, whilst the one in the separated zone indicate that medium-frequency motions are the most energetic.

The top horizontal axis of all figures presents the Strouhal number, obtained with a characteristic length $L = 35$ mm, corresponding to the distance between the separation point and the impingement location of the lambda shock on the wall, and a velocity of $U = 300$ m s^{-1}, corresponding to the flow speed above the recirculation bubble. This scaling yields, for the sensor placed at the shock foot, a maximum $f \cdot \mathrm{PSD}$ around 0.04, which corresponds to a frequency of 300 Hz.

The line corresponding to $x = 335$ mm in figure 3 illustrates that the spectrum of a pressure transducer placed close to the shock and after separation exhibits the low-frequency unsteadiness due to the shock, but also the medium-frequency due to the mixing layer. This indicates that the sensor was in an intermediary zone midway between the two phenomena. The last three sensors, placed close to the end of the

separation bubble, display a very similar spectrum, indicating that pressure fluctuations inside the recirculation zone propagate downstream without changing their frequency content.

The most energetic perturbations in this zone are around 4000 Hz ($St_L = 0.5$). The scale in the premultiplied spectrum of figure 3(*b*) is arbitrary, but the whole spectrum is known up to a multiplicative constant, which is the same for all frequencies: the fact that the peak in the medium-frequency motions is more energetic than the low-frequency one suggests that shock motions contribute less to the total amount of unsteadiness. However, even if less energetic, low-frequency motions are present in the whole interaction, as indicated by figure 3(*a*), where the low-frequency spectral density is high for all the sensors. Thus, even if the weighted PSD in figure 3(*b*) displays a peak in the low-frequency range only at the shock foot, one can find low-frequency fluctuations also in the separated zone. On the contrary, the PSD distribution at the separation point reveals that the shock foot is only affected by low-frequency motions, with a maximum located at the zero-frequency. The frequency distribution is close to a low-pass filter, with a cutoff frequency around $f = 300$–400 Hz, which corresponds to the peak of the weighted PSD in figure 3(*b*).

2.1.2. *Skin-friction fluctuations*

The purpose of this section is to present frequency spectra of skin-friction fluctuations. We used hot-film sensors, based on a thin metal film deposited on an electrically insulating substrate. Three sensors were located after the end of the bump (figure 2): one inside the recirculating bubble ($x = 360$ mm), one around the end of the separated region ($x = 390$ mm) and one downstream of it ($x = 420$ mm).

The sensors (glue-on probe model 55-R47) consist of a 0.1×0.9 mm nickel film deposited on a 0.05 mm thick polyamide foil carrying a 0.5 μm quartz coating, and were operated with a constant temperature circuit (model DISA 55M10). The signals were amplified, digitised and processed as previously described. Figure 4 presents the classic and weighted spectra: in all cases the spectrum displays a high level of PSD in the low-frequency region, and a bump at medium-frequencies. In the weighted PSD, the bump is represented by a broadband peak centred around $St_L = 0.03$, at slightly smaller frequency than in the wall-pressure fluctuations.

When a sensor is placed inside the recirculation zone and close to the shock foot (solid line corresponding to $x = 360$ mm in figure 4) both low- and medium-frequency motions are clearly visible: the premultiplied spectrum presents a bump in the low-frequency range whose energy content is analogous to the one of the medium-frequency bump. This low-frequency content is still visible when the sensor is at the end of the recirculation zone ($x = 390$ mm), and disappears completely for the hot-film sensor in the most downstream position ($x = 420$ mm). The peak corresponding to $f = 50$ Hz identified in all curves of figure 4 is a consequence of the commercial electric power distribution system and is not linked to any physical phenomenon.

The frequency content of the low-frequency fluctuations seems however not the same when analysed with hot-films or with unsteady pressure sensors: the weighted PSD presents a maximum value at $f = 70$–100 Hz when computed with hot-films signals, whilst the peak was around $f = 300$–400 Hz for the Kulite sensors. We do not have a clear explanation of this discrepancy, except the fact that the two sensors have different spatial integration because of their size (the hot-film surface area is greater than those of a Kulite). Note however that if we compare hot-film and pressure curves obtained at the same location (here at the end of the recirculation zone $x = 390$ mm),

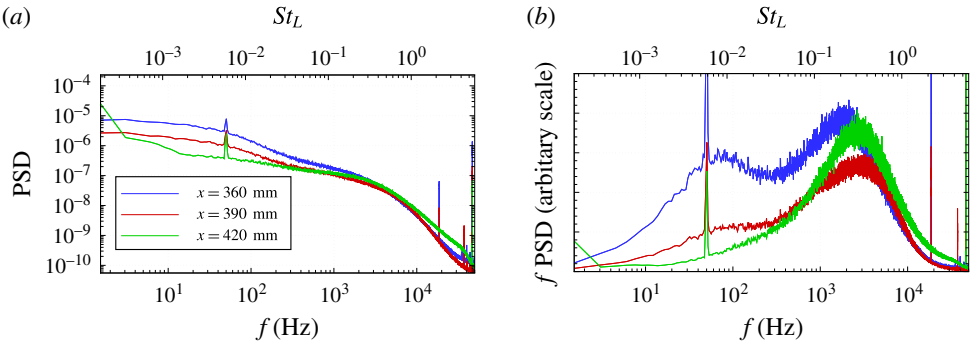

FIGURE 4. (Colour online) Skin-friction fluctuations on the centreline of the test section. (*a*) Power spectral density; (*b*) premultiplied spectrum.

then the skin-friction and pressure spectra are close: the medium-frequency peak is located at $f = 4$ kHz in the premultiplied pressure spectrum, while it is located at $f = 3$ kHz in the skin-friction spectrum.

Despite the small difference in the peak location, both measurement techniques confirm the presence of low-frequency motions, mostly located at the shock foot but also in the separated region, and medium-frequency motions, localised after the separation point and not limited to the recirculation zone. This observation compares favourably with all the SWBLI studies discussed in the literature. By scaling the frequency with appropriate length and velocity scales, we obtain satisfactory agreement with results obtained in other configurations, such as compression ramps (Dolling & Brusniak 1989; Wu & Martin 2008) or a shock impinging on a turbulent boundary layer (Dupont *et al.* 2006).

2.2. *High-speed Schlieren visualisation*

Pressure and skin-friction measurements, although very reliable, are only at few points and located at the wall. In order to have a global description of the unsteady behaviour of the interaction, we consider high-speed Schlieren visualisation. If Kulite and hot-film measurements are too local, Schlieren visualisation may suffer the opposite problem; the image obtained corresponds to a spanwise integration of the light beam, and may include three-dimensional effects due to the lateral boundary layers on the wind-tunnel walls.

Schlieren visualisation is a technique based on light deflection by a refractive index whose level is related to the flow density gradient. The deflected light beam is compared to the undeflected one by blocking the undisturbed light with a knife edge. A shadow pattern is then produced, representing the expansions and compressions in the flow. The magnitude of the density gradient is proportional to the light intensity measured by the camera sensor; a dark point on the image corresponds to negative density gradient whilst a bright point implies the presence of a positive one.

A high speed camera (Vision Research Phantom V710) with a 7 Gpx s^{-1} throughput and 300 ns digital exposure is placed on the side of the wind tunnel, and 60 000 images (464 $\times$ 360 pixels) are recorded at 35 kHz frame rate. The magnification ratio is around 3.3 px mm^{-1}, producing an image 140 mm wide which spans the whole channel height. Both horizontal and vertical knife-edge are considered: the light intensity is proportional, respectively, to the vertical and horizontal components of the density gradient (figure 5).

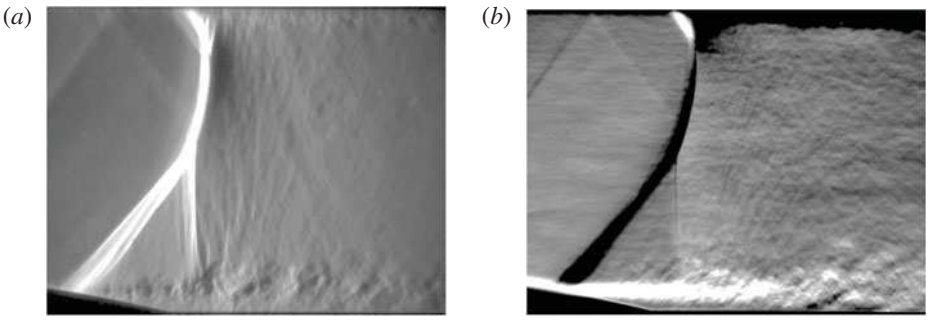

FIGURE 5. Horizontal and vertical density gradients obtained with the Schlieren apparatus. (*a*) $\partial\rho/\partial x$: vertically-oriented knife edge; (*b*) $\partial\rho/\partial y$: horizontally-oriented knife edge.

Figure 5(*a*) presents the horizontal density gradient; the shock wave has a positive gradient and is therefore white. The boundary layers are not visible, as they are not identified by any gradient in the streamwise direction. In the instantaneous Schlieren image, the mixing layer downstream the shock foot presents a succession of positive and negative density gradients, due to the vortices shed from the separation point. Here, small and medium scale structures are responsible for the high- and medium-frequency unsteadiness. Figure 5(*a*) also indicates that the mixing layer is a source of noise, generating acoustic waves under the form of almost vertical Mach lines which perturb the shock.

Figure 5(*b*) has been obtained with a horizontal edge-oriented knife. The boundary layers exhibit wall-normal density gradients due to the fact that the flow temperature is warmest near the walls and that the wall-normal pressure gradient is zero in these regions. Hence the picture is bright on the lower wall and dark on the upper one, corresponding to positive and negative $\partial\rho/\partial y$, respectively. The mixing layer on the lower-wall is bright since it is generated from the attached lower boundary layer, which was also bright. Across the shock wave, the density gradient is positive in the flow direction. The bump curvature yields a vertical velocity component which is negative, and thus the density gradient is negative.

Schlieren photography is now used to investigate the spatial structure of unsteadiness at low- and medium-frequencies. For this, we perform a Fourier-mode decomposition of the images and investigate the two-point correlations of the density gradient. The camera was equipped with a 12-bit colour depth sensor: the light intensity measured by each pixel is associated to a number between 0 and 4095. The available range is too small to describe at the same time the shock density gradient and the small variations in the mixing layer caused by the vortex shedding. For this reason, the images often exhibit colour saturation. Examples can be found in figure 5(*b*) on the shock (black region caused by the absence of light) or at the beginning of the mixing layer (white region associated to too much light intensity). This problem can cause signal truncation, adding high-frequency energy to the Fourier mode in the saturated zone, or showing 100 % correlation because of the absence of texture in the images.

2.2.1. *Fourier-mode decomposition*

In image processing, the time resolved image sequence can be written as $I(i, j, n)$ where I is the light intensity of each pixel. In this study, i and j vary from 1 to 464 and 1 to 360, n is the snapshot number (from 1 to $N = 60\,000$). The sampling

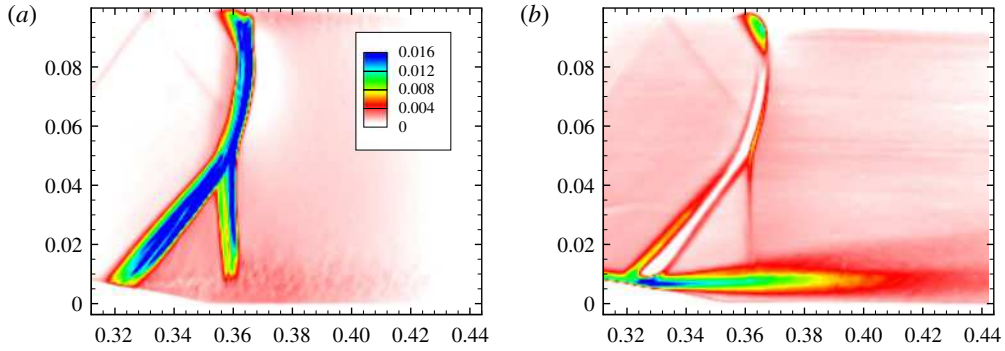

FIGURE 6. (Colour online) Fourier mode at $f = 300$ Hz for the horizontal and vertical density gradients. (*a*) Horizontal density gradient $\partial\rho/\partial x$; (*b*) vertical density gradient $\partial\rho/\partial y$.

frequency is 35 kHz. The time series describing the light intensity evolution at a given pixel (i, j) can be written as $I_{ij}(n)$. Assuming a linear correspondence between light intensity and density gradient, we compute the Fourier transform of $I_{ij}(n)$ using a FFT algorithm with a Hanning window function and 60 blocks with 50 % overlap of 2048 images.

Because of the reduced amount of data, the spectrum has a resolution of $f = 17$ Hz and the blocks are insufficient to converge the statistics of the lowest frequencies. The computed frequency spectrum is noisy and may not be compared to the frequency spectra presented in § 2.1, where we used 500 blocks. Yet, relying on the informations obtained in the previous section, we consider in the following the spatial structures of a low- and a medium-frequency Fourier mode, corresponding to the peaks displayed in the premultiplied pressure spectrum of figure 3(*b*).

Figure 6 shows the spatial structure of the low-frequency Fourier mode at $f = 300$ Hz. In figure 6(*a*) the fluctuations are located on the whole shock wave, without small scale structures after the separation point. Figure 6(*b*), which presents the vertical density gradient, shows that this Fourier mode has its maximum strength at the shock foot (also in the upper wall), even though the mode is located on the entire shock. The low-frequency mode is energetic also in the core of the mixing layer, where the PIV investigation of Sartor *et al.* (2012) has indicated that the turbulence production has its maximal value. The absence of energy inside the shock is a consequence of the lack of light in the Schlieren images and should not be interpreted as a stationary flow region.

In the upper left side of figure 6(*a*) and (*b*) two oblique lines reveal the presence of a compression wave, generated at the sonic throat and propagating across the flow at Mach angle $\alpha = \sin^{-1}(1/Ma)$. As it will be shown in the global stability analysis, those compression waves play an important role in the flow dynamics since they indicate the directions along which informations propagate in the supersonic zone.

Figure 7 displays the Fourier mode at $f = 4000$ Hz, located in the mixing layer region downstream of the separation point. Figure 7(*a*) also indicates the presence of small scale structures above the bump in the mixing layer (similar structures are also visible near the upper wall). In the shock region, the energy distribution is similar to the one in the low-frequency mode, but the energy levels are four times smaller than in the case of figure 6. Although similar features have been observed in the DNS simulations of Wu & Martin (2008), who documented the presence of small-amplitude

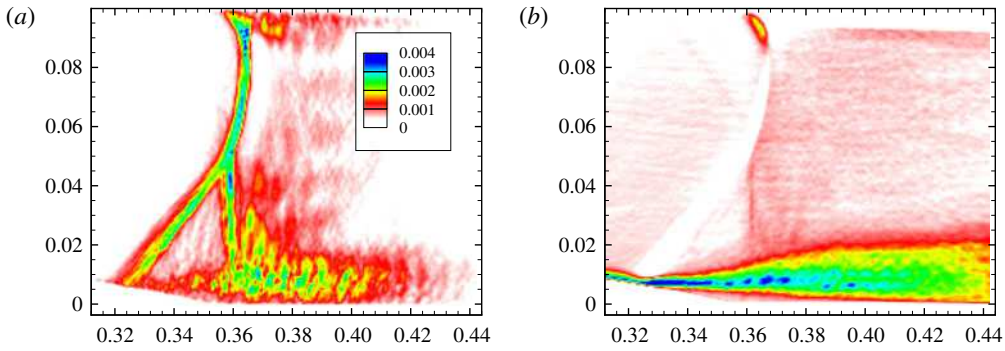

FIGURE 7. (Colour online) Fourier mode at $f = 4000$ Hz for the horizontal and vertical density gradients. (*a*) Horizontal density gradient $\partial\rho/\partial x$; (*b*) vertical density gradient $\partial\rho/\partial y$.

spanwise wrinkling on the shock, it is believed that in the present case the medium-frequency energy comes from the truncated signal due to colour saturation.

The medium-frequency mode in figure 7(*b*) suggests that the most energetic fluctuations are in the mixing layer, whilst the shock does not present any medium-frequency unsteadiness. This result confirms that medium-frequency motions on the shock are spurious, and only the mixing layer is affected by those motions.

Although less detailed in frequencies, the Fourier-mode decomposition confirms the presence of two characteristic modes. Medium-frequency perturbations are mainly located in the mixing layer. Using LES flow fields, Pirozzoli *et al.* (2010) performed a Fourier analysis and found similar results in a shock-impinging configuration. We also found that low-frequency perturbations are not only restricted to the shock foot, but affect the whole shock wave and even the top of the recirculation bubble. The mixing layer has therefore energetic contributions in both the low- and medium-frequency Fourier modes. A similar result has recently been observed in a compression ramp configuration (Grilli *et al.* 2012), where a dynamic mode decomposition (Schmid 2010) documented the presence of a low-frequency mode associated to the pulsation of the separation bubble and accompanied by a forward–backward shock motion.

2.2.2. *Two-point correlations*

In this section, a set of $N = 20\,000$ images is employed for analysing two-point correlations, which can give insights on the coherent structures of the flow, regardless of the frequency. As before, the light intensity of a given pixel at time n can be written as $I_{ij}(n)$. If we consider another pixel on the image, with coordinates (k, l), one can compute the correlation between the time series at point (k, l), indicated as $I_{kl}(n)$, and the time series at all other points $I_{ij}(n)$. When processing images where the brightness varies from image to image due to lighting, it is recommended to first subtract the mean and then normalise the results by dividing by the standard deviation of each data sequence. The cross-correlation coefficient is then given by:

$$C_{kl}(i,j) = \frac{1}{N}\sum_{n=1}^{N}\frac{[I_{ij}(n) - \overline{I_{ij}}][I_{kl}(n) - \overline{I_{kl}}]}{\sigma_{ij}\sigma_{kl}}, \tag{2.1}$$

where $\overline{I_{ij}}$ is the mean value of the light intensity and σ_{ij} and σ_{kl} are the standard deviations. The result of this operation is a set of 464×360 fields which represent,

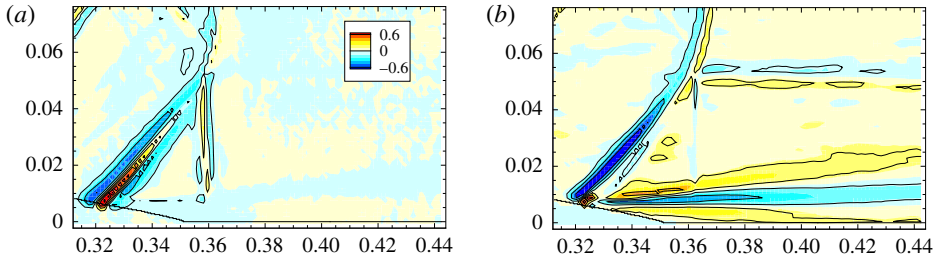

FIGURE 8. (Colour online) Correlations when the reference point (+ symbol) is at the shock foot. (*a*) Horizontal density gradient $\partial\rho/\partial x$; (*b*) vertical density gradient $\partial\rho/\partial y$.

for each interrogation point (k, l), the correlation between the chosen pixel and the whole image. The approach proposed in this section consists in fixing an interrogation point, for example at the shock foot or in the mixing layer, and investigating the zones of the flow where the density gradients are correlated to that point. Contrary to the correlation analyses based on wall-pressure measurements (Dolling & Erengil 1991; Dupont *et al.* 2006) or on numerical simulation data (Larchevêque *et al.* 2010; Touber & Sandham 2008), the correlations computed here are based on light intensity.

Figure 8 presents the correlation maps when the reference point is at the shock foot. A strong correlation exists with the whole shock wave, suggesting that shock movements are rigid-body displacements. The horizontally elongated correlated regions observed in the mixing layer of figure 8(*b*) reveal that the shock movements are linked to vertical displacements of the separated zone: due to the bump slope, shock movements correspond to vertical displacements of the separation point, which induce contractions and expansions of the recirculation bubble. This result has already been observed by Kussoy *et al.* (1988) in flow past a flared cylinder.

We have also found that the boundary layer fluctuations are not correlated to the shock or the mixing layer fluctuations, even if this observation is limited by the spatial resolution of the Schlieren pictures. On the contrary, when considering a point in the mixing layer, the spatial resolution of the Schlieren images is sufficiently fine to identify vortices generated near the separation point, as in figure 9. For example, when considering the horizontal density gradient, the correlation maps reveal the presence of large scale structures which can be linked to vortex shedding.

The sketch in figure 10(*a*) helps understanding of the horizontal density gradient distribution generated by three downstream travelling co-rotating vortical structures; on the lower part of the image, the density gradient is represented for two realisations. The correlation map highlights the region in the mixing layer with similar density gradient distributions, due to the passage of vortical structures. The result is a positive correlation on the reference point (red arrows) in the mixing layer, surrounded by two negatively correlated regions upstream and downstream of this point (blue arrows). A similar behaviour can be observed in figure 10(*b*) with the negatively correlated regions above and below the correlation point. The distance between the positive and negative correlation regions indicates the characteristic size of the shed vortices, which evolve spatially as moving downstream.

When considering the vertical density gradient correlations (figure 9*b*), the relation between the mixing layer movements and the shock displacements is even more evident; close to the separation, the shock foot and the mixing layer are highly correlated. In this region, the Fourier-mode decomposition showed high energy at low

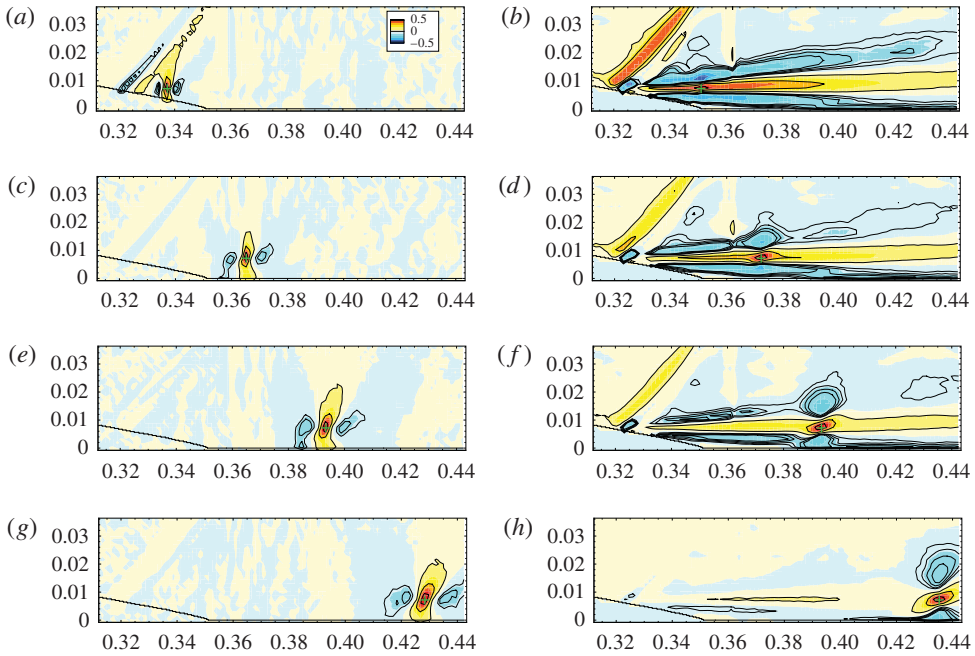

FIGURE 9. (Colour online) Correlations when the reference point (+ symbol) is in the mixing layer. (*a*) Horizontal density gradient $\partial\rho/\partial x$; (*b*) vertical density gradient $\partial\rho/\partial y$.

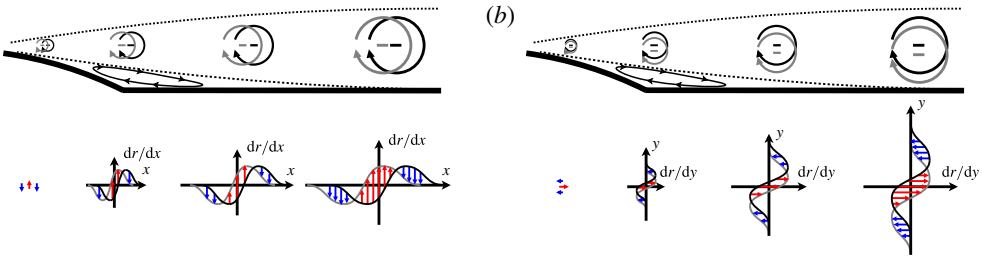

FIGURE 10. (Colour online) Density gradient distribution when vortical structures are shed in the mixing layer. (*a*) Horizontal density gradient $\partial\rho/\partial x$; (*b*) vertical density gradient $\partial\rho/\partial y$.

frequencies. Considering reference points more downstream in the mixing layer, the shock movements become less correlated, while vortical structures begin to appear. These structures are generated by Kelvin–Helmholtz type instabilities linked to the inflection point of the shear layer. Similar circular periodic patterns have also been observed in a shock reflection configuration by Agostini *et al.* (2012) and associated to medium-frequency unsteadiness using band-pass filtering.

3. Numerical approach

The experimental investigations have shown that the low- and medium-frequency perturbations exhibit characteristic frequencies and spatial wavenumbers below those of the small scale motions representative of turbulence. It seems therefore reasonable

that the scale-decoupling assumption holds within such a flow. Hence, the dynamics of the large scales might be captured by time-integration of RANS equations, while the impact of small scale dynamics on the large ones is accounted for by a turbulence model.

In this section, we consider a numerical model based on RANS equations closed with a Spalart–Allamaras turbulence model. First (§ 3.1) we will march in time these equations and observe that the flow converges to a steady-state solution. This indicates that unforced RANS equations are not able to capture the low- and medium-frequency perturbations. The asymptotic two-dimensional solution is then considered as a base flow for linear stability analyses. Both global modes of the Jacobian (§ 3.2) and singular modes of the Resolvent (§ 3.3) are computed.

3.1. *Base flow*

The simulations were performed using the finite volume solver elsA v3.3, developed at ONERA and CERFACS (Cambier, Heib & Plot 2013). Numerical computations were performed in parallel over up to 64 cores on ONERA's high-performance computer Stelvio, using 2.8 GHz Intel Xeon 5560 (Nehalem) processors. After spatial discretisation, the governing equations can be recast in the general conservative form:

$$\frac{\mathrm{d}\boldsymbol{w}}{\mathrm{d}t} = \mathscr{R}(\boldsymbol{w}), \tag{3.1}$$

where $\boldsymbol{w} \in \mathbb{R}^N$ represents the set of conservative variables describing the flow at each spatial location in the domain and $\mathscr{R}$ represents the discrete residual. Using a finite volume method, the dimension of $\boldsymbol{w}$ corresponds to the number of cells in the mesh times the number of variables. Note that all boundary conditions are included in the discrete operator $\mathscr{R}$.

The Spalart–Allmaras (S–A) turbulence model (Spalart & Allmaras 1992) has been chosen because previous studies (Deck 2005; Crouch, Garbaruk & Magidov 2007; Sartor *et al.* 2015) proved its ability to correctly reproduce the challenging buffet configuration. A second-order AUSM+(P) upwind scheme is employed for the convective fluxes in the mass, momentum and energy conservation equations (Mary, Sagaut & Deville 2000). Roe and Jameson schemes were not considered due to difficulties to converge to a steady-state solution. The convective flux associated to the turbulence equation is discretised with the first-order Roe scheme with Harten's correction (Harten & Hyman 1983), whilst a central-difference scheme is used for the turbulent diffusive flux.

The boundary conditions have been chosen to match the experimental configuration described in § 2; both upper and lower walls are considered as adiabatic walls and the boundary layers start developing in the settling chamber. The outlet pressure condition is adjusted to place the shock wave close to the position in the experimental configuration (approximately $p = 62$ kPa at $x = 0.65$ m). The computational domain, partly visible in figure 11, is a two-dimensional single-block representation of the S8Ch wind tunnel, composed of 120 000 nodes; 300 in the vertical direction, and 400 in the streamwise direction. In the shock region, the average distance between two mesh points is 0.45 mm. Considering the interaction length L as a characteristic dimension, this corresponds to a resolution of $\Delta_x/L = 0.013$. Eighty cells have been used to discretise the wall-normal gradients in the boundary layers, while the first point is located at $y^+ = 0.6$.

To assess the spatial convergence of the solutions, two other meshes are considered; a coarser mesh, with $\Delta_x/L = 0.020$ in the interaction region, and a finer one,

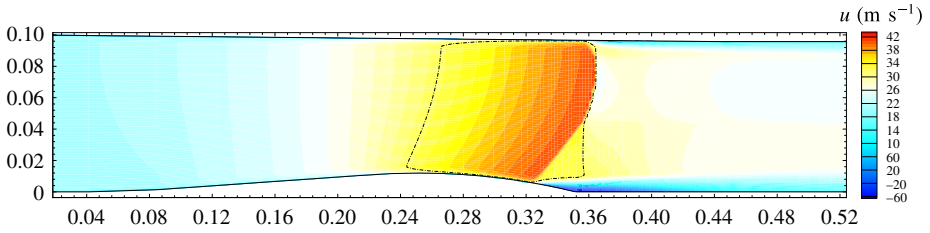

FIGURE 11. (Colour online) RANS simulation: steady-state solution of the wind-tunnel test section. Iso-contour of streamwise velocity and dashed-dotted sonic line.

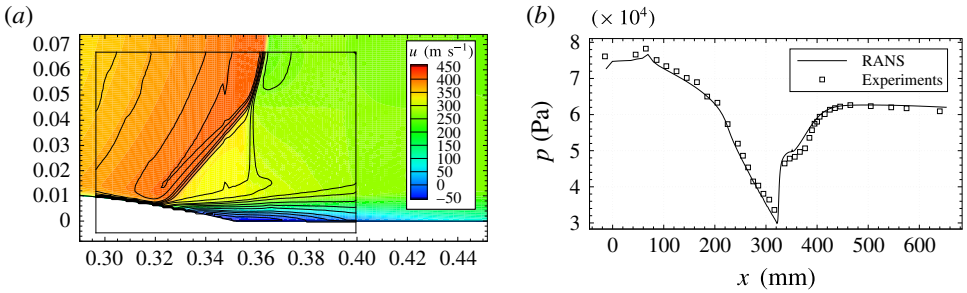

FIGURE 12. (Colour online) Comparison between the experimental results (pressure taps and PIV measurements from Sartor *et al.* (2012)) and the base flow (RANS solution). (*a*) Velocity field; (*b*) wall pressure.

with $\Delta_x/L = 0.065$. All grids converge to the same RANS solution in terms of shock location, size of the recirculation bubble and separation-point position, but the shock thickness increases with decreasing the cell size. As will be shown in the next sections, this does not impact the results of the global-mode decomposition, but slightly influences those of the singular-value.

3.1.1. *Results*

The resulting velocity field is displayed in figure 11, with a dashed-dotted sonic line. On the upper wall, the shock pressure gradient induces separation of the turbulent boundary layer, and a small separation bubble is formed.

Figure 12(*a*) shows a comparison between the experimental time-averaged PIV measurements obtained by Sartor *et al.* (2012) and those of the RANS simulation. The shock position compares favourably on the top, but in the numerical simulation the shock foot is slightly downstream. Moreover, the PIV results indicate a thicker shock, but this may come from the averaging of the shock unsteadiness in the experiments. The average pressure on the wall is depicted in figure 12(*b*); a rise of static pressure begins at $x = 320$ mm, corresponding to the shock foot. The recirculation bubble is characterised by a small pressure plateau, and after the separated zone the pressure reaches the value imposed at the downstream boundary.

Figure 13 presents three velocity profiles, taken upstream of the shock wave ($x =$ 300 mm), in the interaction region ($x = 340$ mm) and downstream of the separated zone ($x = 380$ mm). The PIV measurement and the RANS result are in fair agreement outside the separated region, with a slight velocity deficit in the numerical simulation (figure 13*a*,*c*). In figure 13(*b*), PIV measurements indicate similar velocities inside the

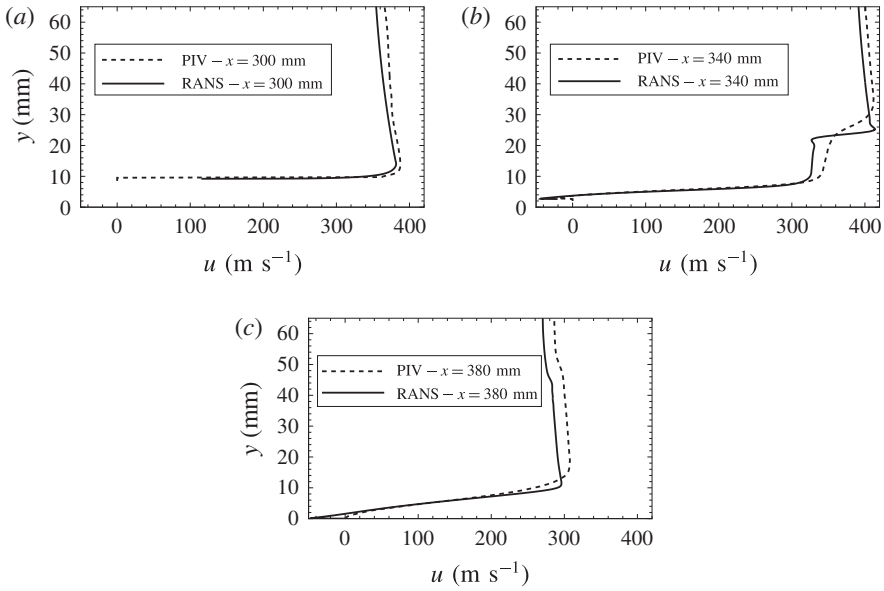

FIGURE 13. Velocity profiles from the numerical investigation and the PIV measurement. (*a*) Upstream of the shock; (*b*) in the interaction region; (*c*) downstream of the bubble.

recirculation zone and in the supersonic region, but a different distribution across the shear layer. This discrepancy can be attributed to the different lambda shape of the shock, probably due to three-dimensional effects in the wind tunnel.

Overall, RANS computations are in a fair agreement with the experimental investigation. Note that the characteristic length and velocity scales used in the following to obtain the Strouhal number are those of the experimental investigation.

Unsteady RANS simulations with a time step of $\Delta t = 10^{-6}$ s (corresponding to a maximum CFL number of 20) indicate a stationary solution. The velocity field obtained is the same as the steady-state result obtained with a local time stepping. This is not surprising since Knight & Degrez (1998) analysed the numerical capabilities of RANS approaches and stated that turbulent interaction predictions are correct only in terms of mean-pressure distribution: in this case, (unforced) RANS computations fail to predict the intermittent separation stage and to capture the high levels of unsteadiness.

As will be shown in the next section, inviscid phenomenon can have a strong signature on the results of the stability analysis. To separate the effect of the interaction with the boundary layers form the acoustic resonances, we considered a configuration with an equivalent geometry, but with slip conditions on both upper and lower walls. A new base flow is obtained, without any boundary layers and separated regions, with a normal shock impinging on the bump. The outlet pressure was adapted to locate the shock at approximately the same position as the configuration with boundary layers. The absence of viscous effects allows for the investigation of the role of the shock in the perturbation dynamics independently from those of the separated region.

The flow is governed by (3.1). The unsteady RANS computations indicate that a steady solution $\boldsymbol{w_0} \in \mathbb{R}^N$ exists, referred to as the base flow. This solution is defined by the equation:

$$\mathscr{R}(\boldsymbol{w_0}) = \boldsymbol{0}. \tag{3.2}$$

Since the governing system contains the Spalart–Allmaras equation, the base flow $\boldsymbol{w_0}$ takes into account the Reynolds stresses involved in the turbulence model. The vector $\boldsymbol{w_0}$ thus represents

$$\boldsymbol{w_0} = (\rho_0, \rho U_0, \rho V_0, \rho E_0, \rho \nu_0)^{\mathrm{T}}, \tag{3.3}$$

where $\rho\nu$ is introduced by the turbulence model. The subscript 0 indicates that all the variables refer to the steady-state solution of the RANS simulation. The stability of the flow is probed by analysing the evolution of small amplitude perturbations, superimposed on the base flow, which involve variations of the turbulent quantities.

3.2. *Global modes*

The equation governing small-amplitude perturbations is given by the first-order linearization of the discretised equations (3.1):

$$\frac{\mathrm{d}\boldsymbol{w}'}{\mathrm{d}t} = \boldsymbol{J}\boldsymbol{w}'. \tag{3.4}$$

The Jacobian operator $\boldsymbol{J} \in \mathbb{R}^{N\times N}$ corresponds to the linearization of the discrete Navier–Stokes operator $\mathscr{R}$ around the base flow $\boldsymbol{w_0}$. The proposed formalism does not assume homogeneity of the base flow in a given direction, and corresponds to the BiGlobal linear-stability analysis as introduced by Theofilis (2003). The analysis is two-dimensional, and we assume that the base flow and the fluctuations are homogeneous in the third direction.

The stability of a base flow is determined by scrutinising the spectrum of the matrix $\boldsymbol{J}$. To this end, particular solutions of (3.4) are sought in the form of normal modes $\boldsymbol{w}' = \hat{\boldsymbol{w}}\mathrm{e}^{\lambda t}$, where $\lambda = \sigma + \mathrm{i}\omega$ describes the temporal behaviour (σ is the amplification rate and ω the frequency) and $\hat{\boldsymbol{w}} \in \mathbb{C}^N$ the spatial structure. Since the governing equations involve a turbulence model, the perturbation includes variations of the turbulent quantities, and the turbulence model equation is also linearised. Hence (3.4) may be recast into the following eigenvalue problem:

$$\boldsymbol{J}\hat{\boldsymbol{w}} = \lambda\hat{\boldsymbol{w}}. \tag{3.5}$$

If at least one of the eigenvalues λ exhibits a positive growth rate σ, the base flow $\boldsymbol{w_0}$ is unstable. To compute the linearised operator, we follow a strategy based on a finite difference method, introduced by Mettot *et al.* (2014*a*), where the Jacobian coefficients are computed by repeated residual evaluations provided by the numerical code. More details on the numerical strategy can be found in Mettot *et al.* (2014*a*), Sartor *et al.* (2015) or Beneddine, Mettot & Sipp (2015), who successfully applied this method to open-cavity flow, transonic buffet and under-expanded screeching jets.

3.2.1. *Results*

To ease comparison with the experimental investigation, the results will be discussed using the dimensional frequency f (expressed in Hertz) and the Strouhal number St_L instead of the pulsation ω. The spectrum and the global modes, depicted in figures 14 and 15, are obtained by computing the five closest eigenvalues with respect to a given shift. Among the eigenvalues, which are all damped since they display a negative real part, one can recognise a group of modes in the lower part of the spectrum in the range of Strouhal numbers corresponding to the low-frequency unsteadiness.

Figure 15 shows the real part of some of those modes. The first (figure 15*a*) is located on the shock wave and represents a global movement of the shock structure.

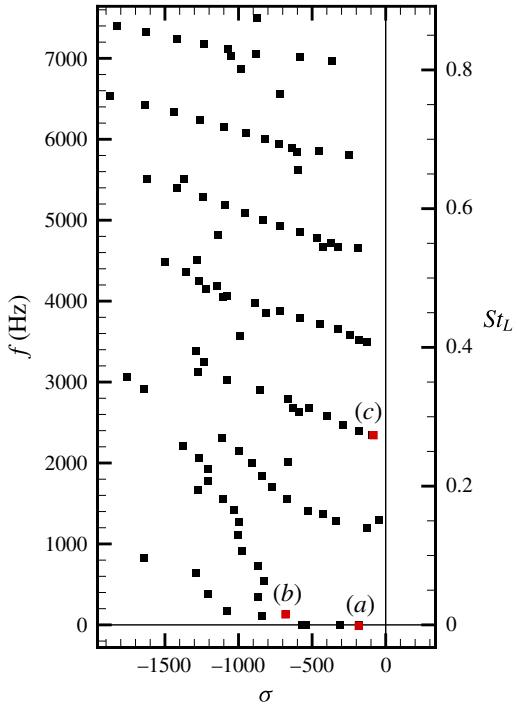

FIGURE 14. (Colour online) Spectrum.

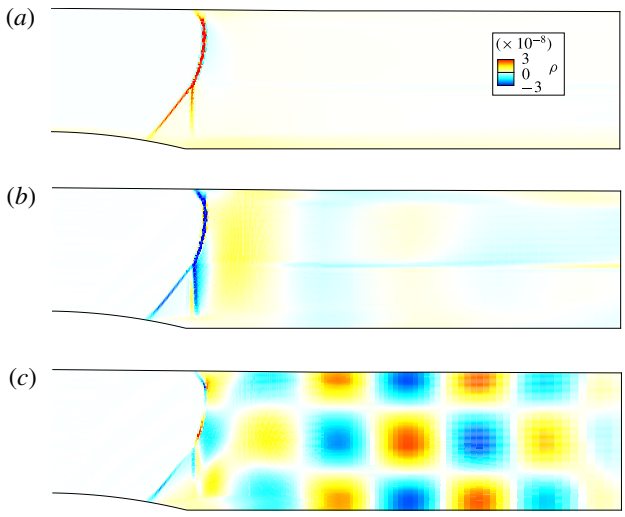

FIGURE 15. (Colour online) Stable global modes. (*a*) Real part of the stable mode at $f = 0$ Hz; (*b*) real part of the stable mode at $f = 130$ Hz; (*c*) real part of the stable mode at $f = 2340$ Hz.

Yet, since the mode is stationary, it does not carry any information about the unsteady behaviour of the interaction. Similarly, the second one (figure 15*b*) is also located on the shock, but with the addition of the slip line and a weak large scale streamwise oscillation in the subsonic region. Such a structure could correspond to an acoustic

wave that resonates with the test section, and which triggers solid-body movements of the shock wave.

Considering higher Strouhal numbers, one can recognise that the eigenvalues in figure 14 are grouped in periodic quasi-horizontal line, with some scattering when the damping rate becomes strong. The spatial structure of the least damped mode on one of those lines is presented in figure 15(*c*); the shock wave is still visible, but the horizontal and vertical wavy structures suggest that the mode is probably acoustic. Those structures propagate upstream preserving their shape while travelling towards the shock wave. All the stable modes just discussed are probably not linked to the unsteady dynamics of the SWBLI, but rather to some acoustic resonance of the channel flow.

In this configuration, as for a generic flow in a duct, if the acoustic wavelength has the same size as the device, the acoustic standing wave resonances may dominate the flow (Koch 2005). The spatiotemporal structure of the mode actually reveals that all the modes correspond to acoustic resonance modes linked to the channel height. All the modes belonging to the same periodic quasi-horizontal line are characterised by the same number of zeros in the vertical direction; one zero for the group characterised by $f \approx 1200$ Hz, two zeros for the group of eigenvalues such that $f \approx 2400$ Hz, etc. Regarding the size of the structures in the streamwise direction, we have verified that the streamwise wavelength L is related to the frequency f and the upstream travelling velocity of acoustic waves $|u - a|$ through $L = |u - a|/f$, where u is the local flow speed.

None of the analysed global modes in the medium-frequency range (more than 100 modes have been scrutinised) exhibit a spatial structure that can be linked to mixing layer instabilities, as would have been expected from the experimental investigation. We believe that such modes exist, but that they are even more damped. This suggests that in some cases the global mode decomposition is not the most convenient approach to explore medium-frequency perturbations in a transonic channel flow.

As previously introduced, a coarser and a finer mesh have been considered to assess grid convergence. Figure 16(*a*) shows the superposition of the spectra obtained with different meshes; nearly all the eigenvalues are converged, especially for low frequencies. Some discrepancies appear at higher frequencies, consistent with the fact that these modes are associated to small scale structures, and coarser meshes can cause spatial filtering. However, the frequencies associated to those structures are outside the range of interest of the study, so the reference grid can be considered adapted for the purpose of the investigation. Figure 16(*b*) presents the comparison between the eigenvalues of the reference case and those obtained when considering a base flow with slip conditions (see § 3.1). The absence of boundary layers and recirculation bubble barely influences the spectrum; the eigenvalues are still grouped into quasi-horizontal lines, confirming that these modes represent acoustic resonances and not the interaction dynamics. Low-frequency eigenvalues are slightly more damped, and no high-frequency modes appear or disappear from the reference spectrum.

3.3. *Singular modes*

If all the global modes are stable, the interaction behave as a noise amplifier. In this case, the transient energy growth is intrinsically linked to the non-normality of the Jacobian matrix (Trefethen *et al.* 1993; Schmid 2007) and an external driving term is now required to sustain the perturbations. This term stands for the environmental

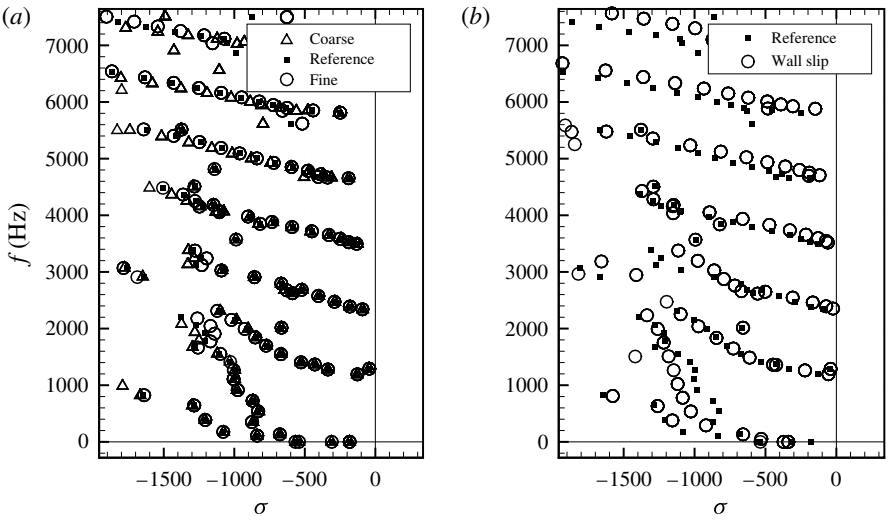

FIGURE 16. Eigenvalue decomposition of the Jacobian matrix. (*a*) Grid convergence; (*b*) effect of boundary layers.

disturbance, which is naturally present in any real flow. The stability analysis aims at quantifying the input/output dynamics by identifying the pseudo-resonances of the interaction. We therefore consider the response of the flow to a small-amplitude forcing $\boldsymbol{f}'$:

$$\frac{\mathrm{d}\boldsymbol{w}}{\mathrm{d}t} = \mathscr{R}(\boldsymbol{w}) + \boldsymbol{f}', \tag{3.6}$$

$\boldsymbol{w}$ is the superposition of the base flow $\boldsymbol{w_0}$ plus a small-amplitude response $\boldsymbol{w}'$ and is driven by the external forcing $\boldsymbol{f}'$. Considering a first-order Taylor expansion of the residual, the response $\boldsymbol{w}'$ is governed by the forced linearised Navier–Stokes equations. We consider a harmonic forcing $\boldsymbol{f}'(x, y, t)$ at frequency ω and a harmonic response $\boldsymbol{w}'(x, y, t)$ in the form $\boldsymbol{f}' = \hat{\boldsymbol{f}}(x, y)\mathrm{e}^{\mathrm{i}\omega t}$ and $\boldsymbol{w}' = \hat{\boldsymbol{w}}(x, y)\mathrm{e}^{\mathrm{i}\omega t}$, with $\hat{\boldsymbol{f}}, \hat{\boldsymbol{w}} \in \mathbb{C}^N$. Simplifying and re-arranging the equation for $\hat{\boldsymbol{w}}$ yields:

$$\hat{\boldsymbol{w}} = \boldsymbol{R}\hat{\boldsymbol{f}}, \tag{3.7}$$

where $\boldsymbol{R}(\omega)$ is the global resolvent matrix $\boldsymbol{R} = (\mathrm{i}\omega\boldsymbol{I} - \boldsymbol{J})^{-1}$ and $\boldsymbol{I}$ is the identity.

The resolvent matrix $\boldsymbol{R}(\omega)$ is defined for any real forcing frequency ω since all eigenvalues of $\boldsymbol{J}$ are strictly damped. The relation in (3.7) gives access, for a given frequency, to the harmonic response of the system when forced with a harmonic forcing of a given spatial form. We now introduce the gain G, function of the external forcing $\hat{\boldsymbol{f}}$ and defined for every frequency, as the ratio between the energy of the response and the energy of the forcing itself:

$$G(\hat{\boldsymbol{f}}) = \frac{\langle \hat{\boldsymbol{w}}, \hat{\boldsymbol{w}} \rangle_{\boldsymbol{Q}_e}}{\langle \hat{\boldsymbol{f}}, \hat{\boldsymbol{f}} \rangle_{\boldsymbol{Q}_f}}, \tag{3.8}$$

where $\langle \cdot, \cdot \rangle_{\boldsymbol{Q}_e}$ and $\langle \cdot, \cdot \rangle_{\boldsymbol{Q}_f}$ respectively refer to the scalar products that quantify the strength of the response and of the forcing. Here we chose the kinetic energy of the perturbation for the response $\hat{\boldsymbol{w}}$ and the energy of the momentum forcing for $\hat{\boldsymbol{f}}$.

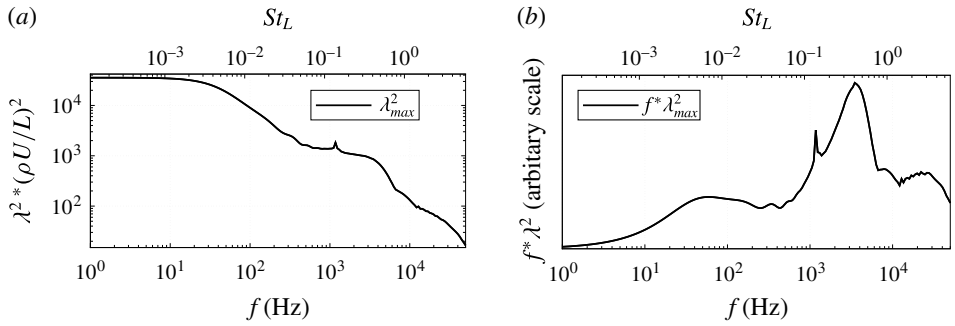

FIGURE 17. Most energetic singular value of the global resolvent. (*a*) Gain function, logarithmic scale; (*b*) normalised premultiplied optimal gain.

Among all the possible forcings, we are looking for the one that causes the strongest gain G, called the optimal forcing. Inserting (3.7) into (3.8) yields, for each frequency ω, an optimisation problem that can be solved through a singular-value decomposition of the global resolvent $\boldsymbol{R}(\omega)$, which may also be written as:

$$\boldsymbol{R}^{\dagger}\boldsymbol{R}\hat{\boldsymbol{f}} = \lambda^2 \hat{\boldsymbol{f}}. \tag{3.9}$$

where $\boldsymbol{R}^{\dagger}$ is the operator adjoint to $\boldsymbol{R}$. The real eigenvalue λ^2 is related to the forcing $\hat{\boldsymbol{f}}$, which we choose of unit norm $\langle \hat{\boldsymbol{f}}, \hat{\boldsymbol{f}} \rangle_{\mathcal{Q}_f} = 1$. The largest eigenvalue of this eigenproblem is λ^2_{max}, which corresponds to the optimal gain G. Once the corresponding optimal forcing is computed, the associated optimal response $\hat{\boldsymbol{w}}$ can be obtained solving (3.7) and verifies $\langle \hat{\boldsymbol{w}}, \hat{\boldsymbol{w}} \rangle_{\mathcal{Q}_e} = \lambda^2_{max}$. For more details and an application of this approach the reader is referred to Sipp & Marquet (2013) and Sartor *et al.* (2015).

3.3.1. *Results*

The singular values λ^2 have been non-dimensionalised with the reference length, velocity and density scales ($L = 35$ mm, $U = 300$ m s^{-1} and $\rho = 0.73$). Note that the value one does not define a threshold between damping and amplification; the role of the gain curve is to determine if there exist preferred frequencies in a flow excited by broadband white noise forcing. The optimal gain $\lambda^2(\rho U/L)^2$ has been represented as a function of frequency in figure 17. We observe that the strongest flow responses are obtained for low frequencies up to 50 Hz; then the gain decreases rapidly and reaches a plateau for frequencies within 1–4 kHz. This curve strongly resembles the experimental PSD curves obtained when processing pressure (figure 3*a*) and skin-friction measurements (figure 4*a*). For example, we both recover the strong flow response at low frequencies and the weaker plateau at medium frequencies.

The weighted gain $f\lambda^2$ has been represented in figure 17(*b*) as a function of frequency. This curve closely resembles the weighted PSD curves presented in figures 3(*b*) and 4(*b*). It displays a peak near $f = 50$ Hz, indicating the frequency where the energy content of the flow response is maximal. This peak occurs approximately at the same frequency as the one obtained with the hot-film sensors (figure 4*b*). Concerning the medium-frequency unsteadiness, the experimental measurements predicted a peak in pressure and skin-friction unsteadiness around $f = 2$–5 kHz (figures 3 and 4), in good agreement with the value of $f = 3$–4 kHz

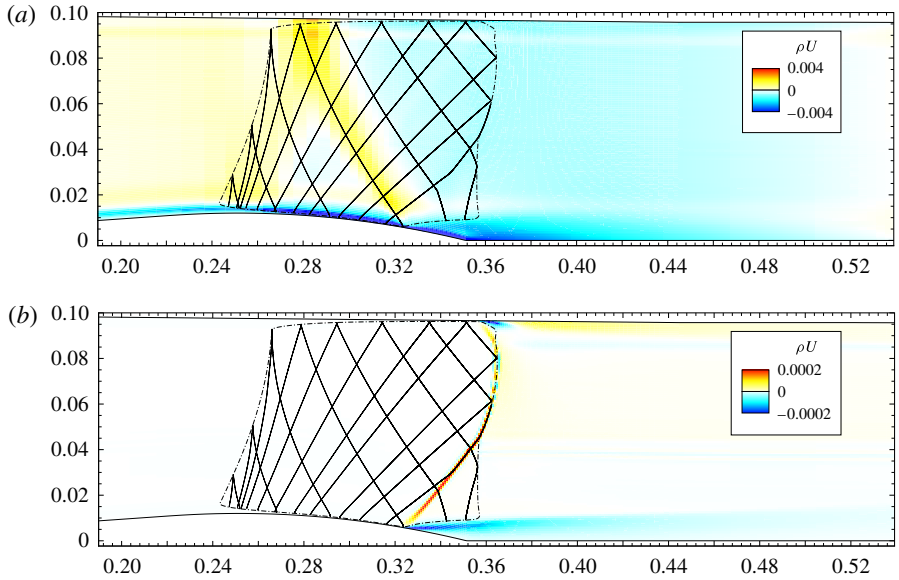

FIGURE 18. (Colour online) Real part of the optimal forcing and associated response at $f = 50$ Hz. Sonic line (dash-dotted) and characteristics (solid) superimposed. (*a*) Optimal forcing; (*b*) optimal response.

of figure 17(*b*). In spite of this, the reader should keep in mind that the results of the experimental investigation are issued from local measurements, while the gain function is a global quantity.

The optimal forcing obtained at the low frequency $f = 50$ Hz is shown in figure 18(*a*); it is located mostly in the boundary layer on the divergent part of the bump and is strongest at the shock foot. Starting from the top of the bump, the optimal forcing forms an oblique pattern that bounces on the upper sonic line and then hits the shock foot. To investigate the nature of this line we consider the theory of characteristics (Délery 2010). The oblique part of the forcing in figure 18(*a*) follows exactly the right characteristic line that impacts on the shock foot, where the recirculation bubble begins; the separation point therefore has a fundamental importance in the dynamics of the flow, and forcing at this position optimally influences the low-frequency dynamics. As the information propagates along the characteristic lines, the optimal forcing is energetic on the lines along which information propagates and impacts the separation point. More details can be found in Sartor *et al.* (2015), where a similar structure has been found in the case of a transonic flow over aerofoils, and has been observed in the adjoint unstable global mode associated to transonic buffet.

The optimal response associated to the low-frequency forcing is presented in figure 18*b*: the mode is located mostly on the shock wave, with a spatial form similar to what has been observed for the low-frequency Fourier mode of figure 6. Part of the response is located in the core of the mixing layer, with a horizontal structure of large wavelength. The presence of a negative value of the mode in the mixing layer, associated to a positive value on the shock, implies that the contraction of the bubble is related to a downstream motion of the reflected shock, whereas its expansion is related to intense reverse flow and, consequently, upstream motion of the

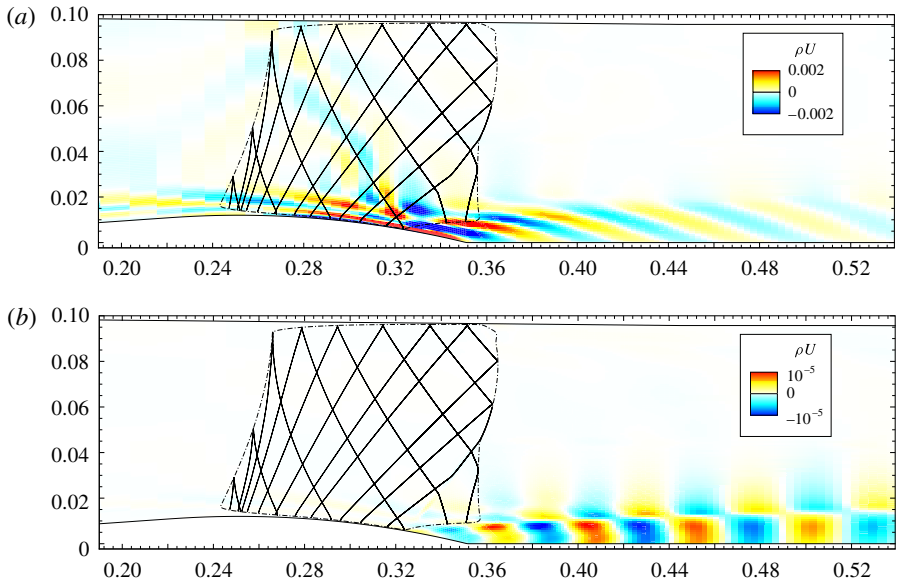

FIGURE 19. (Colour online) Real part of the optimal forcing and associated response at $f = 4000$ Hz. Sonic line (dash-dotted) and characteristics (solid) superimposed. (*a*) Optimal forcing; (*b*) optimal response.

reflected shock. This observation is consistent with the model proposed by Piponniau *et al.* (2009).

The medium-frequency optimal forcing at $f = 4$ kHz and its induced response are shown in figure 19. The spatial structure of the forcing is now more elaborated. It is still located both in the supersonic and subsonic regions, with strong values at the shock foot and at the beginning of the mixing layer. Yet, it is not anymore located along the characteristic lines. Similarly to the results of Marquet *et al.* (2008), we observe forcing structures which lay against the shear, confirming that the Orr (Orr 1907) mechanism is at play here. The medium-frequency forcing induces a response which is not localised on the shock-wave inside and along the mixing layer. Note that no acoustic wave pattern can be seen in the channel, indicating that this mode couples only weakly with acoustic waves. The present picture reminds the medium-frequency Fourier mode presented in figure 7. Finally, we observe medium scale wavelength structures due to Kelvin–Helmholtz type (Drazin & Reid 1980) instabilities, indicating that the medium-frequency unsteadiness is associated to vortex shedding.

To describe those motions, a Strouhal number based on the local mixing layer thickness $\delta_\omega(x)$, rather than on the interaction length L, is probably more significant. This quantity can be evaluated using the PIV measurement or the RANS result, and its value in a streamwise location corresponding to the centre of the separated zone ($x = 355$ mm) is $\delta_\omega = 6$ mm. The most appropriate velocity to compute the Strouhal number for Kelvin–Helmholtz instability is the mixing layer average speed, given by $\Delta U = (U_1 - U_2)/2 = 180$ m s^{-1}, where U_1 and U_2 are the flow velocities outside the mixing layer. This scaling would yield $S_\delta = 0.13$ for the medium-frequency unsteadiness, instead of $St_L = 0.5$ when using the interaction length and the reference velocity.

Grid convergence is assessed in figure 20(*a*). It is shown that medium- and high-frequency motions are well converged, while at low frequencies the gain is more

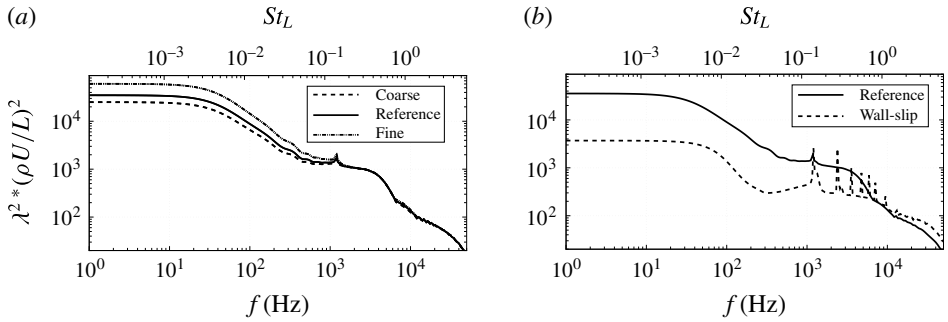

FIGURE 20. Optimal gain as a function of frequency. (*a*) Grid convergence; (*b*) effect of boundary layers.

energetic for a finer grid. This is not surprising since in this case the response of the flow is located on the shock, while we know that a finer grid has a strong impact on the representation of the shock wave (see § 3.1). We believe that even finer grids are required to converge the optimal gain curve at low frequencies. Yet, the main features presented here should remain unchanged.

Isolated peaks, located around $f = 1200$ Hz and its multiples, are visible in the gain function. To investigate their nature, we consider again the wall-slip configuration introduced in § 3.1. The new gain function (figure 20*b*) presents isolated peaks at the above mentioned frequencies. The associated responses are shown to be similar to the mode presented in figure 15(*c*). This indicates that these peaks are linked to acoustic resonance phenomena. Also, these peaks reflect the presence of weakly damped global modes in the spectrum shown in figure 16. Without boundary layers and recirculation region, it is seen that the evolution of the optimal gain still reveals a higher gain at low frequencies than at medium frequencies. Hence, even in this simplified case, the shock should react preferentially to low-frequency motions.

4. Conclusions

The main purpose of this study was twofold: to describe experimentally the unsteady dynamics of the transonic interaction between a strong shock and a turbulent boundary layer developing over the Délery bump; and to address the problem of unsteadiness in SWBLI employing stability analyses.

In the experimental investigation, wall-pressure and skin-friction fluctuations gave access to a local description of the unsteadiness. Near the shock foot, the low frequencies dominate the spectrum, while after the separation point medium-frequency fluctuations are most energetic. The recirculation zone displays both low- and medium-frequency unsteadiness. Similarly to other SWBLI, the fluctuations are broadband and weak in amplitude. The Strouhal numbers representative of low- and medium-frequency unsteadiness compare favourably with other configurations. An innovative investigation using high-speed Schlieren photography allowed for a more complete characterisation of the interaction: Fourier-mode decomposition indicated where low- and medium-frequency unsteadiness are most energetic. The results confirm the separation of temporal scales between the unsteadiness in the shock and the mixing layer. Cross-correlation maps showed that shock motions undergo rigid-body displacements accompanied by expansion and contraction of the recirculation bubble. In the mixing layer region, the medium-frequency perturbations are due to Kelvin–Helmholtz instabilities, which generate vortex shedding.

The interaction has been investigated numerically. It has been shown that unsteady RANS simulations converge toward a steady-state solution, which compares favourably with the mean PIV and wall-pressure measurements. Global stability analyses have then been conducted: the RANS equations were linearised around the base flow, and the Jacobian matrix explicitly extracted. The eigenvalue decomposition indicates that the flow is globally stable for two-dimensional perturbations, and the least stable eigenvalues cannot be related to the unsteadiness. Pseudo-resonances of the flow have then been identified by computing the singular values of the global resolvent. Such an input/output approach aims at characterising the receptivity of the flow to external forcings. It has been confirmed that low-frequency unsteadiness is due to a preferred response of the flow to existing environmental noise at low frequencies. The optimal forcings are concentrated both upstream and downstream of the shock, with a strong sensitivity at the shock foot. In the supersonic region, low-frequency forcings are also located along the right characteristic lines that impinge on the separation point. Medium-frequency unsteadiness is linked to Kelvin–Helmholtz instabilities, which exist regardless of the presence of the shock wave.

From a broader perspective, the considered two-dimensional interaction has potential for transient growth. If this behaviour were typical of all SWBLI, such flows would be better characterised by analysing the singular values and vectors of the global resolvent, and not the eigenvalues of the Jacobian matrix. Regarding the origin of the unsteadiness, it has been shown that both perturbations in the incoming flow and in the recirculation bubble may trigger shock unsteadiness. If this behaviour is conserved in three-dimensional cases, the source of low-frequency motions may not be unique. The authors support the idea that the interaction responds as a dynamical system which is affected by external or internal disturbances; if forced by an external agent, the flow will respond. However, even in the absence of this forcing, low-frequency oscillations can be caused by coupling between the dynamics of the separation bubble and the shock.

Acknowledgements

The authors would like to acknowledge the financial support of the French agency ANR through the DECOMOS program (compressible separated flows and self-sustained oscillations, ANR-10-BLANC-914). This work wouldn't have been possible without the constant guidance of Professor J.-P. Dussauge and P. Dupont, from the Supersonic Group of the IUSTI lab (Aix-Marseille Université). We are also grateful to Y. Le Sant, from ONERA – DAFE Department, for the wonderful tool that he developed for analysing and post processing the Schlieren images.

REFERENCES

ABDESSEMED, N., SHARMA, A. S., SHERWIN, S. J. & THEOFILIS, V. 2009 Transient growth analysis of the flow past a circular cylinder. *Phys. Fluids* **21**, 044103.

AGOSTINI, L., LARCHEVÊQUE, L., DUPONT, P., DEBIÈVE, J. F. & DUSSAUGE, J. P. 2012 Zones of influence and shock motion in a shock/boundary-layer interaction. *AIAA J.* **50** (6), 1377–1387.

ALIZARD, F., CHERUBINI, S. & ROBINET, J. C. 2009 Sensitivity and optimal forcing response in separated boundary layer flows. *Phys. Fluids* **21** (6), 064108.

ANDREOPOULOS, J. & MUCK, K. C. 1987 Some new aspects of the shock-wave/boundary-layer interaction in compression-ramp flows. *J. Fluid Mech.* **180** (1), 405–428.

BENEDDINE, S., METTOT, C. & SIPP, D. 2015 Global stability analysis of underexpanded screeching jets. *Eur. J. Mech. (*B*/Fluids)* **49**, 392–399.

BERESH, S. J., CLEMENS, N. T. & DOLLING, D. S. 2002 Relationship between upstream turbulent boundary-layer velocity fluctuations and separation shock unsteadiness. *AIAA J.* **40** (12), 2412–2422.

BLACKBURN, H. M., BARKLEY, D. & SHERWIN, S. J. 2008 Convective instability and transient growth in flow over a backward-facing step. *J. Fluid Mech.* **603**, 271–304.

BRANDT, L., SIPP, D., PRALITS, J. O. & MARQUET, O. 2011 Effect of base-flow variation in noise amplifiers: the flat-plate boundary layer. *J. Fluid Mech.* **687**, 503–528.

BUR, R., BENAY, R., GALLI, A. & BERTHOUZE, P. 2006 Experimental and numerical study of forced shock-wave oscillations in a transonic channel. *Aerosp. Sci. Technol.* **10** (4), 265–278.

BUR, R., COPONET, D. & CARPELS, Y. 2009 Separation control by vortex generator devices in a transonic channel flow. *Shock Waves* **19** (6), 521–530.

BUR, R., CORBEL, B. & DÉLERY, J. 1998 Study of passive control in a transonic shock wave/boundary-layer interaction. *AIAA J.* **36** (3), 394–400.

CAMBIER, LAURENT, HEIB, SÉBASTIEN & PLOT, SYLVIE 2013 The onera elsA CFD software: input from research and feedback from industry. *Mechanics Industry* **14** (03), 159–174.

CERQUEIRA, S. & SIPP, D. 2014 Eigenvalue sensitivity, singular values and discrete frequency selection mechanism in noise amplifiers: the case of flow induced by radial wall injection. *J. Fluid Mech.* **757**, 770–799.

CLEMENS, N. T. & NARAYANASWAMY, V. 2014 Low-frequency unsteadiness of shock wave/turbulent boundary layer interactions. *Annu. Rev. Fluid Mech.* **46**, 469–492.

COSSU, C. & CHOMAZ, J. M. 1997 Global measures of local convective instabilities. *Phys. Rev. Lett.* **78** (23), 4387.

CROUCH, J. D., GARBARUK, A. & MAGIDOV, D. 2007 Predicting the onset of flow unsteadiness based on global instability. *J. Comput. Phys.* **224** (2), 924–940.

CROUCH, J. D., GARBARUK, A., MAGIDOV, D. & TRAVIN, A. 2009 Origin of transonic buffet on aerofoils. *J. Fluid Mech.* **628** (1), 357–369.

DECK, S. 2005 Numerical simulation of transonic buffet over the OAT15A airfoil. *AIAA J.* **43** (7), 1556–1566.

DÉLERY, J. 1978 Analysis of the separation due to shock wave-turbulent boundary layer interaction in transonic flow. *La Recherche Aerospatiale* 305–320.

DÉLERY, JEAN 2010 *Handbook of Compressible Aerodynamics*. ISTE.

DOLLING, D. S. 2001 Fifty years of shock-wave/boundary-layer interaction research: what next? *AIAA J.* **39** (8), 1517–1531.

DOLLING, D. S. & BRUSNIAK, L. 1989 Separation shock motion in fin, cylinder, and compression ramp-induced turbulent interactions. *AIAA J.* **27** (6), 734–742.

DOLLING, D. S. & ERENGIL, M. E. 1991 Unsteady wave structure near separation in a Mach 5 compression ramp interaction. *AIAA J.* **29** (5), 728–735.

DRAZIN, P. G. & REID, W. H. 1980 *Solutions to the Problems in Hydrodynamic Stability*. Cambridge University Press.

DUPONT, P., HADDAD, C. & DEBIÈVE, J. F. 2006 Space and time organization in a shock-induced separated boundary layer. *J. Fluid Mech.* **559**, 255–278.

DUSSAUGE, J. P., DUPONT, P. & DEBIÈVE, J. F. 2006 Unsteadiness in shock wave boundary layer interactions with separation. *Aerosp. Sci. Technol.* **10** (2), 85–91.

EHRENSTEIN, U. & GALLAIRE, F. 2005 On two-dimensional temporal modes in spatially evolving open flows: the flat-plate boundary layer. *J. Fluid Mech.* **536**, 209–218.

ERENGIL, M. E. & DOLLING, D. S. 1991*a* Correlation of separation shock motion with pressure fluctuations in the incoming boundary layer. *AIAA J.* **29** (11), 1868–1877.

ERENGIL, M. E. & DOLLING, D. S. 1991*b* Unsteady wave structure near separation in a Mach 5 compression ramp interaction. *AIAA J.* **29** (5), 728–735.

FARRELL, B. F & IOANNOU, P. J. 1996 Generalized stability theory. Part I: Autonomous operators. *J. Atmos. Sci.* **53** (14), 2025–2040.

GRILLI, M., SCHMID, P. J., HICKEL, S. & ADAMS, N. A. 2012 Analysis of unsteady behaviour in shockwave turbulent boundary layer interaction. *J. Fluid Mech.* **700**, 16–28.

HARTEN, A. & HYMAN, J. M. 1983 Self adjusting grid methods for one-dimensional hyperbolic conservation laws. *J. Comput. Phys.* **50** (2), 235–269.

HUERRE, P. 2000 Open shear flow instabilities. In *Perspectives in Fluid Dynamics* (ed. G. Batchelor, H. Moffatt & M. Worster), Perspectives in Fluid Dynamics, pp. 159–229. Cambrige University Press.

IACCARINO, G., OOI, A., DURBIN, P. A. & BEHNIA, M. 2003 Reynolds averaged simulation of unsteady separated flow. *Intl J. Heat Fluid Flow* **24** (2), 147–156.

JACKSON, C. P. 1987 A finite-element study of the onset of vortex shedding in flow past variously shaped bodies. *J. Fluid Mech.* **182** (1), 23–45.

JOVANOVIC, M. R. & BAMIEH, B. 2005 Componentwise energy amplification in channel flows. *J. Fluid Mech.* **534**, 145–184.

KNIGHT, D. D. & DEGREZ, G. 1998 Shock wave boundary layer interactions in high Mach number flows a critical survey of current numerical prediction capabilities. *AGARD ADVISORY REPORT AGARD AR* **2**, 1–1.

KOCH, W. 2005 Acoustic resonances in rectangular open cavities. *AIAA J.* **43** (11), 2342–2349.

KUSSOY, M. I., BROWN, J. D., BROWN, J. L., LOCKMAN, W. K. & HORSTMAN, C. C. 1988 Fluctuations and massive separation in three-dimensional shock-wave/boundary-layer interactions. In *Transport Phenomena in Turbulent Flows: Theory, Experiment, and Numerical Simulation* (ed. M. Hirata & N. Kasagi), pp. 875–887. Hemisphere.

LARCHEVÊQUE, L., DUPONT, P., DE MARTEL, E., GARNIER, E. & DEBIÈVE, J. F. 2010 Experimental and numerical study of unsteadiness in boundary layer/shock wave interaction. In *Turbulence and Interactions*, pp. 263–269. Springer.

LAWSON, S. J. & BARAKOS, G. 2011 Review of numerical simulations for high-speed, turbulent cavity flows. *Prog. Aerosp. Sci.* **47** (3), 186–216.

MARQUET, O., SIPP, D., CHOMAZ, J. M. & JACQUIN, L. 2008 Amplifier and resonator dynamics of a low-reynolds-number recirculation bubble in a global framework. *J. Fluid Mech.* **605**, 429.

MARY, I., SAGAUT, P. & DEVILLE, M. 2000 An algorithm for unsteady viscous flows at all speeds. *Intl J. Numer. Meth. Fluids* **34** (5), 371–401.

MCKEON, B. J. & SHARMA, A. S. 2010 A critical-layer framework for turbulent pipe flow. *J. Fluid Mech.* **658** (1), 336–382.

METTOT, C., RENAC, F. & SIPP, D. 2014*a* Computation of eigenvalue sensitivity to base flow modifications in a discrete framework: Application to open-loop control. *J. Comput. Phys.* **269**, 234–258.

METTOT, C., SIPP, D. & BÉZARD, H. 2014*b* Quasi-laminar stability and sensitivity analyses for turbulent flows: Prediction of low-frequency unsteadiness and passive control. *Phys. Fluids* **26** (4), 045112.

ORR, W. M. F. 1907 The stability or instability of the steady motions of a perfect liquid and of a viscous liquid. Part II: A viscous liquid. In *Proceedings of the Royal Irish Academy. Section A: Mathematical and Physical Sciences*, pp. 69–138. Hodges, Figgis, & Co.

PIPONNIAU, S., DUSSAUGE, J. P., DEBIÈVE, J. F. & DUPONT, P. 2009 A simple model for low-frequency unsteadiness in shock-induced separation. *J. Fluid Mech.* **629**, 87–108.

PIROZZOLI, S., LARSSON, J., NICHOLS, J. W., BERNARDINI, M., MORGAN, B. E. & LELE, S. K. 2010 Analysis of unsteady effects in shock/boundary layer interactions. *Annu. Res. Briefs* 153–164.

PLOTKIN, K. J. 1975 Shock wave oscillation driven by turbulent boundary-layer fluctuations. *AIAA J.* **13** (8), 1036–1040.

ROBINET, J. C. 2007 Bifurcations in shock-wave/laminar-boundary-layer interaction: global instability approach. *J. Fluid Mech.* **579** (1), 85–112.

RODI, W. 1997 Comparison of LES and RANS calculations of the flow around bluff bodies. *J. Wind Engng Ind. Aerodyn.* **69**, 55–75.

SARTOR, F., LOSFELD, G. & BUR, R. 2012 PIV study on a shock induced separation in a transonic flow. *Exp. Fluids* **53** (3), 815–827.

SARTOR, F., METTOT, C. & SIPP, D. 2015 Stability, receptivity and sensitivity analyses of buffeting transonic flow over a profile. *AIAA J.* **53** (7), 1980–1993.

SCHMID, P. J. 2007 Nonmodal stability theory. *Annu. Rev. Fluid Mech.* **39**, 129–162.

SCHMID, P. J. 2010 Dynamic mode decomposition of numerical and experimental data. *J. Fluid Mech.* **656**, 5–28.

SCHMID, P. J. & HENNINGSON, D. S. 2001 *Stability and Transition in Shear Flows*. Springer.

SIPP, D. & MARQUET, O. 2013 Characterization of noise amplifiers with global singular modes: the case of the leading-edge flat-plate boundary layer. *Theor. Comput. Fluid Dyn.* **27** (5), 617–635.

SIPP, D., MARQUET, O., MELIGA, P. & BARBAGALLO, A. 2010 Dynamics and control of global instabilities in open-flows: a linearized approach. *Appl. Mech. Rev.* **63** (3), 30801.

SPALART, P. R. & ALLMARAS, S. R. 1992 A one equation turbulence model for aerodinamic flows. *AIAA paper* 1992–0439.

THEOFILIS, V. 2003 Advances in global linear instability analysis of nonparallel and three-dimensional flows. *Prog. Aerosp. Sci.* **39** (4), 249–315.

THEOFILIS, V. 2011 Global linear instability. *Annu. Rev. Fluid Mech.* **43**, 319–352.

TOUBER, E. & SANDHAM, N. D. 2008 Oblique shock impinging on a turbulent boundary layer: low-frequency mechanisms. *AIAA paper* 2008–4170.

TOUBER, E. & SANDHAM, N. D. 2009 Large-eddy simulation of low-frequency unsteadiness in a turbulent shock-induced separation bubble. *Theor. Comput. Fluid Dyn.* **23** (2), 79–107.

TOUBER, E. & SANDHAM, N. D. 2011 Low-order stochastic modelling of low-frequency motions in shock-wave/boundary-layer interactions. *J. Fluid Mech.* **671**, 417–465.

TREFETHEN, L., TREFETHEN, A., REDDY, S. & DRISCOLL, T. 1993 Hydrodynamic stability without eigenvalues. *Science* **261** (5121), 578–584.

WU, M. & MARTIN, M. P. 2008 Analysis of shock motion in shockwave and turbulent boundary layer interaction using direct numerical simulation data. *J. Fluid Mech.* **594**, 71.

Dynamique et contrôle de l'interaction onde de choc / couche limite

Le phénomène d'interaction onde de choc / couche limite apparaît dès lors que l'écoulement atteint le régime supersonique, ce qui est fréquemment le cas pour les applications aéronautique (avions de transport et de combat, missiles) et spatial (lanceurs, corps de rentrée). Ce phénomène est étudié dans un canal transsonique dans lequel l'interaction forte entre le choc droit (en lambda) et la couche limite turbulente provoque un décollement massif de l'écoulement. La position de l'onde de choc est soit quasi-stationnaire dans le canal, soit forcée par une came elliptique en rotation placée en aval de l'interaction.
Des mesures optiques non intrusives ont permis de déterminer la nature tridimensionnelle du décollement ainsi que la réponse de l'interaction au forçage quasi-harmonique, en quantifiant l'évolution de la zone décollée et de la couche de cisaillement durant un cycle d'oscillation du choc. Ces écoulements sont alors contrôlés par des actionneurs passif, de type générateurs de tourbillon, et actif par aspiration localisée au niveau de la zone décollée. Les générateurs de tourbillon placés en amont de l'interaction sont efficaces pour réduire le décollement, grâce à une meilleure distribution de la quantité de mouvement dans la couche limite. Pour le cas de l'oscillation forcée, le contrôle par aspiration permet de réduire plus efficacement l'amplitude des oscillations du choc, avec des débits d'aspiration modérés. La dynamique de l'interaction est étudiée à la fois à partir de visualisations strioscopiques obtenues par une caméra à haute cadence, et par un calcul de stabilité globale puis par une analyse de la réceptivité de l'écoulement à un forçage externe.
Le calcul montre que tous les modes sont stables et, donc, que l'écoulement est un amplificateur sélectif de bruit. L'interaction est définie par la coexistence de deux fréquences caractéristiques distinctes, le battement du choc à basse fréquence et la dynamique de la couche de cisaillement à plus haute fréquence, liée aux instabilités de Kelvin-Helmholtz.

Mots-clés : ONDE DE CHOC ; OSCILLATION CHOC ; COUCHE LIMITE DECOLLEE ; INTERACTION CHOC COUCHE LIMITE ; ECOULEMENT TURBULENT ; CONTROLE ECOULEMENT

Dynamics and control of shock wave / boundary layer interaction

Shock wave / boundary layer interaction appeared in supersonic flow regime, which is mainly the case in both aeronautical (transport and military aircrafts, missiles) and aerospace (launchers, re-entry vehicles) applications. This phenomenon has been studied in a transonic channel where the strong interaction between the lambda normal shock and the turbulent boundary layer leads to a massive flow separation. The shock wave position into the channel could be quasi-steady or forced by a rotating elliptical shaft located far downstream of the interaction. Non-intrusive optical measurements allowed to determine the tri-dimensional behaviour of the separation and the response of the interaction to the quasi-harmonic forcing, by quantifying the separated zone and the shear layer evolutions during a shock oscillation cycle. Then, flow control on both natural and forced configurations is carried out by means of passive - vane-type vortex generators- and active - suction flow in the separated region - devices. Vortex generators located upstream of the interaction are efficient to reduce the separation thanks to a better mixed momentum distribution into the incoming boundary layer. For the forced configuration, active control allowed to diminish the shock oscillation amplitude, even with moderate suction mass flow rates. Dynamics of the interaction is studied by a Fourier analysis of Schlieren visualisations provided by a high speed camera, but also by a global stability calculation and a receptivity analysis of the flow to external optimal forcing.
The eigenvalue decomposition indicates that all the modes are stable and, then, that the flow behaves as a noise amplifier. The interaction region is characterised by the existence of two selected frequencies, one at low frequency for the shock displacement and the other at medium higher frequency corresponding to the dynamics of the shear layer due to Kelvin-Helmholtz instabilities.

Keywords : SHOCK WAVE ; SHOCK OSCILLATION ; BOUNDARY LAYER SEPARATION ; SHOCK BOUNDARY LAYER INTERACTION ; TURBULENT FLOW ; FLOW CONTROL.

Office National d'Études et de Recherches Aérospatiales
BP 72 - 29 avenue de la Division Leclerc
92322 CHATILLON CEDEX
Tél. : +33 1 46 73 40 40 - Fax : +33 1 46 73 41 41
http://www.onera.fr